State-of-the-Science Review of the Stress Field during a Glacial Cycle and Glacially Induced Faulting

NWMO-TR-2021-09 June 2021

Patrick Wu

University of Calgary

NUCLEAR WASTE MANAGEMENT ORGANIZATION
SOCIÉTÉ DE GESTION DES DÉCHETS NUCLÉAIRES

Nuclear Waste Management Organization
22 St. Clair Avenue East, 4th Floor
Toronto, Ontario
M4T 2S3
Canada

Tel: 416-934-9814
Web: www.nwmo.ca

State-of-the-Science Review of the Stress Field during a Glacial Cycle and Glacially Induced Faulting

NWMO-TR-2021-09

June 2021

Patrick Wu
University of Calgary

Document History

Title:	State-of-the-Science Review of the Stress Field during a Glacial Cycle and Glacially Induced Faulting		
Report Number:	NWMO-TR-2021-09		
Revision:	R000	Date:	June 2021
Author Company(s)			
Authored by:	Patrick Wu		
Nuclear Waste Management Organization			
Reviewed by:	Richard Crowe, Monique Hobbs, Sarah Hirschorn		
Reviewed by:	Raymond Munier (Terra Mobile Consultants, AB)		
Accepted by:	Paul Gierszewski		

Revision Summary		
Revision Number	**Date**	**Description of Changes/Improvements**
R000	2021-June	Initial issue

Title: **State-of-the-Science Review of the Stress Field during a Glacial Cycle and Glacially Induced Faulting**
Report No.: **NWMO TR-2021-09**
Author(s): Patrick Wu
Company: University of Calgary
Date: June 2021

Abstract

Glacial cycles are known to exert an influence on the regional state of stress and in turn this may influence the stability of faults and increase the frequency of earthquakes. This report reviews the scientific background related to the response of the Earth to glacial cycles, summarizing current knowledge and understanding of the influence of glacial cycles on the evolution of fault stability.

To model the spatio-temporal variation of stress and fault stability, the stresses induced from glacial loading, including those from bending of the lithosphere and relaxation of the mantle are superposed on the overburden stress, pore fluid pressure and ambient tectonic stresses to give the total stress. The effect of stress changes associated with sedimentation and erosion processes and shear induced by glacier flow are also considered and are found to be relatively unimportant. Various rock failure criteria including the changes in fault stability margin from Mohr-Coulomb failure criteria are reviewed and the assumption of virtual faults and optimal orientation are also discussed. Stresses induced by glacial loads are not large enough to fracture intact rocks in the crust, but can reactivate pre-existing faults that are initially close to failure. Since the ambient tectonic stresses are required to keep pre-existing faults close to failure, both glacially induced stresses and ambient tectonic stresses are important in fault stability studies.

The spatio-temporal variation of the fault stability margin (δFSM) in once glaciated areas of Eastern Canada (Laurentia or Laurentide), Fennoscandia, and Scotland are studied. For loads of large horizontal extent (e.g. Laurentide ice sheet), fault instability is suppressed by the weight of the load. However, this is not true for small isolated ice caps since the effect of stress amplification becomes significant. The effects of tectonic stress and overburden, material properties, compressibility, mantle rheology and lithospheric ductile zones are also studied. It is found that a thrust background stress regime is able to explain many of the observed data in Laurentia and Fennoscandia. The size of the ice sheet and its deglaciation history are found to have large effects on the onset timing of earthquakes inside and outside the ice margin. Mantle rheology has large effects on the onset time of earthquakes and the amplitude of fault stability margin outside the ice margin, but has little effect on the onset timing and mode of failure within the ice margin. However, mantle viscosity is observed to have a large effect on the rate of change in δFSM within the ice margin after glacial retreat. A vertical ductile zone within the lithosphere is found to concentrate the strain rate and δFSM near the ductile zone inside the ice margin.

Results from modeling slip on a single fault plane in 2D confirm that faults can become stabilized when loaded by an ice sheet of sufficient thickness and can be reactivated near the end of deglaciation. When reactivated, thrust faults with low dip angle typically slip once and stop, but high angle thrust faults can slip more than once, with subsequent slips smaller than the first event. The amount of fault slip can be predicted from the model which dictates the magnitude of the induced earthquake and the stress release which determines the subsequent seismic history of the fault.

TABLE OF CONTENTS

LIST OF FIGURES

Page

1. INTRODUCTION

Intraplate earthquakes are observed in the once glaciated areas of Eastern Canada (Laurentia/Laurentide), Northern Europe (Fennoscandia) and around the current ice margins of the Greenland and Antarctica ice sheets. In order to understand the spatio-temporal variation of the state of stress and the potential for fault motion in particular, the role of glacial loading and unloading in the triggering of earthquakes needs to be considered.

The main aim of this report is to review the scientific background, the conceptual model and computational results related to the spatio-temporal evolution of stress and fault stability in glaciated areas. Although some geophysical and geological observations are also mentioned, their review is outside of the scope of this report.

In Section 1, terminology such as ice sheets, ice ages and glacial isostatic adjustment will be described, as well as some of the geological observations about intraplate earthquakes, the state of stress and the importance of visco-elasticity in understanding glacial isostatic adjustment of the Earth to glacial cycles. Section 2 reviews the computational methods for the stresses induced by glacial cycle. Section 3 reviews spatial-temporal variation of total stress and summarizes how the contribution from pore fluid, overburden and tectonic stresses are included in the model. The shear stress induced by the motion of ice sheets is also considered. Section 4 reviews the failure of rocks and faulting mechanisms, including a discussion of the change in fault stability, which will be central to the discussion of this report. Section 5 reviews some recent work and recent progress in understanding the factors that affect fault stability. Section 6 reviews recent work that attempts to treat faults more realistically, followed by a discussion and summary of the key findings in this report.

1.1 GLACIERS, ICE AGES AND GLACIAL ISOSTATIC ADJUSTMENT

1.1.1 Glaciers, Ice Sheets, Ice Stream & Ice Shelf

A *glacier* is a large, slow-moving mass of perennial ice formed by the compaction of layers of snow. There are two types of glaciers: *alpine glaciers* that are found in mountainous areas and *continental glaciers* that contain an enormous mass of ice continuously covering large areas of the continent. Smaller glaciers that cover less than 50,000 km^2 are called *ice caps* while the larger ones are called *ice sheets*. Today, ice sheets are found only in Antarctica and Greenland.

The shape of the Antarctic ice sheet is approximately parabolic (refer to section 3.4, Eqn 3.13), so that the maximum ice thickness is determined by its horizontal dimension and the mean yield stress at the base of the glacier. The parabolic profile is predicted by ice mechanics and is taken to be the ideal ice shape. During the last Ice Age, the Laurentide ice sheet covered most parts of Canada and northern USA, the Fennoscandian (or Weichselian) ice sheet covered Northern Europe and the Patagonian ice sheet covered the southern part of South America.

Where the ice sheet meets the ocean, there is a thick tongue of floating ice called the *ice shelf*. An ice sheet may contain *ice streams* – long narrow regions that move significantly faster than the surrounding ice. Ice streams usually occur where the ice starts to leave the ice sheet and enter into the ice shelf. In Antarctica, ice streams account for about 10% of the volume of ice. The speed of flow in the ice streams of Greenland is approximately 100 m/year, but fast flowing outlet glaciers have an ice flow rate as high as 1500 m/year (Joughin et al. 2008). *Ice quakes* can occur within an ice sheet, possibly due to calving of ice (Tsai et al. 2008, Tsai & Ekström 2007) and should not be confused with earthquakes, as discussed in this report.

1.1.2 Ice Ages

The normal temperature of the Earth throughout its history has been much warmer than today and normally the Earth seems to have been ice-free even in high latitudes. However, there is evidence of 4 to 5 extensive Ice Ages in the past: The earliest one is the Huronian ice age (2.7-2.3 billion years ago) but this is less well-documented than the others. The second one occurred during the Neoproterozoic (850 – 630 million years ago) and may have produced a *Snowball Earth* (i.e. the whole Earth appears to have been encased in ice – even at the equator). This is followed by a minor ice age during the Late Ordovician and the Silurian periods (460-430 million years ago) and a more extensive ice age during the Permo-Carboniferous period (350 – 260 million years ago). The latest and the best documented is the Pleistocene ice age (2.6 million years ago) although the climate in the Northern Hemisphere started a gradual, but not strictly uniform, decline, even in the Eocene. The Antarctic ice sheet started to grow almost 20 million years ago.

Within each ice age are cycles of glaciation with ice sheets advancing and retreating. The colder periods are called *glacial periods* and the warmer periods *inter-glacials*. Within a glacial period there are warmer periods of short durations called *interstadials*, and within the warmer inter-glacial periods there are colder *stadial* periods. Isotope data from deep sea cores and ice cores show that during the last million years, the glacial cycles are 100,000 years long with growth period of about 90,000 years followed by more abrupt deglaciation period of about 10,000 years (Imbrie et al. 1984). Before the past million years or so, the periods of the glacial cycles are only 40,000 years long and can be explained by the Croll-Milankovitch astronomical theory of variations in insolation (Muller & MacDonald 1997). The last ice age in the Pleistocene ended about 9,000 years ago, and today the remaining continental ice sheets are the Greenland and the Antarctic ice sheets. According to this pattern of glacial growth and decay, the Earth will experience another ice age in around sixty thousand years or so (Peltier 2011).

1.1.3 Glacial Isostatic Adjustment of The Earth To Glacial Cycles

During the last ice age, much of northern Eurasia, North America, Greenland and Antarctica were covered by ice sheets. The ice may have been as thick as 4 kilometers during the last glacial maximum 20,000 years ago (Roy & Peltier 2015). According to Peltier (2004), the ice was 5 km thick, but it was later revised downwards (Argus & Peltier 2010, Peltier et al. 2015). The enormous weight of this ice caused the surface of the Earth to deform and downwarp under the ice load, forcing the fluid mantle material to flow away from the loaded area. At the end of the ice age, when the glaciers retreated, the removal of the weight from the depressed land led to uplift or rebound of the land and the return flow of mantle material back under the deglaciated area. Due to the high viscosity of the mantle, it takes thousands of years before the land can return to isostatic equilibrium. This process used to be called *postglacial rebound,* but recently has been replaced by *glacial isostatic adjustment (GIA)*. The reason is that the Earth's crust not only rebounds upwards underneath the area once covered by ice, but there are also sinking or more complicated vertical motions outside the ice margin. The word 'isostatic' implies that the adjustment process is very gradual and slow. In reality, the isostatic movement is punctuated by local, abrupt movements of the Earth's surface when faults are reactivated near the end of deglaciation (Dyke et al. 1991, Arvidsson 1996). Associated with the vertical land movement of GIA is horizontal motion of the land, changes in ocean surface, the Earth's gravity field, and the rotational motion of the earth (Wu & Peltier 1984, Milne & Mitrovica 1998, Peltier 1998).

1.2 STRESS AND EARTHQUAKE OBSERVATIONS

The spatial distribution and focal mechanism of intraplate earthquakes in Eastern Canada, Northern Europe, Greenland, and Antarctica provide useful observational constraints in our study of glacial induced seismicity. Currently, Greenland and Antarctica are still covered with large ice sheets and are experiencing deglaciation. On the other hand, deglaciation was essentially completed several thousand years ago in Fennoscandia (Northern Europe) and Laurentia (Eastern Canada), although glaciers are still found in Baffin Island and the High Arctic. Together, these provide important clues as to what happens in these two vastly different phases of a glacial cycle.

Earthquakes in Antarctica are rare – only 6 large events have been detected since the 1950s. The largest one (Mw8.1) was located just outside the ice margin near Balleny Island (Tsuboi et al. 2000) and is thought to have been induced by deglaciation (Gangopadhyay 2006). Three others were located near the ice margin and two smaller ones are found within the ice sheet (Fig.1.1d). In Greenland, there are many more intraplate earthquakes, but the largest earthquake detected had a magnitude of M5.5 (Voss et al. 2007). As in Antarctica, most of the earthquakes in Greenland are located near the ice margin; however, a few of them have been located in the stable interior beneath the ice (Fig. 1.1c).

In Eastern Canada (east of the Cordillera), historic earthquakes as large as M7.3 occurred in 1933 (Adams 1996). In recent years, the largest recorded earthquake was the 1988 M6.5 earthquake near Charlevoix, Quebec. Spatial distribution of recent earthquakes shows that seismic activities mainly lie along three pre-weakened tectonics zones (see Fig. 1.1a): (i) the Baffin Bay-Grand Banks Mesozoic rift margin; (ii) the Paleozoic Boothia Uplift-Bell Arch; and (iii) the Paleozoic rift along the St. Lawrence Valley-Ottawa Bonnechere Graben (Adams & Basham 1989). In Northern Europe, most of the larger (M>4) earthquakes are located near the coastal regions while the interior is relatively non-seismic with most magnitudes less than M4 (Fig.1.1b).

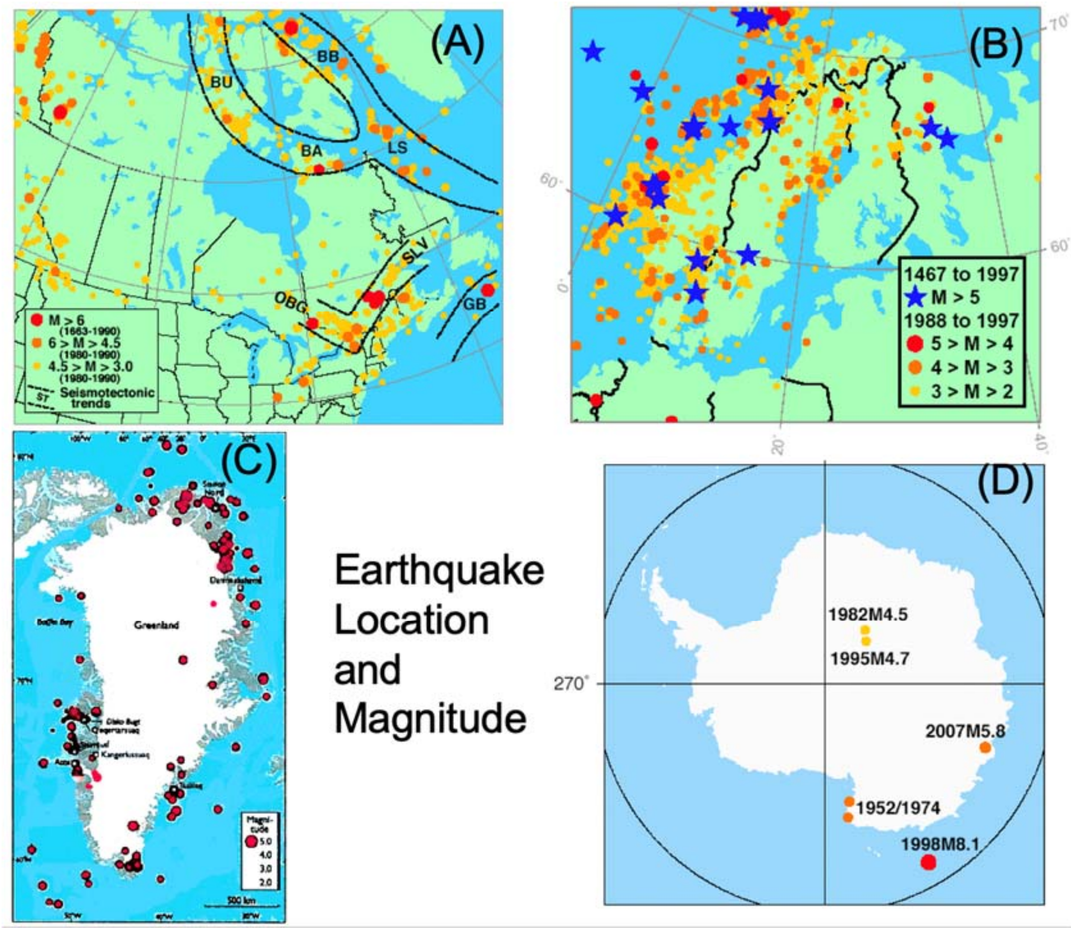

Figure 1.1: Earthquake location and magnitude in: (a) Eastern Canada, where BA=Bell Arch, BB=Baffin Bay, BU=Boothia Uplift, GB=Grand Banks, LS=Labrador Sea, OBG=Ottawa Bonnechere Graben, SLV=St. Lawrence Valley (b) Northern Europe, (c) Greenland and (d) Antarctica. (See Wu & Hasegawa 1996b, Wu et al. 1999, Voss et al 2007, Tsuboi et al. 2000).

The fault-plane solution of earthquakes tells us the orientation of the stress and the mode of failure. Unfortunately, the focal mechanism of small earthquakes is difficult to determine. Fig. 1.2 shows that thrust faulting is dominant in Eastern Canada, except in Baffin Island where the mode is normal faulting. Fig. 1.2 (ii) shows that in Fennoscandia, the mode of failure is a mixture of strike-slip, normal and thrust motion (Arvidsson & Kulhanek 1994, Slunga 1991). Along the ice margin of Greenland, the mode of failure is primarily normal faulting with some strike slip motion, while the earthquake recorded outside the Antarctic ice sheet near Balleny Island is strike-slip. For these intraplate earthquakes, strike-slip motion generally indicates that tectonic stress has a dominant contribution while thrust faulting is generally characteristic of a compressive regime inside the ice margin. Normal faulting can be attributed to the tensional stress at the peripheral bulge outside the ice margin. However, these conditions may be influenced by the background tectonic stress.

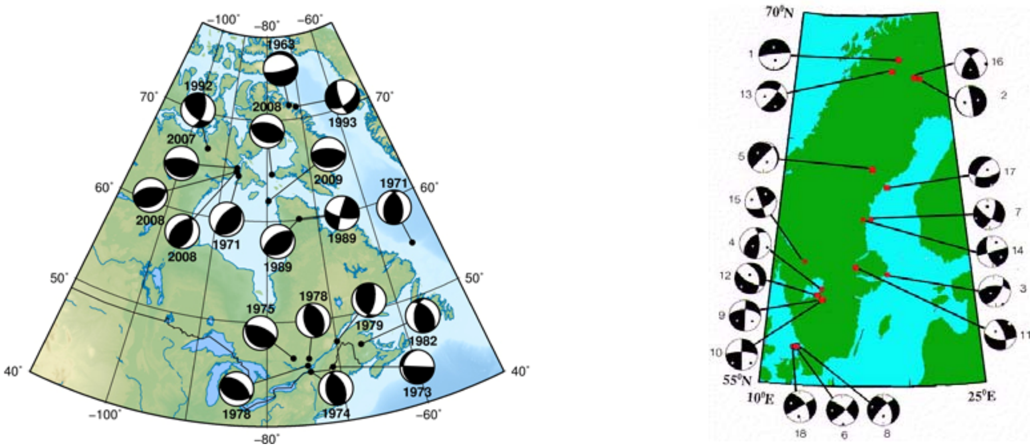

Figure 1.2: Stereographic projections of fault-plane solution of earthquakes in (i) Eastern Canada (Modified from Hasegawa et al. 1985, Steffen et al. 2021a) and (ii) Fennoscandia (Arvidsson & Kulhanek 1994).

The orientation of the contemporary stress field in Eastern Canada (see Fig. 1.3) is almost uniformly aligned along an ENE-NE azimuth (Adams & Bell 1991, Zoback & Zoback 1991, Zoback 1992a, b, Heidbach 2008) and is readily explained by the stresses associated with spreading at the Mid-Atlantic Ridge (Richardson & Reding 1991). In Fennoscandia, the near-surface stress orientation is more variable (Clauss et al. 1989, Stephansson 1989), probably due to local faults and topography. The first order maximum horizontal principal stress orientation below 300 m depth is NW-SE and is associated with the direction of ridge-push from the Mid-Atlantic Ridge (Slunga 1991, Gregersen 1992). It is now thought that the current stress field in Fennoscandia is dominated by a tectonic stress regime (e.g., Bungum et al. 2010, Pascal et al. 2010, Pascal and Cloetingh 2009).

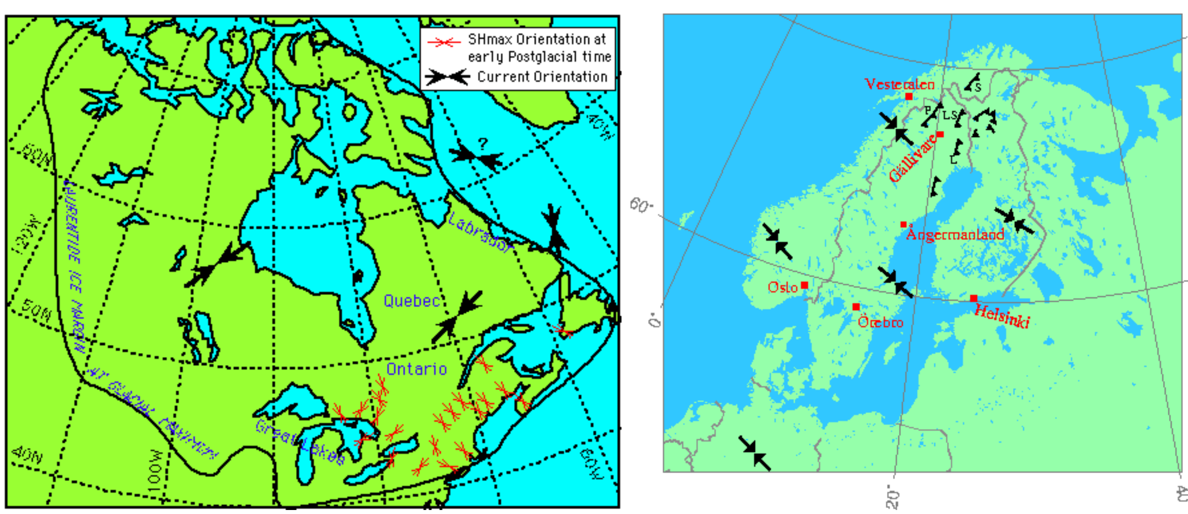

Figure 1.3: Orientation of the contemporary regional stress field (bold inward-pointing arrows). a. In Eastern Canada, the orientation of an earlier stress field deduced from postglacial faults (red thin inward-pointing arrows) is also shown (Wu 1996). b. In Fennoscandia, the location and orientation of some postglacial faults are also shown (Wu et al. 1999).

Postglacial faults have been found in both Laurentia and Fennoscandia (Fig. 1.3); (see Fenton (1994), Munier & Fenton (2004) and Steffen et al. (2021) for more detail). These faults are interpreted to have formed in postglacial times because they offset scour marks left by the moving glaciers. The throw of the postglacial faults in Fennoscandia can be as high as 15 meters (Lundquist & Lagerbäck 1976). Most of the postglacial faults in southern Laurentia have throws in the millimeters range, but a few are in the 5-50 centimeter range (Fenton 1994). In the Canadian Arctic, the Boothia Arch was reactivated abruptly near the end of deglaciation resulting in 60-120 m of local relief (Dyke et al. 1991). Such deformation can be interpreted as the movement of a postglacial fault. The postglacial faults in south-eastern Canada tell us that the orientation of the stress field during postglacial times was quite different from that of today (Adams 1989). The maximum horizontal principal stress at that time was mostly perpendicular to the ice margin (see Fig. 1.3a), but since then has rotated by about 90 degrees to the current ENE-NE direction. This indicates that the stress due to the ice sheet was dominant during postglacial times but today, tectonic stress has become the dominant stress. This amount of stress rotation has been used to constrain the viscosity of the mantle and the difference in magnitude between the maximum and minimum horizontal principal tectonic stresses (Wu 1996).

The dating of some earthquake-triggered mud slumping events in Eastern Canada indicates that earthquake activities were generated at the end of deglaciation around 9,000 years ago (Shilts et al. 1992, Dyke et al. 1991). The dating of earthquake-induced liquefaction features in the Wabash Valley, bordering Indiana and Illinois, gives an earthquake-onset time of 8 to 1 ka BP (Obermeier et al 1991). Ancient faults reactivated by glacial isostatic rebound in Fennoscandia were active about 9,000 years ago (Lundquist 1986, Lundquist and Saarnisto 1995, Muir-Wood 1989, Lagerbäck 1979, 1990, Mörner et al. 2000) and the magnitudes could have been as large as $8.2 \pm 0.2\ M_w$ (Arvidsson 1996). These onset timings have been used to discriminate between different glacially induced seismo-tectonic models (Muir-Wood 2000, Stewart et al. 2000).

Based on the above observations and modeling results, Wu & Hasegawa (1996a, b) and Wu (1997) proposed that both tectonic forces and glacially induced stress are needed to explain current seismicity and stress data in Laurentia. Past tectonic processes have created zones of weakness in which current tectonic stresses bring pre-existing faults close to failure. During glacial time, the near-surface stress induced by the glacial load in Laurentia was large enough to dictate the stress orientation while glacial unloading reactivates pre-existing faults that are critically stressed. As the stress induced by glacial unloading gradually diminishes with time after deglaciation ended, tectonic stress becomes increasingly important and is large enough to dominate the stress orientation. However, this does not mean that the stress induced by glacial unloading cannot trigger intraplate earthquakes today. In fact, earthquakes today could still be triggered by the deglaciation event 9000 years ago, and depending on the viscosity profile of the Earth, fault stability may increase or decrease over time.

The relation between rapid deglaciation (near the ice margin) and earthquakes is consistent with the observed spatial distribution of earthquakes in Greenland and Antarctica. This is further supported by the finding of Sauber & Molnia (2004) that linked rapid glacial melting in southwest Alaska to the 1979 St. Elias M7.2 earthquake.

1.3 VISCO-ELASTICITY AND THE LITHOSPHERE

In order to model the glacial isostatic adjustment process and compute the stress induced during a glacial cycle, the Earth must be treated as visco-elastic, which means rocks deform as a solid and flow like a fluid. An important consequence of this is that the stress in the mantle will relax during the glacial cycle causing stress to migrate and concentrate in the lithosphere. These concepts are reviewed and explained below.

During the 1950-60s, when the idea of plate tectonics was hotly debated, geoscientists realized that all rocks are visco-elastic; otherwise, it is impossible to reconcile how the mantle can flow like a fluid and yet can support shear waves to propagate within it (note that shear waves do not travel in a fluid). Rock physics shows that visco-elastic material can be characterized by the shear modulus, μ, and viscosity, η. When stress is applied to a visco-elastic body, it behaves like a solid if the duration of the applied stress is short compared to the Maxwell time, which is defined to be $\tau_M = \eta/\mu$. If the stress duration is longer than the Maxwell time, τ_M, then the visco-elastic body starts to flow and behave like a viscous fluid.

The viscosity of a material is determined by its temperature. This is clearly illustrated in honey, which flows under room temperature but behaves like a rigid solid when cooled in a freezer. A consequence of this is that the definition of the lithosphere, especially its effective thickness - which determines the relaxation of rebound stress, depends on the temperature and the stress duration through the Maxwell time.

The temperature near the surface of the Earth is generally colder than that at greater depth; thus, the colder outer shell of the Earth results in a very high viscosity layer (see Fig. 1.4). The viscosity of the Earth's outer shell is so high that the Maxwell time exceeds even the resident time of mountains. In other words, within this resident time period, there is little transition to fluid behavior – thus, this "elastic" layer provides support to mountains to keep them elevated and prevents them from sinking into the mantle. The actual strength of this elastic layer is limited by the fracture stress, above which brittle deformation occurs (Ranalli 1995, also see Fig. 1.5).

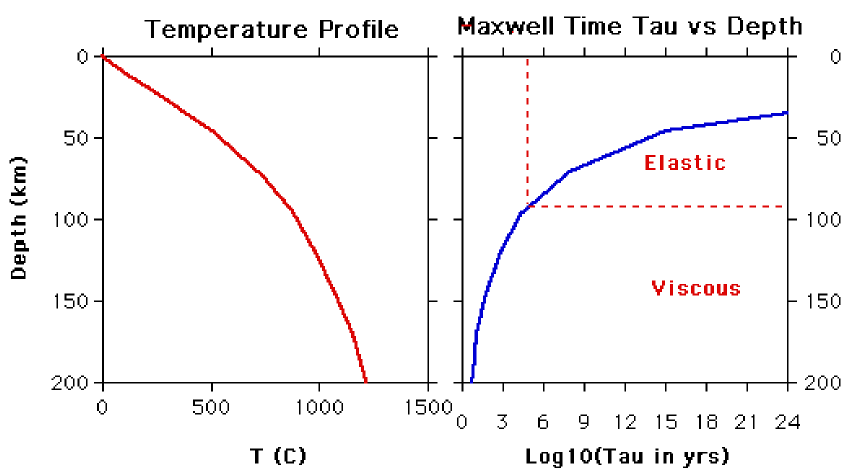

Figure 1.4: (a) Typical temperature profile in the top 200 km of the Earth. (b) Corresponding Maxwell time as a function of depth of a uniform mantle.

At greater depth, mantle temperature continuously increases (see Fig. 1.4a) and thus the viscosity and the Maxwell time both decrease exponentially with depth (Fig. 1.4b). The predicted exponential decay is due to the fact that viscosity is a thermally activated process and varies exponentially with temperature. In reality, vertical changes in chemical composition and other factors may also affect how the Maxwell time changes with depth (see Fig. 1.5).

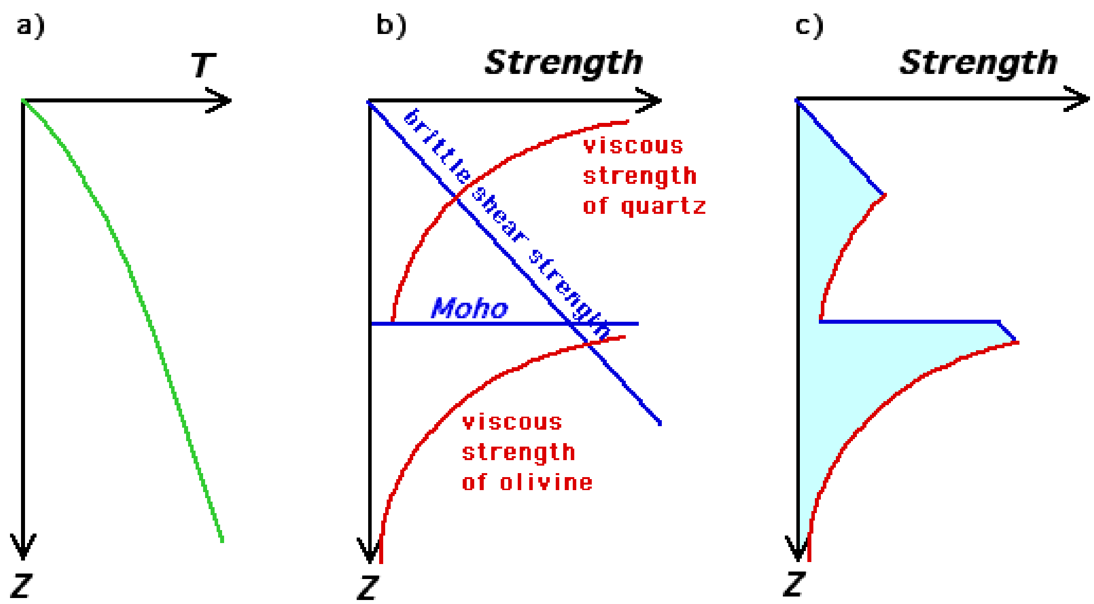

Figure 1.5: Schematic diagram of a Brace-Goetze lithosphere. a) Typical continental temperature-depth profile. b) Brittle strength and viscous strength in a 2-layer lithosphere: the composition of the crust above the Moho is assumed to be quartz and the composition of the upper mantle is olivine. The brittle shear strength (blue line) increases linearly with depth (see section 4) and the viscous strength (red curves) decreases with depth. c) Strength profile constructed from b using the fact that the deformation mechanism taken by a rock at any depth is the one that requires less stress.

For glacial loads with duration of 100 thousand years or so, the mechanically strong outer shell that does not relax to become a fluid within this period is the lithosphere seen by the glacial process. The thickness of this layer is typically of the order of 100 km or more under old and cold cratons (Fig. 1.4b). Below the base of this lithosphere, the mantle will start to creep like a fluid when the duration of the load exceeds the Maxwell time. The yield strength decreases rapidly with increasing temperature and thus is very small. The strength of this ductile layer is determined by its viscous (creep) strength (Ranalli 1995).

From a different perspective, the effective thickness of the lithosphere depends on the duration of loading. To see this, consider a load placed on the surface of a visco-elastic Earth with uniform composition (Fig. 1.4b). Immediately after loading, the whole mantle supports the load, and the whole mantle appears elastic initially. However, as the load duration increases, only the upper part of the mantle, with Maxwell time larger than the load duration, can support the load. Thus, the “elastic” part of the mantle (that can provide support to the load) continuously shrinks towards the surface as the load duration increases. As a consequence, the lithosphere ‘seen’ by glacial loads is thicker than the lithosphere ‘seen’ by mountain loading because their loads have different loading duration.

The above stress relaxation applies to a layered lithosphere as well, where there is compositional change with depth (e.g. Fig. 1.5). The added complication is the lithospheric ductile zone in the lower crust (above the Moho) which can also flow and allow stress relaxation, which will be discussed in Section 5.5.

1.4 SUMMARY

This chapter introduces some terminology and basic information about glaciers, ice sheets, ice streams, ice shelf, ice ages and the glacial isostatic adjustment (postglacial rebound) processes. It also reviews some observational data about stress orientation, earthquake distribution and mode of failure. The important ideas to remember are that: (i) faults were active around the end of deglaciation and the orientation of the postglacial faults indicates that the paleo-stress orientation in Laurentide was different from that of today; (ii) at shallow depth, rebound stress due to the ice load in Laurentide and Fennoscandia were large enough to dominate the state of stress at early postglacial time when the postglacial faults were activated; (iii) since that time, the contribution of rebound stress to the state of stress has decreased; (iv) the present-day distribution of earthquakes indicates that both rebound and tectonic stresses are responsible for the current-day seismicity. Finally, the idea of lithosphere, stress migration and upward concentration and a ductile lower crust were introduced. These ideas are important for the following discussions.

2. METHODOLOGY FOR GIA STRESS MODELING

Models have been developed to compute the spatial-temporal variation of stress due to the loading and unloading of ice sheets during a glacial cycle on a visco-elastic Earth. The methods for the computation will be briefly reviewed here, but the details can be found in the original papers.

2.1 EQUATIONS OF MOTION AND BOUNDARY CONDITIONS

The initial state of the Earth, before the application of any deforming stresses, is assumed to be in a state of hydrostatic equilibrium (see Chapter II in Cathles 1975:

$$dp_o/dr = -\rho_o g_o \tag{2.1}$$

where p_o is pressure, ρ_o is density, g_o is gravity and the subscripts 0 denote the initial state. The gravity of the initial field is related to the gravitational potential ϕ_o by *Poisson's equation*:

$$\nabla^2\phi_o = -\nabla\cdot\vec{g}_o = 4\pi G\rho_o \tag{2.2}$$

This equation states that the density distribution determines the gravitational potential and the gravitational acceleration (or gravity). The Earth model that satisfies Poisson's equation is often called self-gravitating because, when deforming stresses are applied, the movement of masses alter the local gravity and its potential (via gravitational attraction) and Poisson's equation remains valid (see equation 2.5).

The perturbed state is when deforming stresses are applied and there is motion. The motion gives rise to strain, ε_{ij}, and stress, σ_{ij}, in addition to the perturbed density ρ_1, gravity g_1 and gravitational potential, ϕ_1.

These perturbed quantities must satisfy the linearized version of Newton's law of momentum conservation (Farrell 1972, Cathles 1975, Wu & Peltier 1982):

$$0 = \vec{\nabla}\cdot\overline{\overline{\sigma}} - \vec{\nabla}\left(\vec{u}\cdot\rho_0 g_0\hat{r}\right) - \rho_0\vec{\nabla}\phi_1 - \rho_1 g_1\hat{r} \tag{2.3}$$

Note that the acceleration term on the left side of equation 2.3 is neglected because the glacial isostatic process is too slow to be of significance. The terms on the right side of the equation are the divergence of stress, the advection of pre-stress, the perturbed gravity field and the buoyancy force of local density perturbation, respectively. Here, $\hat{r}$ is a unit vector in the radial direction, and $\vec{u}$ is the displacement vector with $\vec{u}\cdot\hat{r} = u_r$.

Cathles (1975) pointed out that the advection of pre-stress term, $\nabla\left(\rho_o g_o u_r\right)$ exists only for an elastic solid and not for a viscous fluid; however, he did not clarify the role this term plays in a visco-elastic Earth. Wu & Peltier (1982) pointed out that this term is required in order that the correct boundary condition is satisfied in the viscous fluid limit. Furthermore, Wu (1992a) showed that this term provides the restoring force of isostasy and without it there will be no postglacial rebound. Wolf (1985a, b) argued that $\rho_o g_o u_r$ in the advection of pre-stress term connects the material incremental stress to the local incremental stress. This term is also important in the implementation of the equation of motion with the Finite-Element Method (Wu 2004).

Since mass must be conserved during the deformation process, the second equation used in models of glacial isostatic adjustment (GIA) is the linearized continuity equation:

$$\rho_1 = -\rho_o \vec{\nabla} \cdot \vec{u} - \vec{u} \cdot (\partial_r \rho_o) \hat{r} \tag{2.4}$$

This equation says that the perturbed density has two contributions: the change in volume of the parcel of mantle material as it moves (first term on the right side), and the change in the background density of the new environment (last term on the right). Since the Earth is self-gravitating, this perturbed density, ρ_1, causes a change in the gravitational potential and is described by Poisson's equation:

$$\nabla^2 \phi_1 = 4\pi G \rho_1 \tag{2.5}$$

Finally, the material properties of the Earth must also be included. Because the Earth is visco-elastic, and the simplest visco-elastic model that can describe the glacial isostatic adjustment (GIA) process is that of a Maxwell body, its constitutive relation between stress and strain will be used:

$$\frac{\partial}{\partial t}\sigma_{ij} + \frac{\mu}{\eta}\left(\sigma_{ij} - \tfrac{1}{3}\sigma_{kk}\delta_{ij}\right) = \lambda \frac{\partial}{\partial t}\varepsilon_{rr}\delta_{ij} + 2\mu \frac{\partial}{\partial t}\varepsilon_{ij} \tag{2.6}$$

where σ_{ij} and ε_{ij} are the stress and tensor, respectively, δ_{ij} is the diagonal tensor, λ and μ are the elastic Lamé parameters and η is the viscosity.

Equations (2.1) to (2.6) form the complete set of Equations of Motion that must be solved in order to model the deformation of the Earth. The solution that satisfies these Equations of Motion must also satisfy a specific set of boundary conditions. Although the specific boundary conditions may vary from problem to problem, the conditions common to glacial isostatic adjustment are:

(i) Continuity of gravitational potential throughout the Earth: $\left[\phi_1\right]_-^+ = 0$

(ii) At the surface of the Earth, $r = a$: $\left[\overline{\overline{\sigma}} \cdot \hat{r}\right]_-^+ = 0$, so that for normal stress $\sigma_{rr}\big|_{z=0} = -\gamma g_o$ and for shear stress $\sigma_{r\theta}\big|_{z=0} = 0$. Here, γ is the surface mass density of the applied surface load. In addition, the gradient of gravitational potential satisfies $\left[\nabla\phi_1 \cdot \hat{r}\right]_-^+ + 4\pi G \rho_o u_r = 4\pi G \gamma$.

(iii) At internal solid-solid boundaries, $\left[\overline{\overline{\sigma}} \cdot \hat{r}\right]_-^+ = 0$, so that $\sigma_{rr}\big|_-^+ = \sigma_{r\theta}\big|_-^+ = 0$. In addition, there is continuity of displacement $\left[\vec{u}\right]_-^+ = 0$ and $\left[\nabla\phi_1 \cdot \hat{r} + 4\pi G \rho_o u_r\right]_-^+ = 0$.

(iv) At the core-mantle boundary, CMB, $\left[\overline{\overline{\sigma}} \cdot \hat{r}\right]_-^+ = \rho_f g_o u_r \hat{r}$, where ρ_f is the density at the top of the fluid core and u_r is the radial displacement at the elastic-fluid boundary. In addition, shear stress vanishes at the CMB, $\left[\vec{u}\right]_-^+ = 0$ and $\left[\nabla\phi_1 \cdot \hat{r}\right]_-^+ + 4\pi G\left[\rho_o\right]_-^+ u_r = 0$.

The Equations of Motion and the boundary conditions described above are those for elastic solids, but as the visco-elastic Earth relaxes the equations and the boundary conditions for a viscous fluid will also be satisfied (Wu & Peltier 1982). This can be seen by defining the viscous stress to be:

$$\overline{\overline{\sigma}}^{V} = \overline{\overline{\sigma}} - \rho_o g_o u_r \overline{\overline{I}} \tag{2.7}$$

Equation (2.7) will turn the equations of motion and boundary conditions for an elastic solid to those for a viscous fluid. As will be seen in Section 2.2.2, this equation forms the backbone of the Coupled Laplace-Finite-Element method.

2.2 SOLUTIONS

2.2.1 Spectral Approach

The set of equations of motion that consists of partial differentiations in both time and space can be reduced to a system of ordinary differential equations by applying the following transforms. First, apply the Laplace Transform, which converts time, *t,* to the transform variable, *s*. Then, the solution in space is decomposed into its spherical harmonics or wave-number, *k*, which results in the removal of horizontal derivatives. After these transformations, the Equations of Motion can be expressed as a system of ordinary differentiation equation of order 6 – with differentiation in the radial direction only. For a radially stratified Earth, the ordinary differentiation can then be solved by the usual propagating matrix or numerical integration techniques (Cathles 1975, Peltier 1974).

Analytical solutions in the spatial *k*-domain (or for a certain spherical harmonic) exist for a few simple cases. For example, the solutions for incompressible or compressible halfspaces are given by Wolf (1985a, b) while the solution for a spherical uniform Earth is given in Wu & Peltier (1982). Perhaps, more appropriate for the study of stress, is the solution for an elastic layer over an inviscid mantle, whose solution is given by Johnston et al. (1998). This will be used to benchmark the Finite Element Method described in the following sub-section.

The solution obtained in the transformed *s* and spectral domains needs to be transformed back to the space and time domains. The inverse transform in space is straight forward (e.g., Cathles 1975), but the inversion back in the time domain is more involved. Peltier (1974) used the collocation method for time-inversion, but the result is only approximate. Commonly used is the method of Normal Modes (Wu 1978, Peltier 1976), which involves finding poles and singularities in the complex s-domain (Wu 1978, Peltier 1985, Klemann et al. 2003).

The spectral method generally works well for laterally homogeneous visco-elastic Earth models if there is no sharp change in the surface load magnitude – otherwise, the Gibbs Phenomenon can cause distortions in the solution especially near the edge of the load. Another problem is numerical instability in the integration of the ordinary differential equation, which becomes stiff for small values of the transform variable, *s* – instability in the solution arises when the 6th-order ordinary differential equation for an elastic solid becomes a 2nd-order differential equation for a fluid (Wu 1978). Another limitation of the spectral method is that it does not work well when there is strong lateral change in material properties inside the Earth; as shown in Wu (2002a), lateral heterogeneity introduces mode-coupling, making the spectral solution very difficult to implement.

2.2.2 Finite Elements & Other Numerical Approaches

The Finite-Element (FE) method is a more versatile tool because it can take into account of strong lateral variation of material properties in the Earth. Unlike the spectral method that works well only if mantle creep is linear, the FE method can also be used to model nonlinear creep flow inside the mantle.

However, for the FE method to work well, the spatial scale of the elements must be small enough that the lateral change in displacement or stress within an element is small. Otherwise, the gradient in stress and displacements cannot be resolved. Thus, the computation normally involves a large number of FE grids, and this increases the computational memory, time and cost.

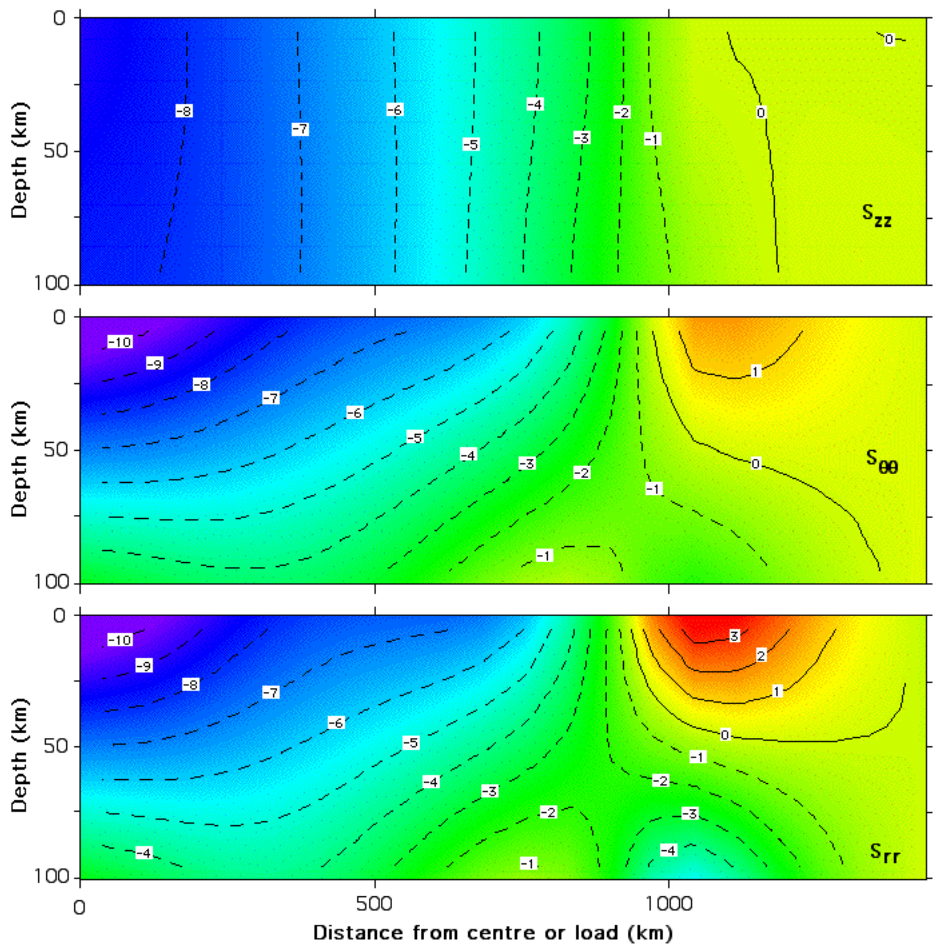

Figure 2.1: Vertical component, tangential and radial components of the material incremental stress due to the loading of an axisymmetric load of radius 1000 km with parabolic profile on an elastic plate over an inviscid mantle. The results are computed by the Finite Element (FE) technique. Comparison with Fig. 5 in Johnston et al. (1998), which is obtained with the spectral technique, demonstrates the validity of the FE technique.

There are a number of commercially available FE packages (Gasperini & Sabadini 1990, Wu 1992b); however, most commercial FE packages only solve the equation:

$$0 = \vec{\nabla} \cdot \overline{\overline{\sigma}} \tag{2.8}$$

Comparing equation (2.8) with equation (2.3) shows that the important contributions of the advection of pre-stress, the perturbed gravity field, and the buoyancy force of local density perturbation, are not included in commercial FE packages. Wu (2004) shows that using the stress transformation in equation (2.7), together with modified boundary conditions and Wrinkler

Foundations, commercial FE packages can be used to model the deformation of a non-gravitating flat Earth or a spherical, self-gravitating incompressible Earth. (See Wu 2004 & Wu et al. 2021 for more details about the method.) In addition, the sea level equations, which are important for other GIA studies (see section 3.2), can also be solved. Details can be found in Wu (2004).

For the benchmarking of the FE method, the FE solution of an ideal ice sheet with parabolic profile over an elastic lithosphere and an inviscid mantle as described in Fig.5 in Johnston et al. (1998) is computed and shown in Fig. 2.1. Comparison of this figure to the spectral solution of Johnston et al. (1998) shows that there is excellent agreement between the two methods. This validation test here and those in Wu (2004) for displacements and gravitational potential give us confidence in the continued use of this method.

Besides the finite element method, discussion of other numerical methods that are applicable are outside the scope of this report. First, there is the spectral-finite element method (e.g., Martinec 2000), which also suffers from the limitation of spectral methods when there is a sharp lateral change in the ice load or a strong lateral change in material property. Another method is the finite-volume method (Latychev et al. 2005), where the properties and motion of a 3-D volume element is represented by the values at a single node. Despite disadvantages from such simplifications, the advantage of this method is that it can easily include the effect of compressibility on internal buoyancy (Klemann et al. 2003).

2.3 SUMMARY

This section reviews the methodology in modeling the postglacial isostatic adjustment process and the computation of the rebound stress. First, the equations of motion and the boundary conditions are presented. Of particular importance are the idea of pre-stress and its advection. There are two common methods of solution: the spectral method, and the finite element method. While the spectral method can give the solution to high spatial resolution, the finite element (FE) method can take into account of lateral changes in material properties and nonlinear creep laws. Finally, stresses computed from the FE method are benchmarked with that of the spectral method, and excellent agreement is obtained.

3. SPATIAL-TEMPORAL VARIATION OF STRESS

Earthquakes can be triggered by the reactivation of pre-existing faults or by fault rupture of intact rock, however there is no evidence to suggest that earthquakes in recently deglaciated areas have ruptured intact rock. This is because stresses induced by glacial loads rarely exceeds 35 MPa while the fracture of intact rocks in the crust is generally larger than 50 MPa and typically of the order of 100 MPa (Paterson 1978, Johnson & DeGraff 1988). Thus, glacially induced stresses are not large enough to fracture intact rocks in the crust, but can easily reactivate pre-existing faults that are initially close to failure since that only require a few kPa (King et al.1994, Gomberg 1996). In this section, the spatial-temporal variation of the stress field is investigated, as this allows us to understand the reactivation or rupture of faults in the next section.

It is well known that as depth increases, the state of stress increases due to the weight of the overburden pressure (see equation 2.1) but that the increase is counteracted by the pore fluid pressure. In addition, there are many geological processes that can contribute to the state of stress. A few notable processes that result in variation of stress over time scales of millions of years or more include: fault rifting, the spreading of the ocean ridges, transcurrent fault movements, the subduction of plates, mantle flow, continental collision, movement of thrust sheets and mountain building, erosion, sedimentary basin formation, etc. On the other hand, there are much faster geological processes such as magma intrusion, volcanism, meteor impact, and surface loading of the Earth by ice and ocean water during a glacial cycle.

With so many geological processes, it seems impossible to consider all of their stress contributions in a single model. However, following Wu & Hasegawa (1996a), the stresses can be grouped together according to their time scales of variation. Because we are interested in stress variations greater than 0.1 MPa during time scales of 10 thousand years, all those stresses that take longer than 10 thousand years to change significantly can be considered as "time invariant" and the contribution for all of these time-independent stresses can be combined together and treated as the "Ambient Stress".

In the Canadian Shield or the Baltic Shield, it is not difficult to find places that are far away from active volcanism and magmatism, not recently cratered and do not experience fast erosion/sedimentation rates. In those areas, the main stress contribution with time scales less than 100 thousand years would be from surface ice/water loading and the pore fluid pressure fluctuations induced by climatic variations (e.g., glacial cycles). However, the variation of pore fluid pressure is complicated, as it depends on a number of factors that are not well understood (Finlay et al. 1984, Roots 1984, Johnston 1989, Flowers & Clarke 2002a, b, Henriksen 2008). These include: (i) whether the base of the ice sheet is wet or dry, (ii) the location relative to the ice margin, (iii) permeability of the crust and the fracture network and (iv) the largely unknown variation of hydraulic pressure beneath an ice sheet which strongly affects the stability of faults. For example, during warm periods, the glacier is full of water and the pore pressure head could reach 100% of the local weight of the ice sheet. In this report, we shall treat pore fluid pressure as time-independent to make the problem easier to solve. These preliminary results will form an important stepping-stone for interpreting more advanced studies, where time dependent pore fluid pressure is included.

Stresses are described in more detail in the following section.

3.1 AMBIENT STRESS

Ambient stresses that do not change appreciably during a glacial cycle form the state of stress before the onset of glacial cycles, and the glacial-induced stresses are superposed on top of the ambient stresses. As discussed in the beginning of this section, the ambient stress includes: regional and local tectonic stresses, overburden stress, time independent pore fluid pressure and uplift/burial induced changes to overburden pressure. In the following subsections, we shall consider each of them in more detail.

3.1.1 Overburden Stress

According to equation (2.1), the initial state where no tectonic or surface deforming stresses were applied, represents the initial stress (or pre-stress). Expressed in terms of depth *z* (which is positive downwards), equation (2.1) gives:

$$dp_o / dz = \rho_o g_o. \tag{3.1}$$

This means that if the material at some depth, z_o, has initial pressure, p_o, then the initial pressure at a deeper depth, z_o+w, is $p_o + \rho_0 g_0 w$ and ρ_o is the mean density of the rocks between the two depths z_o and $z_o + w$. Thus, we can define the vertical component of the overburden stress to be $S_V = \rho_o g_o z$. Here, we use the geologist's convention that positive values of stress mean compression.

For a flat elastic Earth where the lateral sides are constrained, the stress-strain relation of elasticity gives rise to elastic compressive stresses in the horizontal direction with magnitude (e.g., Ranalli 1995):

$$S_{horiz} = \frac{\lambda}{\lambda + 2\mu} S_V = \frac{\nu}{1-\nu} S_V = \frac{\nu}{1-\nu} \rho_0 g_0 z \tag{3.2}$$

Typically $\nu \approx \frac{1}{4}$, therefore $S_{horiz} = \frac{1}{3} S_V = \frac{1}{3} \rho_o g_o z$. The horizontal compressive stresses due to this laterally confined elastic medium is about 1/3 of the overburden pressure.

This 'lateral constrain theory' has been called into question by McGarr (1988), who favors a lithostatic state of stress in which:

$$S_{horiz} = \zeta S_V = \zeta \rho_o g_o z \tag{3.3}$$

With the overburden parameter $\zeta = 1$, this is consistent with an incompressible Earth where $\nu = \frac{1}{2}$. (For a visco-elastic Earth, the fluid limit is incompressible, so that $\zeta \to 1$ as material become more fluid like.) On the other hand, for a uniform, spherical, self-gravitating elastic Earth, the value of ζ can exceed 1, and that is more consistent with the predominance of compressive stress regimes in plate interiors (Zoback et al. 1993, Adams & Bell 1991). In this report, a range of values of ζ will be considered (see discussion in section 3.1.5).

3.1.2 Changes in overburden pressure due to sedimentation and erosion

Section 3.2 shows that stresses induced by glacial loads change by tens of MPa during the last ten thousand years. Taking the density of sediments to be 2500 kg/m^3 and gravity to be 10 m/s^2, the rate of sedimentation or erosion has to exceed 40 m/10^3 years before their induced stress changes by 1 MPa in 10,000 years. The mean sedimentation rate is typically of the order of 0.3 m/10^3 years in continental shelf and is of the order of 1 m/10^3 years in deltas and turbidities (e.g., Worm et al. 1998, Biju-Duval & Swezey 2002). On land, the sedimentation rate is generally much lower (e.g., Árnadóttir et al. 2009). For erosion, the mean erosion rate is usually smaller than 0.5 m/10^3 years in river basins (Brown & Ritter 1969) but can be much larger in coastal areas. Therefore, except in highly anomalous regions, sedimentation and erosion can be treated as time independent and their contribution to overburden negligible within the time frame of interest.

3.1.3 Pore fluid pressure

Crustal rocks are often porous, permeable and contain fluids within the pore space. If the pore fluids are interconnected, then the fluid pressure, p_f, increases with depth according to:

$$dp_f / dz = \rho_f g \tag{3.4}$$

where p_f is the mean density of the fluid. If the pore fluids are trapped within a rock formation and cannot escape, then the pore fluid pressure would be abnormally high and it rises faster than this hydrostatic pressure gradient. In any case, the pore fluid pressure opposes the compressive stresses acting on the rock matrix, so that the effective stress can be written as:

$$\sigma_{ij}^{eff} = \sigma_{ij} - p_f \delta_{ij} \tag{3.5}$$

where δ_{ij} has a value of 1 when i=j, and otherwise has a value of zero. As discussed in Section 4.1, pore fluid weakens the strength of rocks and pore fluid pressure reduces the effective normal stress on faults (see equation 4.3). As discussed earlier, the pore fluid pressure is treated as time-independent in this report.

3.1.4 Tectonic stresses

In much of North America and Europe, the main horizontal stress of continental scale is that due to the spreading of the North Atlantic Ridge (Richardson & Reding 1991). As a consequence, the maximum (compressive) horizontal principle stress, $S_{H\,max}$, in the interior of the North American Plate (See Fig. 1.3a) is in the ENE to NE direction (Zoback & Zoback 1991, Zoback 1992b). Similarly, the first order $S_{H\,max}$ orientation in Northern Europe below 300 m depth (See Fig. 1.3b) is along NW-SE (Clauss et al. 1989, Stephansson 1989, Gregersen 1992, Heidbach 2008). The orientation of the minimum (compressive) horizontal principle stress, $S_{h\,min}$, is orthogonal to $S_{H\,max}$. The magnitudes of these regional tectonic stresses are uncertain and may range from tens to hundreds of MPa. Ranges of different ($S_{H\,max}, S_{h\,min}$) combinations have been studied in Wu & Hasegawa (1996 a & b) and Wu (1996). They showed that the exact magnitude of ($S_{H\,max}, S_{h\,min}$) has little effect on fault stability studies, except for unrealistically low values of them. On the other hand, their difference $S_{H\,max} - S_{h\,min}$ is important in determining the orientation of the stress field and such. Stress difference can be constrained by the stress rotation observed since the end of deglaciation in Eastern Canada, which puts 2 < $S_{H\,max} - S_{h\,min}$< 10 MPa (Wu 1996, 1997). In tectonically pre-weakened areas where the faults are close to failure, the condition for fault equilibrium results in a relation between the stress components, which will be discussed in more detail in Section 4.3.

Superposed on the horizontal stress of continental scale are the more local tectonic stresses. For example, the eastern part of USA and southeastern of Canada experience tectonic stresses related to the Appalachian Mountains. Similarly, on the western part of North America, there is the contribution from the Rocky Mountains. In Europe, the Caledonides, the Alps and Ural Mountains all contribute stresses in addition to the continental scale tectonic stress.

Other local scale tectonic stresses include local topographic load, crustal weakening due to meteor impact, internal load due to magma intrusion, Moho uplift, rifting events, etc. Such effects perturb the regional tectonic stress magnitude and their local orientation.

In this report, only the horizontal tectonic stresses of continental scale will be included. For more local studies, all the local tectonic stresses should be included. However, as long as the time scale of these local tectonic stresses are very long compared to 100,000 years, they can be treated as time invariant and they will have little effect on fault stability (see Section 4).

3.1.5 Total Ambient Stress and Fault Regime

In view of the above discussion, the effective vertical normal stress due to overburden and fluid pressure is:

$$S_V = \rho_o g_o z - p_f = \left(1-\lambda_f\right)\rho_o g_o z \tag{3.6}$$

where $\lambda_f = p_f \big/ \rho_o g_o z$ is the pore fluid factor, which has a value of zero for dry rocks but for wet crust with hydrostatic pressure is typically 0.4 (e.g. Ranalli 1995).

If the tectonic contribution of maximum and minimum horizontal principal stress components near the surface of the Earth are $S_{H\,max}^{tect}$ and $S_{h\,min}^{tect}$, respectively, then the corresponding components for the ambient stress (away from any pre-weakened zones with fault equilibrium) are:

$$S_H = S_{H\,max}^{tect} + \zeta\left(1-\lambda_f\right)\rho_o g_o z \tag{3.7a}$$

and

$$S_h = S_{h\,min}^{tect} + \zeta\left(1-\lambda_f\right)\rho_o g_o z \tag{3.7b}$$

The value of ζ (see equation 3.3) determines how fast the horizontal stresses increase with depth relative to S_v. For example, if both $S_{H\,max}^{tect}$ and $S_{h\,min}^{tect}$ are compressive (i.e. > 0) as in Eastern Canada, then $\zeta \geq 1$ implies that $S_v < S_h < S_H$ for all depth $z > 0$. On the other hand, if $\zeta < 1$, then $S_h < S_V$ when $z > z_h$ and $S_H < S_V$ when $z > z_H$, where:

$$z_h = \frac{S_{h\,min}^{tect}}{\rho_o g_o\left(1-\lambda_f\right)\left(1-\zeta\right)} \tag{3.8a}$$

$$z_H = \frac{S_{H\,max}^{tect}}{\rho_o g_o\left(1-\lambda_f\right)\left(1-\zeta\right)} \tag{3.8b}$$

It is well known that when earthquakes occur, the mode of failure depends on whether the vertical stress is the maximum, intermediate or minimum principal stress: Thrust faulting is promoted if $S_V < S_h < S_H$, but strike-slip faulting is promoted when $S_h < S_V < S_H$ and normal faulting is promoted when $S_h < S_H < S_V$.

Thus, if both $S_{H\,max}^{tect}$ and $S_{h\,min}^{tect}$ are compressive, then $\zeta \geq 1$ implies that the fault regime that is preferred in the initial state, before any glacial cycles, is thrusting for all depths. But if $\zeta < 1$, then the fault regime preferred in the initial state, would be thrust faulting for $z < z_h$, but at deeper depth, becomes strike-slip for $z_h < z < z_H$, and finally normal faulting for $z_h < z_H < z$.

When the stresses due to glacial cycles are taken into account, there is a similar change in the fault regime with depth (see Fig. 7 in Wu & Hasegawa 1996a) except that the depths of transition between z_h and z_H being dominant are modified by the inclusion of rebound stresses.

3.2 VERTICAL STRESS INDUCED BY CHANGING WEIGHT OF ICE AND WATER

The previous subsection considers only the time-independent ambient stress, but the effects of a time-dependent surface load will be considered in this and the next subsections.

An ice sheet exerts pressure on the surface of the Earth, and the value is equal to the weight of the ice per unit area: $P(x,y,t) = \rho_{ice} g_o h(x,y,t)$, where $P(x,y,t)$ is the pressure at location (x,y) and time *t*, $h(x,y,t)$ is the ice thickness history at the location, ρ_{ice} is the mean density of the ice column and g_o is the gravitational acceleration at the Earth's surface.

For a given ice model, the surface normal stress in the vertical direction, S_{zz}, can be computed. As an illustration, the vertical stress set up by an ideal ice sheet with parabolic shape (maximum ice thickness of 1000 m) in a uniform lithosphere is shown in the upper diagram of Fig. 3.1. Note that the vertical stress does not change rapidly in the vertical direction and the lateral change in stress magnitude is due to the lateral change in ice thickness. Outside the ice margin, the vertical stress is very small, but not exactly zero.

The lower diagram in Fig. 3.1 shows the effect of changing material properties (including density) across 40 km depth. While the horizontal variation of the vertical stress, is again, determined by the ice thickness, there is a sharp decrease in the 'elastic' stress magnitude across the material boundary especially near the center of the load. Such a decrease is a consequence of the stress transformation (equation 2.7).

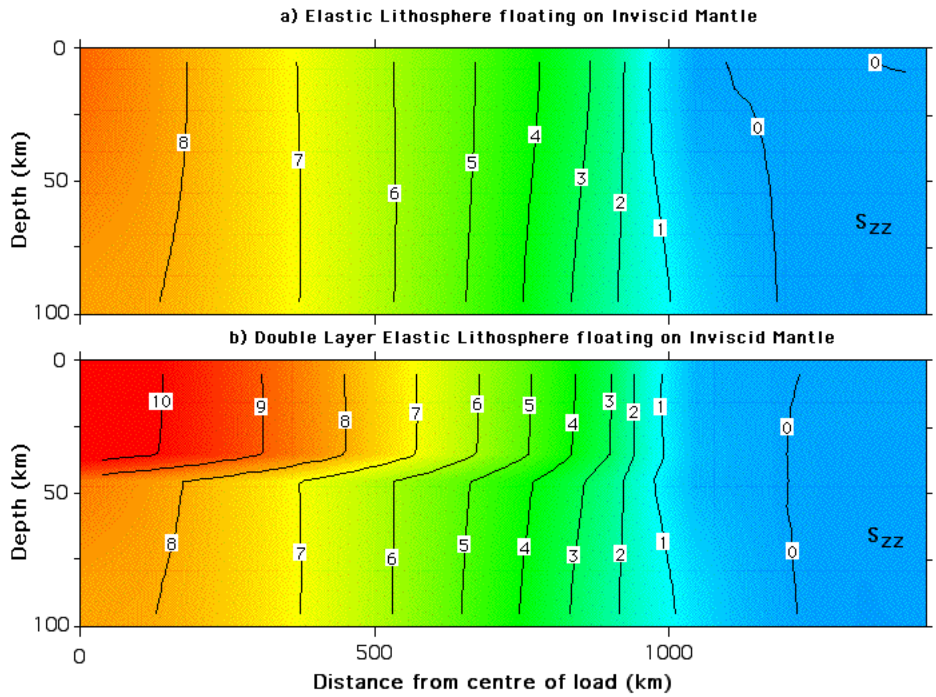

Figure 3.1: Spatial distribution of Szz (MPa) in an elastic lithosphere that floats over an inviscid mantle. The load is axisymmetric with radius 1000 km and has parabolic profile. The elastic lithosphere in the top diagram has uniform properties, while in the lower diagram, there is a change in material property across 40 km depth.

There are several more realistic ice history models. For example, in northern Europe, there is the FBKS8 ice model of Lambeck et al. (1998) and the ice dynamic model of Näslund (2006). For North America, there is the LW-6 ice model of Lambeck et al. (2017). For Antarctica, there is the thermo-mechanical ice flow model of Huybrechts (1990), the GIA based models of Ivins & James (2005), Whitehouse et al. (2012), Ivins et al. (2013). For recent global ice models, there is the ICE-4G (Peltier 1994), ICE-5G (Peltier 2004), ICE-6G (Peltier et al. 2015) and its latest revision ICE-7G (Roy & Peltier 2015). The peak ice thickness west of Hudson Bay in ICE-6G and ICE-7G is around 4000 m and is intermediate between that given in ICE-4G (~3000 m) and ICE-5G (~5000 m). Since all the global ice models ICE-XG are constrained by terminal moraine data, their predicted onset time of fault instabilities within the ice margin do not change significantly, thus we will continue to use ICE-4G in this report for illustration purpose only.

The surface values of Szz in Eastern Canada and Greenland due to the ICE-4G model at the last glacial maximum, and at 9000 years before present, are shown in Fig. 3.2. The peak magnitude is as high as 30 MPa in the southeast shore of Hudson Bay during last glacial maximum. By 9,000 years before present, most of the ice in southern Canada is gone; therefore, the vertical stress is close to zero there. In northern Canada, thin ice sheets still cover the northwest and northeast landward part of Hudson Bay and Baffin Island and, there is still substantial ice thickness in Greenland.

To form the huge continental ice sheets of the last Ice Age, water must have been taken from the oceans. At the peak of the last Ice Age, global sea-level must have fallen by about 100 meters, on average. Thus, the ocean floor experienced a negative water load on the order of 1

MPa. This is small compared to the load under the ice sheets. During deglaciation, the melted ice water returned to the oceans and loads the ocean floor. The load magnitude is, again, of the order of 1 MPa.

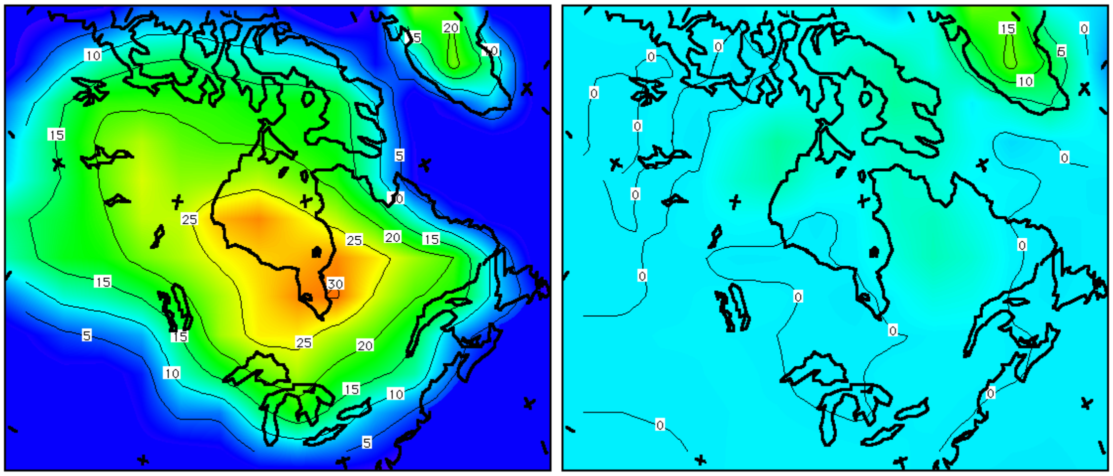

Figure 3.2: Magnitude of near surface vertical normal stress (MPa) in Eastern Canada due to the weight of the ICE-4G ice load (Peltier 1994) during (i) glacial maximum (left), (ii) 9,000 years before present (right).

It should be noted that during the Ice Age, the fall of sea level was not the same everywhere in the ocean, and after deglaciation, the amount of sea level rise is also dependent on the location and time. The reason is because sea surface is an equipotential surface and the Earth's potential is the sum of the gravitational potential and the centrifugal potential due to the Earth's rotation. Because the centrifugal potential only affects the longest (spherical harmonic of degree 2) wavelength, the shorter wavelengths of the sea surface are determined by the gravitational potential and is strongly affected by the gravitational attraction of masses nearby. For example, the massive ice sheets attract ocean water gravitationally, so water level rises by tens of meters near the edge of the ice sheet (see lower left schematic in Fig. 3.3). This raised water provides additional loading on the Earth. The deformation of the Earth's surface due to ice or melted water (see schematic on the top of Fig. 3.3) also causes mantle material to flow away from under the load to the outlying areas. This flow of mantle material also attracts sea-water gravitationally – thus, there is sea level high above the flowing mantle material. The pile of additional water also attracts nearby water gravitationally, adding further to the ocean load (see lower right schematic in Fig. 3.3).

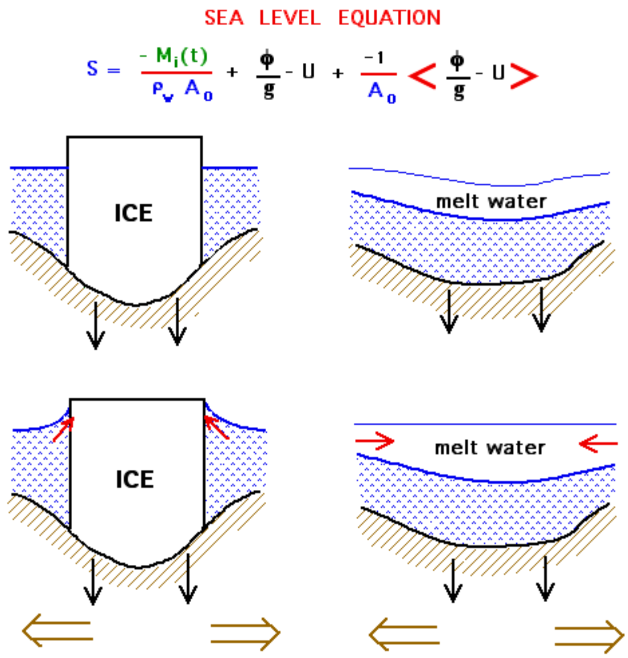

Figure 3.3: The formulation of the Sea Level Equation (Farrell & Clark 1976) takes into account the deformation of the Earth by the ice and water loads (top diagrams), the gravitational attraction between ice and water, between water and water, between water and the flow of mantle rocks and their associated deformation (bottom diagrams).

In addition, the distribution of water mass on the Earth's surface during glaciation and deglaciation, and the induced flow of mantle mass inside the Earth, cause the Earth's moments of inertia to change (Wu & Peltier 1984). As a result, the Earth's rotation changes, and sea level with the longest wavelength is also affected by the induced change in the centrifugal potential (Milne & Mitrovica 1998).

In order to find out how the water load is distributed spatially during glaciation and deglaciation, one has to solve the Sea Level Equation (Farrell & Clark 1976, Milne & Mitrovica 1998, Peltier 1998), which takes into account the ice-water, water-water and mantle-water attractions, their loading effects and rotational feedback.

The result of such an exercise shows that while these effects are significant and cannot be neglected in the study of sea level change, their effects on the vertical stress is relatively minor and the water load can be approximated by assuming that water masses enter the ocean uniformly - that is, the sea level change is the same everywhere in the ocean. This is the ice-equivalent sea level approximation (Milne & Mitrovica 1998) and will be adopted for the rest of the report. According to this approximation, the incremental load on the ocean floor at time t $\Delta L_{ocean}(t)$ is related to the incremental increase in the global ice mass, $\Delta M_{ice}(t)$, surface gravity ,g_o, and the total area of the ocean floor A_{ocean} given by:

$$\Delta L_{ocean}(t) = -\frac{g_o \Delta M_{ice}(t)}{A_{ocean}} \tag{3.9}$$

3.3 HORIZONTAL STRESSES INDUCED BY THE WEIGHT OF ICE AND WATER

Besides inducing vertical stress, the weight of the ice and water loads also induces horizontal stresses. This is because a rigid lithosphere exists on the outer part of a visco-elastic Earth. Unlike the vertical stresses, whose time variations are dominated by the variation of the surface load magnitude (i.e., from weight of ice and water), the time dependence of the horizontal stresses is determined by the creep of mantle and lithospheric rocks.

3.3.1 Lithosphere in a visco-elastic Earth and stress migration

As discussed in the Introduction, the Earth is visco-elastic and the effective thickness of the lithosphere depends on the duration of loading. As the residence time of the surface load increases, the "elastic" part of the mantle continuously shrinks upwards as the lower part can no longer support the load elastically. As a consequence, stress magnitude in the upper elastic part will increase with time during loading. This accounts for the upward migration and concentration of stress in the lithosphere.

However, some studies find it convenient to represent the Earth as an elastic lithosphere (or plate) of a certain thickness overlying an inviscid fluid mantle. However such a model fails to take into account the upward migration and concentration of stress and the result is only valid in the viscous limit - when all stresses below the lithosphere have relaxed completely. We shall briefly consider such a case, as it does provide some physical insight into the stresses due to the bending of a lithosphere.

3.3.2 Bending of an elastic lithosphere over inviscid fluid mantle

It is well known that a surface load applied to an elastic lithosphere floating on a fluid can cause the loaded area to bend downwards, but outside the load, a peripheral bulge may form (Fig.3.4). Due to the downward bending, which results in a concave upward lithosphere, material in the shallow part of the lithosphere becomes compressed and at the bottom of the lithosphere the material becomes stretched. On the other hand, at the top of the peripheral bulge where the plate concaves downwards, the lithosphere is stretched and there is tension. The bottom of the lithosphere material undergoes compression. Somewhere near the middle of the lithosphere, there is a plane where material is neither compressed nor dilated. This is the neutral plane. The normal stress to a surface, whose normal lies parallel to the neutral plane, is called fiber or bending stress. Under the assumption of Thin Plate Theory, that is the lithosphere is very thin compared to the horizontal dimension of the load, a simple relation between fiber stress magnitude and the vertical displacement, *w*, can be found (e.g. Turcotte & Schubert 1982). This has led early investigators (e.g., Walcott 1970, Stein et al. 1979, Quinlan 1984) to employ such a model for the computation of horizontal stresses due to glacial loading.

Numerical experiments that compare the results of Thin Plate Theory and the exact solution show that Thin Plate Theory breaks down if the radius of the load is less than 1.5 times the flexural wavelength *l*, which is defined by:

$$l = \left(\frac{EH^3}{12\left(1-\nu^2\right)\left(\rho_m - \rho_f\right)g_o} \right)^{1/4} \qquad (3.10)$$

Here, H, E, ν, ρ_m, ρ_f and g_o are lithospheric thickness, Young's Modulus, Poisson's ratio, density of the mantle, density of the fill (sediment, water or air) on top of the deformed surface, and the gravitational acceleration, respectively. For typical values of E, ν, ρ_m, (e.g., from PREM model), with values of H between 50 and 150 km and values of ρ_f between 0 to 2000 kg/m^3, the minimum radius of the load for Thin Plate Theory to work varies between 120 to 350 km. Thus, Thin Plate Theory will not work well for the smaller ice sheets (e.g., in British Isles, Iceland).

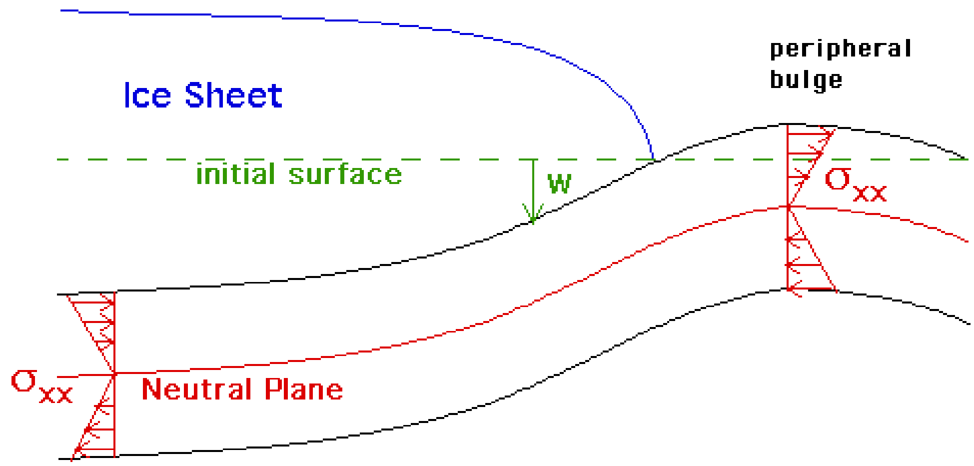

Figure 3.4: Lithospheric Flexure. When an ice sheet loads the Earth, there is downward flexure under the load (with displacement w) and the formation of a peripheral bulge outside the ice margin. Due to the bending of the lithosphere, fibre stresses underneath the load are compressive at the deformed surface, but decrease to zero at the neutral plane and become extensional all the way down to the bottom of the lithosphere. Under the peripheral bulge, the fibre stresses are extensional at the surface but become compressive below the neutral plane.

The solution for a uniformly thick elastic plate floating on an inviscid mantle was calculated and provided in Johnston et al. (1998). Fig. 3.5 shows the spatial variation of fiber stress inside the lithosphere when the load is a parabolic ice sheet with radius of 1000 km. As expected, the neutral plane is near the middle of the lithosphere. Compressive stresses are found under the majority of the load, but changes to tension at the bottom of the lithosphere. Near the edge where the ice thickness becomes small and outside the margin where the peripheral bulge lies, there is tension near the surface, which changes to compression at the bottom. These findings for the Thick Plate solution are very close to what is expected in Thin Plate Theory because the load radius is wide compared to the thickness of the lithosphere.

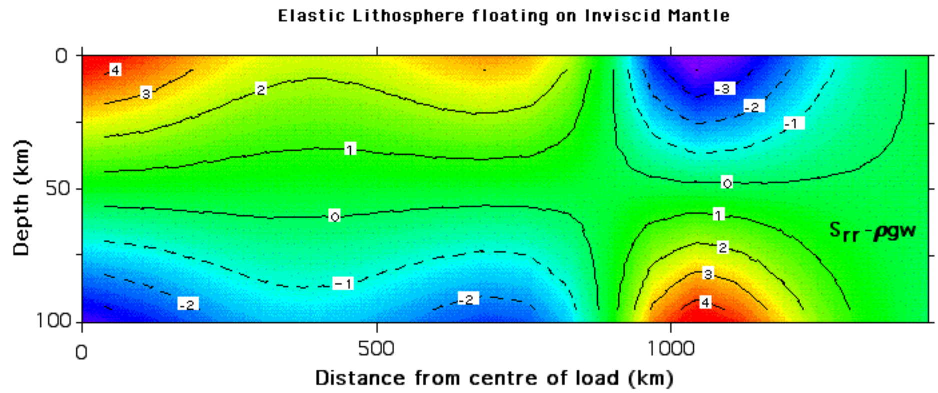

Figure 3.5: Fiber Stress (MPa) distribution in an elastic lithosphere due to the loading of an axisymmetric load of radius 1000 km with parabolic ice profile (maximum ice height 1000 m) on an elastic plate over an inviscid mantle. See Table 1 in Johnston et al. (1998) for details. These thick plate results are computed by the Finite Element (FE) technique.

It should be noted that for this lithospheric model, the response of loading is time-independent – as soon as the load is applied, the lithosphere bends into the final shape and the stress imposed as in Fig. 3.5. After removal of the load, the bending and the stress completely disappear.

Another point is that the fiber stress is a local incremental stress and does not take into account the Advection of Pre-stress. During the deformation, the state of stress would contain the initial pressure carried along with the displaced material (see p. 89 in Love 1911), plus some stress that arises from the new strain induced by the deformation (fiber stress here). The value of the initial pressure has no time to change for an elastic deformation (see p.13-14 in Cathles 1975); thus, rock material that is displaced upwards by *w* will see an extra pressure of $\rho_o g_o w$ when compared to its new surroundings. The new stress state would be the initial pressure at the *new* location plus $\rho_o g_o w$, plus the local incremental stress induced by the deformation (fiber stress here). In other words, the perturbed state at the new location would be $\rho_o g_o w$ plus the local incremental stress. From now on, this perturbed state at the new location will be presented.

Finally, as pointed out in the previous subsection, this simple model does not include the support provided by the mantle or the concentration and migration of stress in the lithosphere as the visco-elastic mantle relaxes. This is considered in the following section.

3.3.3 Horizontal Stress in an Elastic Lithosphere that lies over a Visco-elastic Mantle

In order to illustrate the idea of stress migration, an Earth model that includes both the elastic lithosphere and the relaxation of the underlying visco-elastic mantle is constructed. The lithosphere has uniform material properties and is 100 km thick. The mantle is considered as a uniform visco-elastic halfspace with viscosity of 10^{21} Pa·s. First, we consider a simple case with an axisymmetric parabolic load of 1000 km radius, which is applied at time t=0, and left there for 5,000 years before it is removed instantaneously.

The horizontal stress, S_{rr}, is in the radial direction and consists of the sum of the fiber stress and the Advection of Pre-stress. The latter can be represented as $\rho_o g_o w$, where *w* is the vertical displacement at the location. The spatial distribution of S_{rr} within the lithosphere during the loading phase is shown in Fig. 3.6 for t=0 ka and at 5 ka after the Heaviside application of the load. Immediately after the load is applied (t=0 ka), the whole mantle supports the load elastically and the surface deformation is small - as is the magnitude of the fiber stress. Thus, S_{rr} is dominated by the Advection of Pre-stress term. The lower diagram is at 5,000 years after the application of the ice load, when the mantle has experienced significant relaxation and, consequently, there is concentration and magnification of stress in the upper part of the lithosphere. The fiber stress at this time is becoming similar to that shown in Fig. 3.5 of the last subsection.

When the ice load is suddenly removed after 5,000 years, the spatial distribution of S_{rr} within the lithosphere is shown in the top of Fig.3.7. Comparing with S_{rr} immediately before the removal of the ice load (Fig. 3.6), the greatest change is observed directly underneath the load due to the removal of the load induced elastic displacement and the release of the compressive bending stresses. At t=10,000 years (or 5,000 years after the removal of the ice load), the lithosphere further unbends itself and there is also migration of stress from the mantle thus, the stress at the base of the lithosphere changes more quickly than the top.

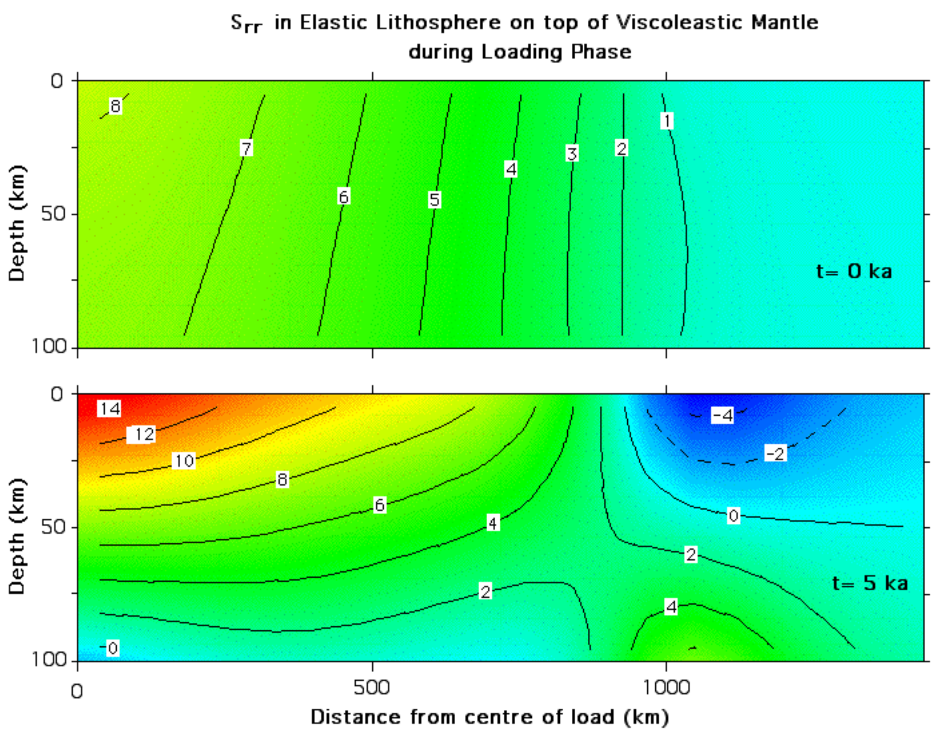

Figure 3.6: Spatial distribution of Horizontal Stress S_{rr} (MPa) in a 100 km thick elastic lithosphere which is on top of a uniform visco-elastic mantle. The load is axisymmetric with parabolic profile and radius of 1000 km.

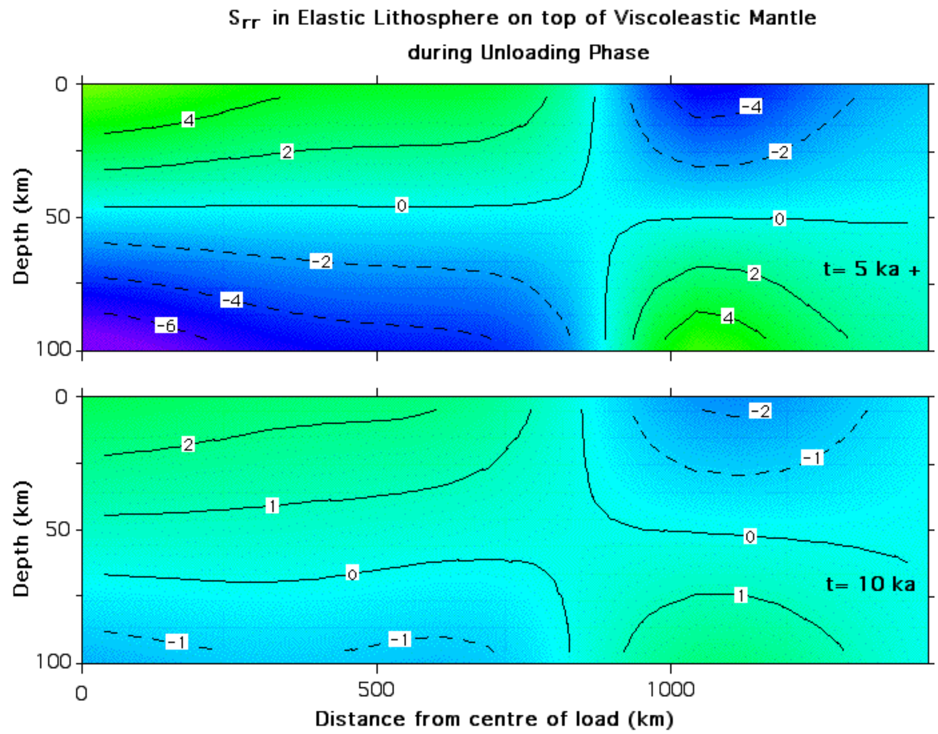

Figure 3.7 Spatial distribution of Horizontal Stress S_{rr} (MPa) in a 100 km thick elastic lithosphere which is on top of a uniform visco-elastic mantle The top diagram is immediately after removal of the parabolic ice load and the lower diagram is 5,000 years after the removal of the ice load.

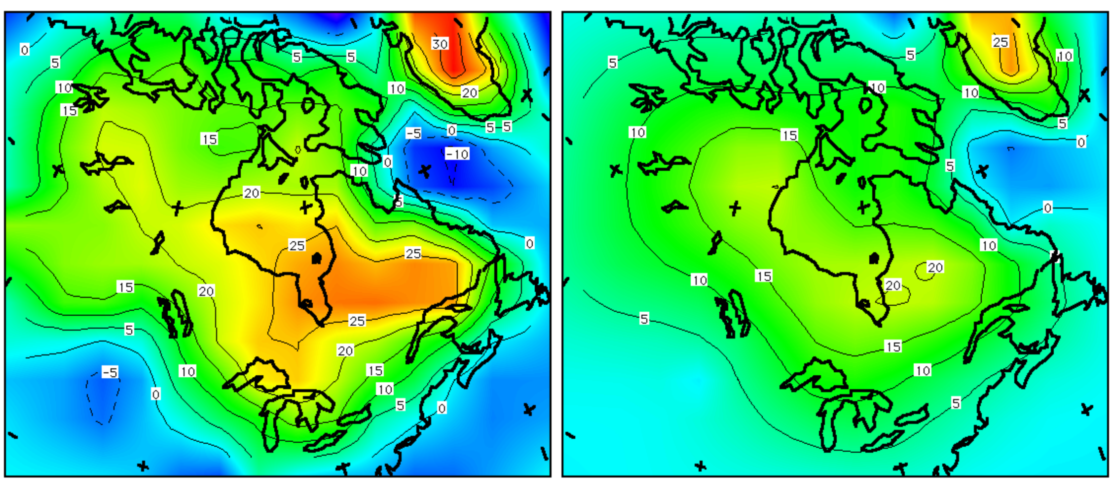

Figure 3.8: Typical magnitude of near surface Maximum Horizontal Principle Stress (MPa) induced by ICE-4G glacial loading/unloading in Eastern Canada during (i) glacial maximum (left) & (ii) 9,000 years before present (right).

The analysis above can be extended to a more realistic ice and Earth model. Fig. 3.8 shows the spatial variation of the near surface maximum horizontal principle stress induced by glaciation at the last glacial maximum in Eastern Canada at 9,000 years before present. The deglaciation history is described by ICE-4G. The stratified Earth includes a uniform 120 km thick lithosphere with upper mantle viscosity of $6\text{x}10^{20}$ Pa·s shallow lower mantle viscosity of $1.6\text{x}10^{21}$ Pa·s from 700 to 1200 km depth, and deep mantle viscosity of $3.0\text{x}10^{21}$ Pa·s from 1200 km to the Core-Mantle-Boundary. Similarly, Fig. 3.9 shows the spatial variation of the near surface minimum horizontal principal stress at the last glacial maximum and at 9,000 years before present (BP).

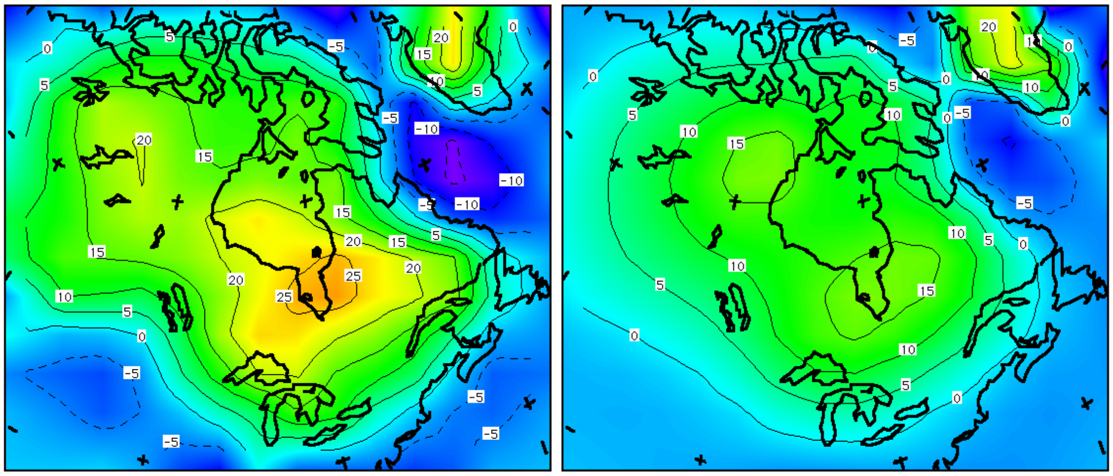

Figure 3.9: Typical magnitude of near surface Minimum Horizontal Principal Stress (MPa) induced by ICE-4G at the last glacial maximum (left) and at 9,000 years before present (BP)(on the right).

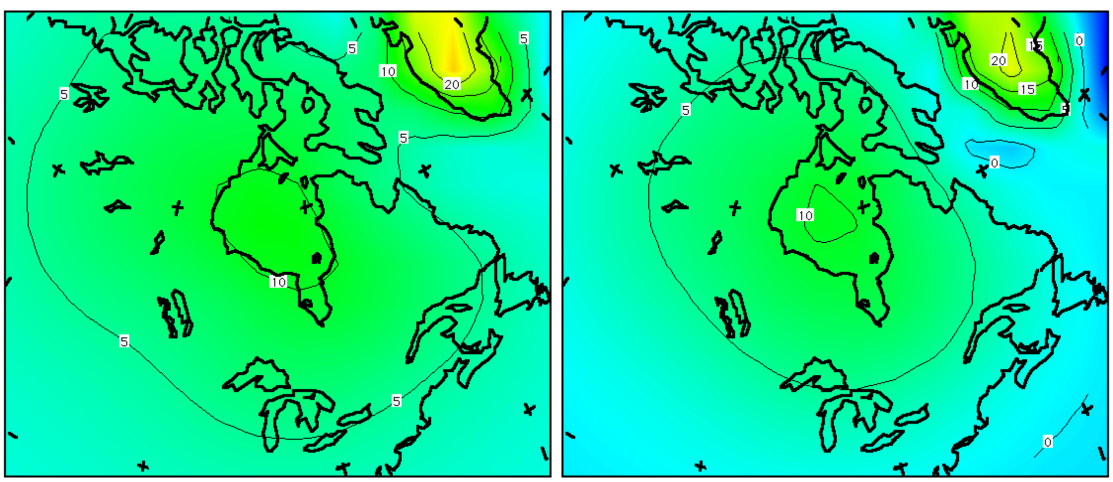

Figure 3.10: Magnitude of present day near surface (i) Maximum & (ii) Minimum Horizontal Principle stress (MPa) induced by glacial unloading in Eastern Canada.

Comparing the near surface maximum horizontal principle stress (Fig. 3.8) with the vertical normal stress (Fig.3.2) at the last glacial maximum shows that except for some spots near the ice margin, the vertical normal stress is generally larger in magnitude. However, by 9,000 years BP, the ice load and the vertical normal stress have significantly decreased, while the maximum and minimum horizontal principle stresses remain large in magnitude. Fig. 3.10 shows that the magnitude of the horizontal stresses remains large even at present, and is due to the slow creep of mantle and lithospheric rocks.

3.4 SHEAR STRESSES INDUCED BY GLACIER FLOW

Besides the weight of the ice sheet, which gives rise to vertical and horizontal stresses in the Earth, glacial flow may be able to transmit shear stresses from the flowing glacier onto the surface of the Earth (i.e., bedrock) by the basal drag, which is the friction between the bedrock and the base of the moving ice in the vertical shear deformation of the sheet ice.

Glaciers flow the fastest when there is decoupled basal sliding at the ice-bed interface. In that case, little or no shear stress is transmitted to the bedrock. Thus, it is incorrect to assume that fast glacial flows or glacial surges can transmit higher shear stress in the Earth. Ice shelves, which consist of floating ice spreading on top of water, is an extreme example where no basal drag exists. In the case of stream ice, basal drag is also small because there is very little basal coupling, or the coupling is through some subglacial sediment where all the shear stresses are concentrated. The question is how large is the basal drag under grounded sheet ice?

The dynamics of glaciers are driven by the down-slope component of gravity τ_d:

$$\tau_d = -\rho_{ice} g_o H \frac{\partial h}{\partial x} \tag{3.11}$$

where H is the ice thickness and h is the elevation of the ice surface. In the x-component of the force balance equation for glacier dynamics (e.g. equation 3.2.12 of Van der Veen 1999):

$$\tau_{dx} = \tau_{bx} - \frac{\partial}{\partial y} \int_{h-H}^{h} R_{xy} dz - \frac{\partial}{\partial x} \int_{h-H}^{h} R_{xx} dz \tag{3.12}$$

Here, the x-component of the driving stress (τ_d) is balanced by that of the basal drag (τ_b) and by lateral drag if the glacier is bounded laterally by rock or slower moving ice (second term on the right hand side of equation 3.12) and also by the longitudinal gradient of the longitudinal normal stress (third term on the right).

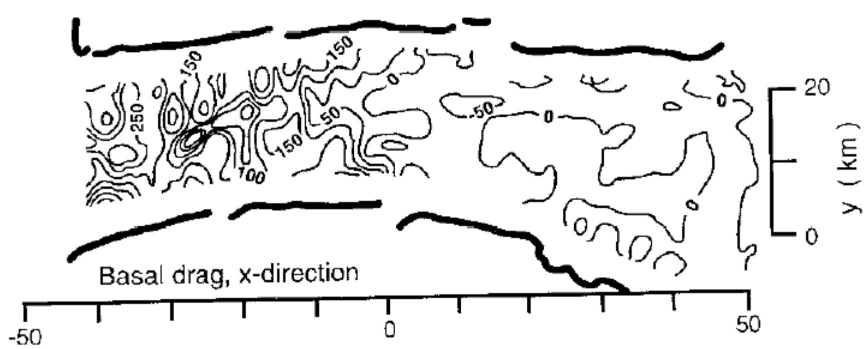

Figure 3.11: Basal drag on Byrd Glacier in East Antarctica computed from the force balance equation. Contour interval is 50 kPa (After Whillans et al. 1989).

From this force-balance equation (3.12), the basal drag (τ_b) can be estimated if a power-law relation between stress and strain with stress exponent n=3 is used and the surface velocities of the glaciers are measured. Using this method, Whillans et al. (1989) computed the basal drag (τ_b) on Byrd Glacier in East Antarctica. Their results show that τ_b is zero under the floating ice-shelf (above which the surface flow velocity reaches 800 m/year), but under the grounded part, where the glacier is frozen to its bed with zero basal sliding, τ_b is larger and is concentrated at isolated spots with magnitude as high as 0.25 MPa (see Fig. 3.11).

The basal stresses estimated in this way may be under-estimated (Van der Veen 1999). To obtain the maximum value of τ_b, one can take the lateral drag and the longitudinal gradient term to be zero in the force-balance equation (3.12), which makes (τ_b) equal to the driving stress τ_d. Whillans et al. (1989) showed that τ_d has maximum value around 0.4 MPa in the Byrd Glacier. The true peak value of the basal drag is likely to lie somewhere between 0.25 to 0.4 MPa and these peak values are concentrated in a few isolated spots (see Fig. 3.12).

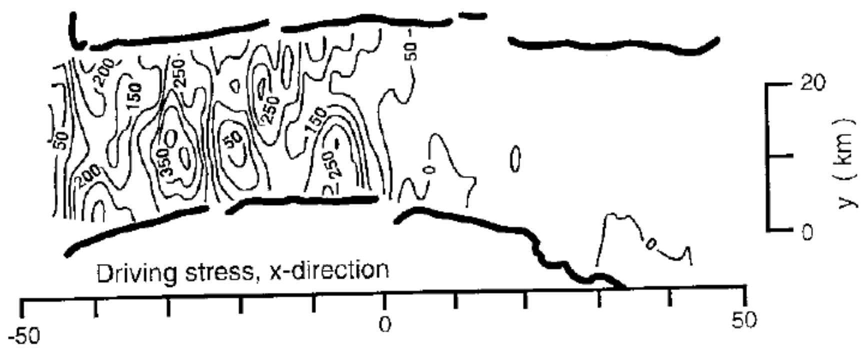

Figure 3.12: Computed driving stress on Byrd Glacier in East Antarctica. Contour interval is 50 kPa (After Whillans et al. 1989).

Van der Veen (1999) summarized the relationship between basal drag and the ratio between surface velocity and ice thickness for several glaciers. He showed that the Byrd Glacier has the largest basal drag among them (see Fig. 3.13). On the other hand, the Jakobshavn outlet has the highest surface velocity to ice thickness ratio, but the basal drag is at least half of that found under the Byrd Glacier. The ice flow velocity in Jakobshavn Isbrae is higher than 1500 m/year (Joughin et al. 2008).

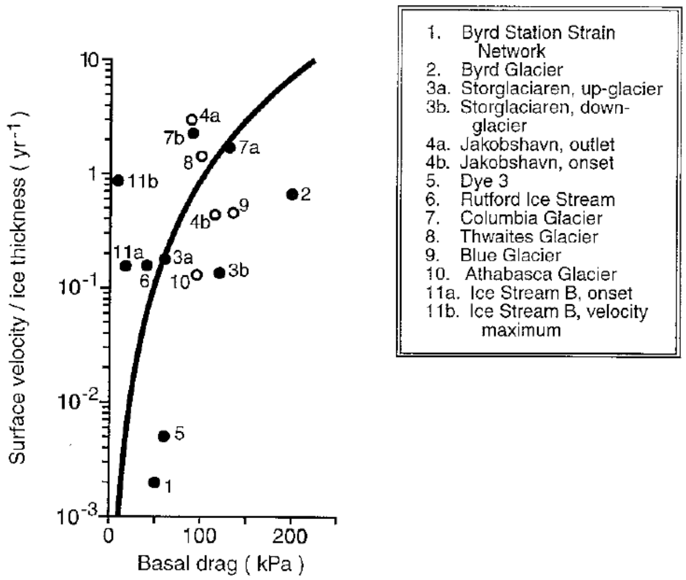

Figure 3.13: Relationship between basal drag and the surface velocity divided by the ice thickness. Open circles represent basal drag estimated from the driving stress, while those estimated from force balance are represented by solid circles (After Van der Veen 1999).

In Figure 3.13, a power-law between strain rate and stress, with stress exponent n=3, is assumed ($R_{ij} = B\dot{\varepsilon}_e^{(1-n)/n}\dot{\varepsilon}_{ij}$). However, in the past, glacier flow has been treated as a problem in plasticity. What that means is that the stress exponent $n \to \infty$. Physically, this means that there is no deformation if the applied stress is below the yield stress (τ_o). However, as soon as the yield stress is reached, the material deforms immediately to relieve the applied stress. In other words, the stress in the material never exceeds the yield stress and, thus, the maximum basal stress $\tau_b = \tau_o$. Using this assumption, the ideal equilibrium profile of a perfectly plastic ice sheet resting on a flat bed is shown to be parabolic:

$$H = H_o\sqrt{1-\frac{x}{L}} \tag{3.13}$$

Here, x is the horizontal distance from the ice divide, *L* is the half-width of the ice sheet, and H_o is the maximum thickness, given by:

$$H_o = \sqrt{\frac{2\tau_o L}{\rho g}} \tag{3.14}$$

By fitting the parabolic ice profile to glaciers, the yield stress (τ_o) is found to be around 0.1 to 0.2 MPa, which is of similar magnitude than that obtained for Byrd Glacier.

The above discussion shows that basal drag is likely to be smaller than 1 MPa. Since the stress magnitude in simple shear is largest at the surface, the shear stress inside the Earth would be well below this level and thus would be small compared to that due to either the weight of the ice sheet during glaciation or the horizontal (bending) stresses after deglaciation. Therefore, the contribution of shear stress due to glacial flow is neglected in the following discussion.

3.5 SUMMARY

For the purpose of this study, it is convenient to express the total stress that triggers fault instability as the sum of 'time independent' ambient stress and time - dependent rebound stresses induced by glacial cycles.

The total ambient stress, which includes contributions from overburden stress, pore fluid pressure and tectonic stress, can generally be expressed by equations (3.6), (3.7a) and (3.7b). Depending on the value of $\zeta = S_h / S_V$, a depth-dependent stress regime is setup by the ambient stress.

The vertical stress induced by glacial cycles in the lithosphere is mainly determined by the weight of the ice load. Due to the presence of the lithosphere and a visco-elastic mantle, horizontal stresses are induced. The main contributions at seismogenic depths are from lithospheric flexure due to changing weight of the surface load and the migration of stress from below. The relaxation of the horizontal stresses is determined by the creep of mantle and lithospheric rocks – a process which occurs over thousands of years. Finally, shear stress due to glacier flow has been shown to have a very small contribution to the state of stress inside the Earth.

4. BRITTLE FAILURE OF ROCKS AND FAULTING MECHANISMS

Earthquakes are generated by the brittle failure of rocks that result in the sudden release of stored energy in the form of seismic waves, which give rise to the shaking ground motion. Brittle failure can result in the creation of new faults in intact rocks, or to frictional sliding along a pre-existing fault. In both cases, the friction along the fault plane is important to the formulation of the Failure Criterion.

4.1 MOHR-COULOMB FAILURE CRITERIA

According to Coulomb, failure occurs when the shear stress along a fault plane exceeds a certain critical value τ_c:

$$|\tau_c| = S + \mu\sigma_n \tag{4.1}$$

where μ is the internal coefficient of friction, σ_n is the normal stress applied to the fault plane, and *S* is the cohesion strength. What this equation says is that as σ_n increases, the fault is pressed more tightly together by the normal stress and, thus, larger shear must be applied to overcome the friction.

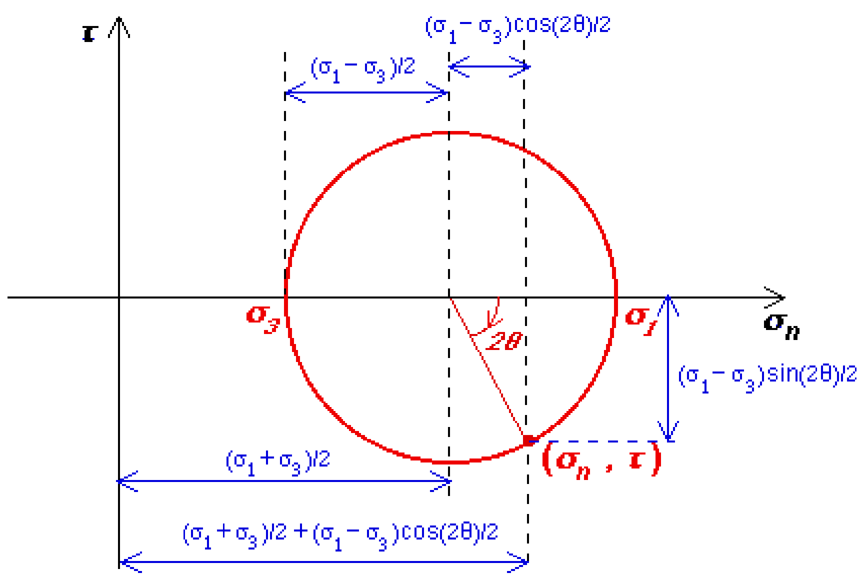

Figure 4.1: Mohr's Circle for the state of stress is a relationship between normal stress σ_n and shear stress τ that acts on a fault plane with normal oriented at angle θ with respect to the maximum principal axis.

Mohr considered a fault plane under a state of compressive stress where the maximum and minimum principal stresses are σ_1 and σ_3 respectively. When the normal of the fault plane makes an angle (θ) relative to the σ_1 axis, the normal stress acting on the fault plane is σ_n and the shear stress is τ (See p. 108 in Malvern (1969) for a discussion of the often-confusing choice of sign conventions for shear). By plotting σ_n against τ for all angles $-\frac{\pi}{2} \le \theta \le \frac{\pi}{2}$, a circle is traced out in the $\sigma_n - \tau$ space (see Fig. 4.1). The center of the circle is located at $(\sigma_n, \tau) = \left(\frac{\sigma_1 + \sigma_3}{2}, 0\right)$ and the radius of the circle is $\frac{\sigma_1 - \sigma_3}{2}$. From the geometry in Fig. 4.1, it is clear that for a given orientation of a fault plane (angle 2θ), σ_n and τ on this fault can be determined from:

$$(\sigma_n, \tau) = \left(\frac{\sigma_1 + \sigma_3}{2} + \frac{\sigma_1 - \sigma_3}{2} cos(2\theta), -\frac{\sigma_1 - \sigma_3}{2} sin(2\theta)\right) \tag{4.2}$$

From this, it can be seen that at $\theta = -\pi/4$ with $(\sigma_n, \tau) = \left(\frac{\sigma_1 + \sigma_3}{2}, \frac{\sigma_1 - \sigma_3}{2}\right)$, so that the maximum shear stress is $\tau_{max} = \frac{\sigma_1 - \sigma_3}{2}$.

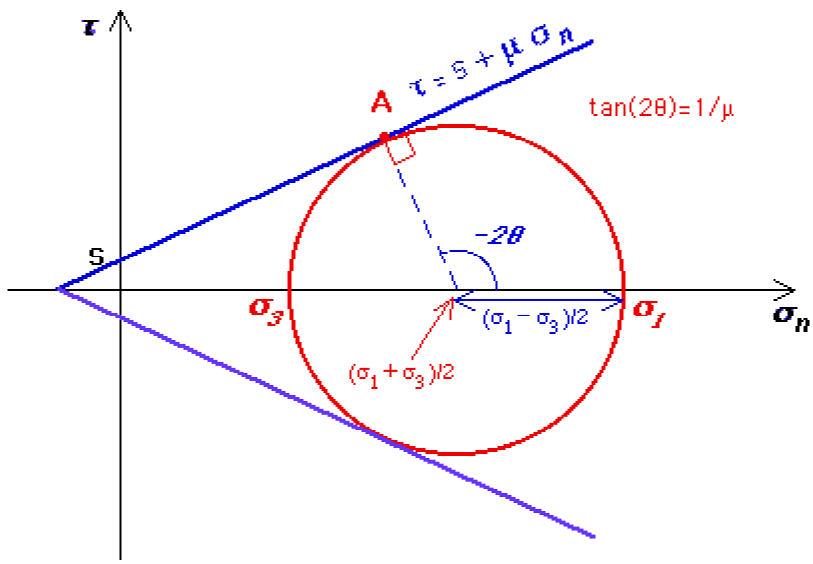

Figure 4.2: The sloping lines represent Coulomb's failure criterion. Brittle failure occurs at point A where the Mohr circle touches the line of failure with critical stresses (σ_{nc}, τ_c). See text for more detail.

According to the Coulomb-Mohr theory, failure does not occur when maximum shear stress is reached. The reason for this is that the normal stress, which presses the fault planes together, is much larger in magnitude ($\sigma_n = \frac{\sigma_1 + \sigma_3}{2}$). Instead, failure occurs at the point where the Mohr circle touches the Failure Envelope $|\tau| = f(\sigma_n)$ as in Fig. 4.2. For most practical applications, the Failure Envelope can be approximated linearly by an equation in the same form as equation (4.1). Because the line of failure is tangent to the Mohr circle, the orientation of the conjugate fault plane is "optimally oriented" and θ is given by: $tan(2\theta) = 1/\mu$ (e.g., Ranalli 1995, p.100).

In terms of the principal stresses, the frictional law (with S=0) can be written as (e.g., Ranalli 1995, p.246): $\frac{\sigma_1}{\sigma_3} = \left(\sqrt{\mu^2+1}-\mu\right)^2$ (see equation 4.8 below).

When failure occurs, the mode of failure can be normal-faulting, strike-slip or thrust-faulting depending on whether the vertical stress is the maximum, intermediate or minimum principal stress, respectively (see Fig. 4.3).

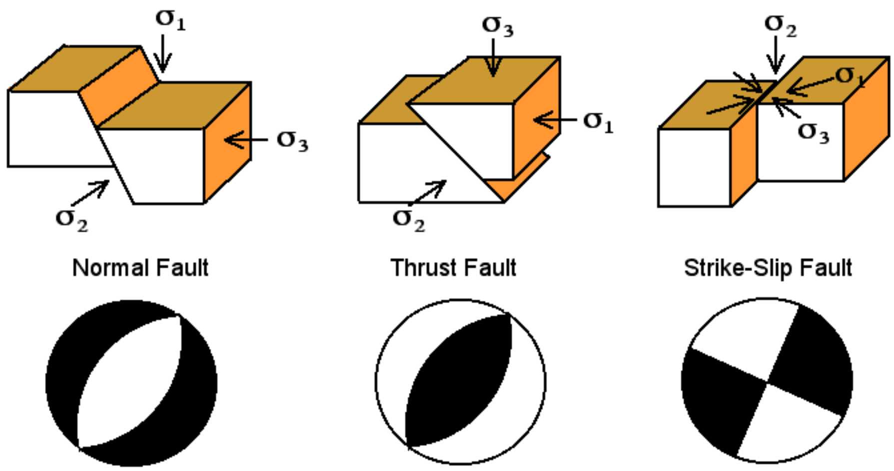

Figure 4.3: The three main types of faults and their focal mechanism. In the top panels, σ_1, σ_2 and σ_3 are the maximum, intermediate and minimum principal stresses, respectively. The fault regime depends on which of the principal stresses is vertical. In the lower panel, the beach balls represent earthquake focal mechanisms - the area colored black represents tension and white represent compression.

The presence of fluid greatly reduces the cohesion strength (S) and slightly reduces the internal coefficient of friction (μ). The pore fluid pressure (p_f) acts in opposition to the normal stress, so that the Mohr-Coulomb criterion becomes:

$$\left|\tau_c\right| = S + \mu\left(\sigma_n - p_f\right) \tag{4.3}$$

If the normal stress is approximately lithostatic ($\sigma_n \approx \rho_o g_o z$), then $\left|\tau_c\right| = S + \mu\rho_o g_o z\left(1-\lambda_f\right)$,

where $\lambda_f = \frac{p_f}{\rho_o g_o z}$ as before (see equation 3.6).

4.2 BYERLEE'S AND AMONTON'S LAWS

If pre-existing faults exist in a rock, and there is no cohesion, equation (4.1) becomes:

$$\tau_c = \mu\sigma_n \tag{4.4}$$

This is Amonton's law.

Byerlee (1978) found empirically that $\mu = 0.85$ for shallow depth (with pressure below 200 MPa). However, at greater depth, brittle failure occurs under the criteria:

$$\tau_c = 60MPa + 0.6\sigma_n \tag{4.5}$$

This is Byerlee's law.

If the normal stress is lithostatic ($\sigma_n \approx \rho_o g_o z$), then the critical frictional strength can be estimated as a function of depth. Again, in the presence of fluid pressure p_f, then Byerlee's laws can be reformulated as:

$$\tau_c = 0.85\sigma_n\left(1-\lambda_f\right) \quad \text{and} \tag{4.6a}$$

$$\tau_c = 60MPa + 0.6\sigma_n\left(1-\lambda_f\right) \tag{4.6b}$$

4.3 ANDERSON AND SIBSON'S EXTENSION OF MOHR-COULOMB LAW

In this section, we consider one of the principal stress directions is vertical and the other two principal stress directions are horizontal. This is similar to that considered in section 3.1.5, where it is shown that the preferred stress regime in the initial state may change as a function of depth. The question is how large must the stress difference be in order that failure occurs. Using the Mohr-Coulomb criterion, Anderson (1951) and Sibson (1974) showed that the required stress difference depends on depth and the stress regime, which is closely related to the orientation of the activated fault. Stüwe (2007) summarized them as follows:

(i) Thrust faults:
$$\sigma_1 - \sigma_3 = \frac{2S + 2\mu\rho_o g_o z\left(1-\lambda_f\right)}{\sqrt{\mu^2+1}-\mu} \tag{4.7a}$$

(ii) Normal faults:
$$\sigma_1 - \sigma_3 = \frac{2S + 2\mu\rho_o g_o z\left(1-\lambda_f\right)}{\sqrt{\mu^2+1}+\mu} \tag{4.7b}$$

(iii) Strike-slip faults:
$$\sigma_1 - \sigma_3 = \frac{2S + 2\mu\rho_o g_o z\left(1-\lambda_f\right)}{\sqrt{\mu^2+1}} \tag{4.7c}$$

When there is no cohesion (S=0), the above can be written in a more compact form (Ranalli 1995):

$$\sigma_1 - \sigma_3 = \alpha\rho_o g_o z\left(1-\lambda_f\right) \tag{4.8a}$$

where
$$\alpha = \begin{cases} R-1 & thrust \\ \dfrac{R-1}{R} & normal \\ \dfrac{R-1}{1+\delta\left(R+1\right)} & strike-slip \end{cases} \quad \text{and} \quad R = \frac{1}{\left(\sqrt{\mu^2+1}-\mu\right)^2}$$

(4.8b)

Here the intermediate principal stress is $\sigma_2 = \sigma_3 + \delta(\sigma_1 - \sigma_3)$, with $0 < \delta < 1$.

Fig. 4.4 shows the stress difference required for faulting at the optimally oriented fault plane is a function of depth, stress regime and two values of pore fluid pressure ratios (λ_f=0.0 and 0.9). One should caution that equations (4.7) and (4.8) are derived for an optimally oriented fault at failure; so, in stable areas away from the fault (e.g. above or below the fault and in lateral areas next to the fault), these equations do not apply. The formulation above has been extended to anisotropic rocks by Ranalli & Yin (1990) and Yin & Ranalli (1992).

Lund et al. (2009) pointed out that in order for faults in tectonically pre-weakened zones to be close to failure (or at fault equilibrium), the principal background stresses at the fault must obey either equation (4.7) or (4.8) depending on whether S is negligible. However, in earlier reports (Wu 1996, 1997), the background stress is assumed to be given by equations (3.6) and (3.7) so that equations (4.7) or (4.8) may not be satisfied at the fault plane. Wu & Hasegawa (1996b) found that as long as the stress regime does not change, the magnitude of the background stress does not strongly affect the conclusion on fault stability. Indeed, recent work where the magnitude of the background stress for a given stress regime is constructed according to equations (4.7) or (4.8) confirms that this previous finding on fault stability remains unchanged.

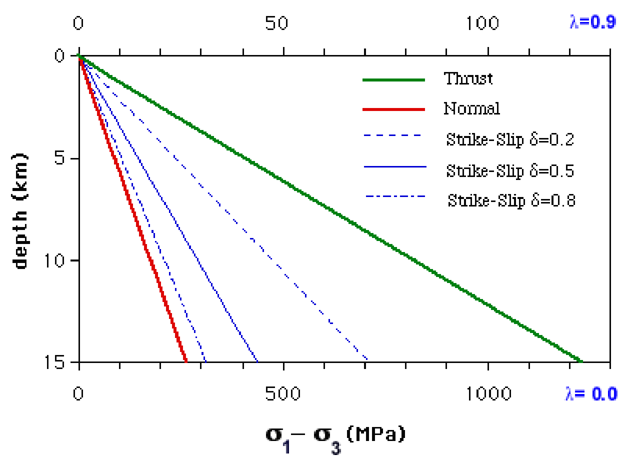

Figure 4.4: Stress differences required for faulting in 3 different stress regimes are shown for two values of pore fluid pressure: horizontal axis at the bottom is for no pore pressure (λ_f=0) and the one at the top is for high pore pressure (λ_f=0.9). The lines for strike-slip faulting with different values of intermediate principal stress (determined by the value δ) lies within those lines for thrust faulting and normal faulting.

4.4 MOHR-COULOMB CRITERIA AND CHANGES IN FAULT STABILITY MARGIN

For the rest of the report, the total stress field consists of the time-dependent rebound stresses induced in glacial cycles, superimposed on the time-independent ambient stresses which include tectonic stress, overburden stress and static pore fluid pressure. Because Anderson and Sibson's extension of the Mohr-Coulomb criteria is for a state of stress that is at failure, the stress relationships in equation 4.7 cannot be applicable throughout the glacial cycle, since the time - dependent total stress field causes the faults to move in and out of failure.

This is illustrated in Fig. 4.5 for sites within the ice margin. During glacial loading, the increased weight of the ice sheet increases the mean stress below the ice load, but the change in stress difference is generally small (see Figs. 3.2, 3.8 & 3.9). As a result, the center of the Mohr circle moves to the right but the radius generally remains almost the same for the larger ice sheets (e.g., Laurentide, Fennoscandian and Antarctica ice sheets). As Mohr's circle moves away from the line of failure (Johnston 1987, 1989), preexisting faults become more stable regardless of whether the stress regime is thrust, normal or strike-slip. For smaller ice sheets (e.g., British Isles), stress amplification of σ'_1 (Johnston et al. 1998) causes the radius of the Mohr circle to increase much more than the mean stress, leading to fault instability, especially near the ice margin (see discussion in Section 5.1). After the end of deglaciation, the horizontal principal stress remains large, even when the weight of the ice sheet disappeared (see Figs. 3.2, 3.8 & 3.9) – this is due to the slow decrease of the horizontal bending stresses which are controlled by viscous flow beneath the unbending lithosphere. For a thrust regime, where the vertical stress is the minimum principal stress, the stress difference, or the radius of the Mohr's circle increases, but the vertical stress returns to its initial value before the glacial cycle. Mohr's circle comes closer to failure or actually reaches failure, after deglaciation (see Fig. 4.5b). For strike-slip regimes where the vertical stress is the intermediate principal stress, flexure causes both σ_1 and σ_3 to increase – as a result, there is not much change towards failure (Fig.4.5c). For normal faulting, where the vertical stress is the maximum principal stress, the fault is also more stable than the initial state (see Fig.4.5d).

Steffen et al. (2021) studied the relative motion between the Mohr circle and the line of failure for sites extending from outside the ice margin to the peripheral bulge. They found that for the thrust-regime, fault stability prevails outside the ice margin– the only exception is after the end of deglaciation and for sites just outside the ice margin but not far enough to be close to the peak of the peripheral bulge. For normal and strike-slip regime, the Mohr's circle moves towards the line of failure for all sites outside the ice margin during glaciation, deglaciation and even after the end of deglaciation – the only exception is after the end of deglaciation for sites just outside the ice margin.

In order to quantify the effect of glacial loading on the stability of faults (i.e., whether Mohr's circle gets closer to or moves away from the line of failure), the Fault Stability Margin (*FSM*) is defined. It is the shortest perpendicular distance from the line of failure to the Mohr circle (see Fig. 4.5) and represents the stability of an optimally oriented fault. It is related to the principal compressive stresses by (Johnston 1989):

$$FSM = \beta\left[\mu\left(\sigma_1 + \sigma_3\right) + 2S\right] - \tfrac{1}{2}\left(\sigma_1 - \sigma_3\right) \quad (4.9a)$$

and

$$\beta = \frac{sin\left[tan^{-1}(\mu)\right]}{2\mu} = \frac{1}{2\sqrt{1+\mu^2}} \quad (4.9b)$$

Note that the value of cohesion, *S*, is basically unknown and cannot be measured without disturbing its value. As mentioned earlier, it's value is generally large for intact rocks, but varies with location and depth; for pre-existing faults, its value is small (Brace & Kohlstedt 1980, Zoback & Healy 1984), but still varies from fault to fault and can change within a fault. This makes determination of the value of *FSM* difficult.

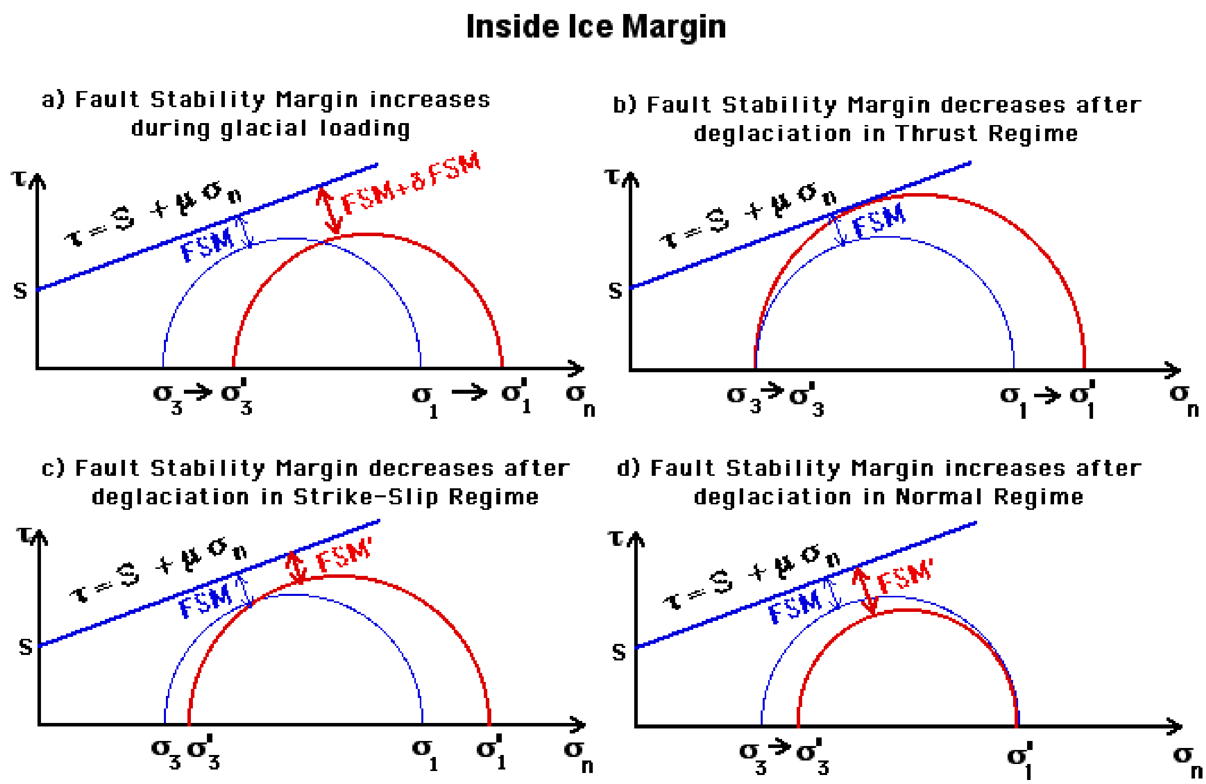

Figure 4.5: Fault Stability Margin and its change during a glacial cycle for a site inside the ice margin of a large ice sheet. σ_1 and σ_3 are the maximum and minimum principal stresses of the ambient stress field before a glacial cycle, but the primed quantities are those for the total (ambient and glacial) stress field during glacial loading (a), and after deglaciation in (b) thrust, (c) strike-slip and (c) normal fault regime.

Lund & Slunga (1999) also Steffen et al. (2021) used a similar measure of fault instability, except that it is the vertical distance (along τ axis in the Mohr diagram) to the line of failure from the fault's location on the Mohr circle:

$$FS_\tau = \tau - \tau_c = \tau - S - \mu\sigma_n \qquad (4.10)$$

Because we are only interested in the effect of glacial cycle on the stability of faults, Wu & Hasegawa (1996a) proposed to study instead the Change of the Fault Stability Margin, i.e. $\delta FSM(t) = FSM(t) - FSM(t_o)$ at time *t* relative to that at initial time t_O (before any glacial cycles):

$$\delta FSM(t) = \tfrac{1}{2}\{[\sigma_1(t_o) - \sigma_3(t_o)] - [\sigma_1(t) - \sigma_3(t)]\}$$
$$+\mu\beta\{[\sigma_1(t) + \sigma_3(t)] - [\sigma_1(t_o) + \sigma_3(t_o)]\} \qquad (4.11)$$

A positive value of δFSM means that the changing stress moves the Mohr Circle away from failure and the fault becomes stabilized. A negative value of δFSM means that the fault moves towards instability while its magnitude gives an indication of the stress available for faulting. The advantage of computing δFSM can be seen by inspecting equation (4.11), which shows that it is independent of the cohesion (*S)*. Note that the first curly brackets on the right contain the change in the stress difference or radius of the Mohr circle, while the last curly brackets contain the change in the center of the circle. Thus, time-independent isotropic stress, such as pore fluid pressure or overburden, with $\zeta = S_h / S_V = 1$, has no effect on its value.

The basic premise for computing $\delta FSM(t)$ is as follows. Glacial loading generally results in fault stability (Fig.4.5a). Stresses induced by glacial unloading (see Figs. 3.8, to 3.10) are not large enough to fracture intact rocks. Thus, glacial unloading will generally activate only pre-existing faults that are initially close to failure. Because past tectonics have created pre-weakened zones in Eastern Canada, Northern Europe and Antarctica (Fig 1.1), there are plenty of pre-existing weak faults with different orientations within these areas. The presence of a real fault or a fault system generally affects the magnitude and orientation of the state of stress nearby and that complicates the matter. Thus, we first consider the pre-existing faults to be “virtual faults”, in that their presence does not affect the state of stress (a more realistic treatment will be discussed in section 6). Since the pre-existing faults are created by ambient tectonic stress, the value of *S* along these faults (see equations 4.9a or 4.10) should be much smaller than that of intact rocks and the Mohr circle at these faults should generally not be too far from failure initially (before glacial loading). During a glacial cycle, if $\delta FSM(t)$ has a positive value, the Mohr circle moves farther from the line of failure and thus stability is promoted. On the other hand, if $\delta FSM(t)$ has a negative value, then the Mohr circle moves closer to failure (see Fig.4.5). The potential for failure depends on the initial value of *S*, how close to failure the fault was initially and the orientation of the fault. **Optimally oriented faults**, (i.e. that satisfy $\tan(2\theta) = 1/\mu$) that are initially close to failure before the onset of glaciation are the first to fail as $\delta FSM(t)$<0 (see Fig. 4.5b). On the other hand, if the fault is not optimally oreiented, the Mohr circle has to rise above the line of failure (see Fig. 4.6) for that fault to fail. If the fault was not near failure initially, then a more negative value of $\delta FSM(t)$ is needed to bring it to failure. If it is not large and negative enough, failure may not occur (see Fig. 8-8 in Lund 2005).

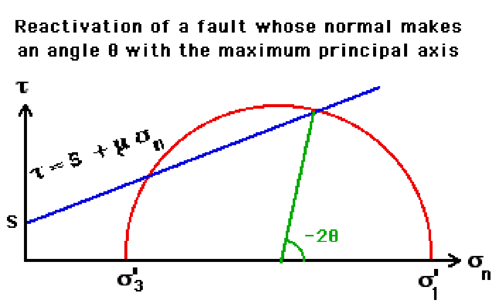

Figure 4.6: Failure for a fault that is not optimally orientated.

Wu & Hasegawa (1996) and Lund (2005) noted that the optimally oriented faults at the initial time (t_o) may not be the same as that at time t, because the maximum principal stress (σ_1) and its orientation may change in time. For example, if there is no ambient tectonic stress, then near the center of the Laurentide ice sheet during glacial maximum, σ_1 is vertical in southeast Hudson Bay (see Fig.3.2, & 3.8). However, by 9,000 BP, σ_1 has become horizontal. If the magnitude of the principal horizontal ambient tectonic stresses are large enough, however, then this will not happen.

4.4.1 Computation of δFSM

Following section 3.1.5 the total stress is defined to be the superposition of the stresses induced by the glacial cycles (commonly called rebound stress and hence superscript R), the tectonic stresses and the vertical normal stress due to overburden and fluid pressure. For the horizontal components:

$$\sigma_{ij}(t) = \sigma_{ij}^R(t) + S_{ij}^{tect} + \zeta\rho_o g_o z(1-\lambda_f)\delta_{ij} \tag{4.12a}$$

and for the vertical components:

$$\sigma_{3j}(t) = \sigma_{3j}^R(t) + \rho_o g_o z(1-\lambda_f)\delta_{3j} \tag{4.12b}$$

Note that only the rebound stresses are assumed to be time dependent (see discussion in section 3.1) and have zero values before the glacial cycles and at the initial time $\sigma_{ij}^R(t_o) = 0$. Also, for faults that are close to failure before the onset of glaciation, the time independent principal background stresses must obey either equation (4.7) or (4.8).

In general, we first compute the time variations of the 6 components of the rebound stress for a given ice and Earth model at a fixed seismogenic depth (taken to be 12 km unless specified) and location (longitude and latitude). Then, for each location and time, the rebound stresses are combined with the tectonic stresses and overburden stress, as shown in equation (4.12), to give the 6 total stress components. Next, the tensor for the total stress is diagonalized numerically to obtain the 3 principal stresses (eigen-values) and the orientation of the principal axis. The principal stresses are used to compute δFSM from equation (4.11). The history of δFSM for various locations is then examined for fault stability changes. In general, none of the 3 principal stresses align exactly with the vertical, especially near the surface, although one of them generally lies within a few degrees from it. The orientation of the principal axis is important in the determination of the mode of failure. The principal stresses that are not close to vertical are projected onto a horizontal plane to determine the orientation of the two horizontal principal stresses.

4.4.2 Example with ζ=1

For illustrative purpose, we will compute δFSM for a 2D case and show that as long as ζ=1, δFSM is independent of any time - independent pressure term.

The principal stresses in a 2D case are related to σ_{ij} by:

$$\sigma_1 = \frac{\sigma_{11}+\sigma_{33}}{2} + \sqrt{\frac{1}{4}\left(\sigma_{11}-\sigma_{33}\right)^2 + \sigma_{13}{}^2} \tag{4.13a}$$

$$\sigma_3 = \frac{\sigma_{11}+\sigma_{33}}{2} - \sqrt{\frac{1}{4}\left(\sigma_{11}-\sigma_{33}\right)^2 + \sigma_{13}{}^2} \tag{4.13b}$$

Using equation (4.12) in (4.13a), (4.13b) and (4.11), it can be shown that:

$$\begin{aligned}\delta FSM(t) = \mu\beta\left\{\sigma_{11}^R(t)+\sigma_{33}^R(t)\right\} + \sqrt{S_{13}{}^2 + \tfrac{1}{4}\left(S_{11}-S_{33}\right)^2} \\ -\sqrt{\left\{\sigma_{13}^R(t)+S_{13}\right\}^2 + \tfrac{1}{4}\left\{\sigma_{11}^R(t)-\sigma_{33}^R(t)+S_{11}-S_{33}\right\}^2}\end{aligned} \tag{4.14}$$

Thus, δFSM is independent of lithostatic and fluid pressures as long as they are time - independent (see Wu & Hasegawa 1996a).

4.5 MOGI-VON MISES FRACTURE CRITERIA

Instead of the Coulomb Failure criteria, Ivins et al. (2003) considered the Mogi-von Mises failure in which the shear stress is generalized to the octahedral shear stress:

$$\tau_{oct} = \tfrac{1}{3}\sqrt{\left(\sigma_1-\sigma_2\right)^2 + \left(\sigma_1-\sigma_3\right)^2 + \left(\sigma_2-\sigma_3\right)^2} \tag{4.15}$$

and the failure criterion is:

$$\tau_{oct} < a\left(\frac{\sigma_1+\sigma_3}{2}\right)^n \tag{4.16}$$

For triaxial experiments with amphibolite, and with the unit of stress in MPa, Chang & Haimson (2000) found that $a \approx 1.77$ and $n \approx 0.86$.

The difference between Mogi-von Mises and Coulomb failure criteria is large. According to Ivins et al. (2003), at 9 km depth, τ_{oct} at failure is ~220 MPa, but the shear stress at the fracture is only 128 MPa at Coulomb failure.

When the change in Fault Stability is computed with Mogi-von Mises failure, its value differs from δFSM by a factor of 1.5 to 2, but otherwise the conclusion about the timing, location and mode of fault reactivation are insensitive to the choice of the failure criteria. Thus, the Mogi-von Mises failure will not be considered further in this report.

4.6 SUMMARY

In the beginning of this section, we reviewed the concept of Mohr's circle, Mohr-Coulomb criterion for the failure of intact rocks or pre-existing faults, and the mode of failure. Anderson and Sibson's extension of Mohr-Coulomb law is also reviewed briefly in Section 4.3; however, these extensions are only applicable at failure but during a load cycle the faults are not always at failure. The fault stability margin (FSM) and its changes (δFSM) are shown to be suitable for the study of fault stability due to glacial cycles. The premise is that the virtual faults are initially close to failure. During the glacial cycle a positive value of δFSM means that fault becomes more stable, while a negative value of δFSM means that fault is becoming unstable. For faults that are optimally oriented and critically stressed initially (i.e. $FSM\left(t_o\right)=0$), failure can occur when δFSM becomes zero. For faults that are not optimally oriented but critically stressed initially, δFSM has to fall further below zero so that the Mohr circle with that orientation can touch the line of failure (Fig. 4.6). Other measures of fault stability are also reviewed, but they give similar predictions about timing, location and mode of fault reactivation. Thus, only δFSM is considered further in section 5.

5. FACTORS THAT AFFECT FAULT STABILITY:

In Section 3, we reviewed time-independent ambient stresses and the time-dependent stresses induced during a glacial cycle for large ice sheets, such as the one in Laurentia. In Section 4, we reviewed measures of fault stability. In this section, we shall review some factors that affect the stability of faults – namely the size of the ice sheet and ice history, the presence of tectonic stress, its magnitude, the overburden parameter ζ, material properties, mantle rheology and crustal weak zones.

5.1 STRESS AMPLIFICATION AND SIZE OF ICE SHEETS

According to Johnston (1987, 1989), fault stability is induced during glacial loading. This is confirmed by Wu & Hasegawa (1996) for the Laurentide ice sheet. The reason, as explained in Section 4.4, is that the effect of increasing the mean stress during loading is larger than the effect of the increase in the radius of the Mohr circle, and as a result the Mohr circle moves away from failure. However, Johnston et al. (1998) showed that the magnitude of the horizontal fiber stress induced by glacial loading depends on the size of the load relative to lithospheric thickness, and that there is stress amplification for smaller ice sheets. Peak amplification occurs if the horizontal dimension of the ice sheet is about four times the lithospheric thickness, so that the fiber (deviatoric) stress can be about four times the weight of the ice sheet.

To study the effects of stress amplification on the ice sheets in the British Isles, Fennoscandia and Laurentia, Johnston et al. (1998) loaded a layered incompressible visco-elastic Earth with an 80 km thick lithosphere using a simple ice model that has the parabolic shape of an ideal ice sheet, and the ice model also takes into account the migration of the ice margin during glacial retreat. For the ice cap in the British Isles, whose size varies from about 8 to 5 times the thickness of the lithosphere (at glacial maximum to the end of deglaciation), fault instability is promoted under the ice sheet at glacial maximum and throughout the glacial cycle (Fig. 5.1a) - this is opposite to what occurs under a large (e.g., Laurentide) ice sheet, where fault stability is promoted under the ice load (Fig.5.1c). To see why, note that Fig. 4.5a is for a large ice load where there is no horizontal stress amplification, so the increase in horizontal stress ($\Delta\sigma_1 = \sigma'_1 - \sigma_1$) is of similar magnitude to the increase in the vertical stress ($\Delta\sigma_3 = \sigma'_3 - \sigma_3$). But for the British ice cap, the increase in horizontal stress ($\Delta\sigma_1$) is several times larger than the increase in the vertical stress ($\Delta\sigma_3$), then the radius of the Mohr circle would be much larger than the increase in mean stress, so the Mohr circle would intersect the line of failure.

For the ice sheet comparable to that in Fennoscandia, its size varies from about 12 to 6 times the thickness of the lithosphere; thus, fault stability was promoted under the ice load until about 12 ka BP when the size of the ice sheet shrinks to about 8 times the thickness of the lithosphere. As a consequence, fault instability starts at about 2 ka before the end of deglaciation but become most negative at the end of deglaciation (Fig. 5.1b). These results have been confirmed in Lund (2005).

It should be noted that ambient tectonic and overburden stresses are not included in Fig.5.1. Lund (2005) showed that the presence of overburden and deviatoric (ambient) stress can strongly affect fault stability outside the ice margin. For example, outside the margin of the Fennoscandian-type ice sheet, fault instabilities are suppressed during glaciation and instability only sets in after the end of deglaciation and at some distance beyond the ice margin. This agrees with the finding of Wu (1998) where both overburden and tectonic stress due to the spreading at mid-Atlantic ridge are included in a realistic ice model for Fennoscandia. Note that both Lund (2005) and Wu (1998) used a uniform mantle viscosity of $1x10^{21}$ Pa·s in these studies, but fault stability outside the ice margin is affected by mantle viscosity in addition to overburden and tectonic stress.

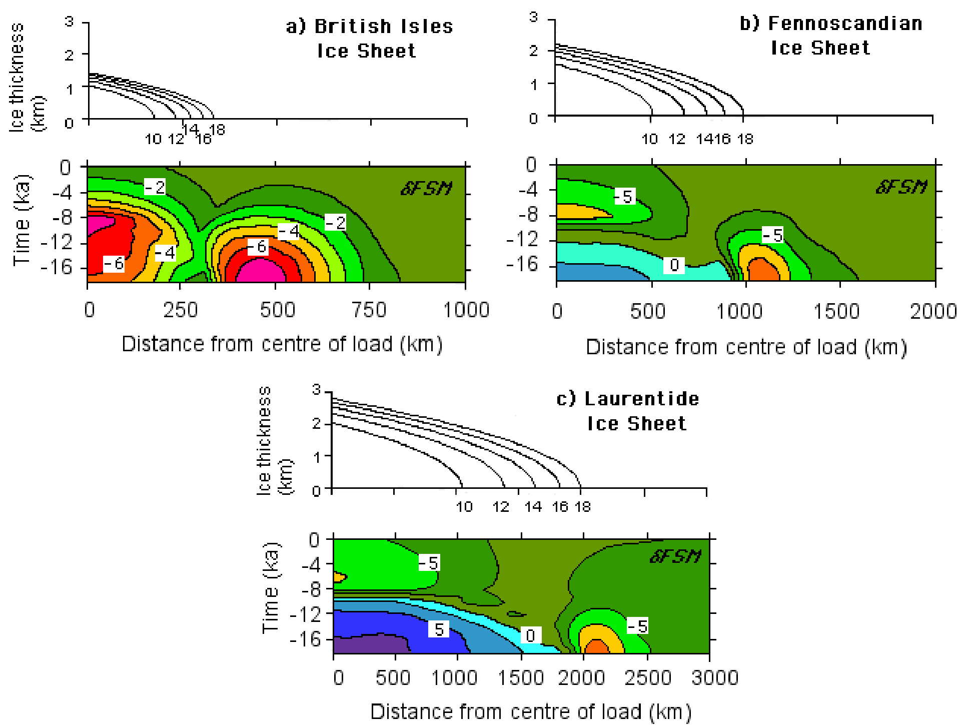

Figure 5.1: Changes in Ice Thickness and Fault Stability Margin (δFSM) as a function of time and radius from the center of an axisymmetric parabolic ice sheet. No tectonic stress was included (after Johnston et al. 1998).

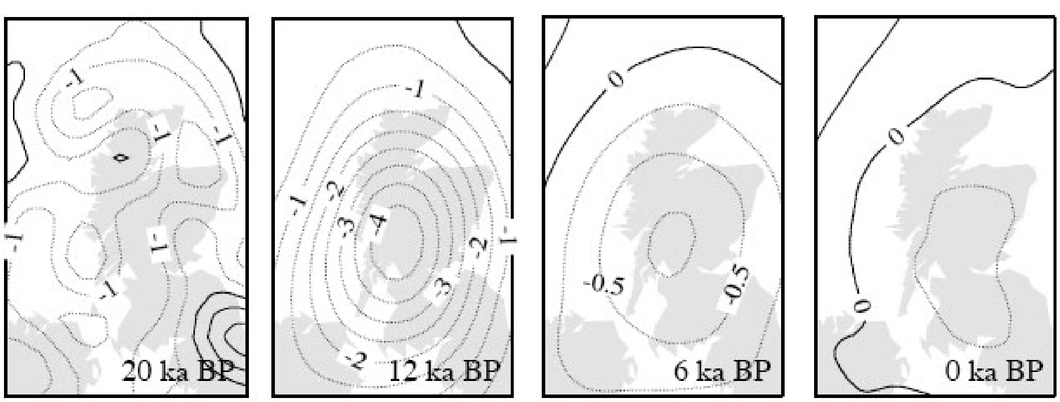

Figure 5.2: Spatial variation of δFSM in Scotland at 4 time periods. Note that fault instability is predicted at glacial maximum and becomes most unstable at the end of the Late Devensian deglaciation (~12 ka BP), after that instability decreases until the present. Tectonic stress due to spreading of mid-Atlantic ridge has been included. Earth model has 65 km thick elastic lithosphere over $4x10^{20}$ Pa-s upper mantle 10^{22} Pa-s lower mantle.

5.2 δFSM FOR REALISTIC ICE SHEETS WITH TECTONIC STRESS

The effects of stress amplification predicted for realistic ice sheets are actually less than that predicted in Fig. 5.1. Johnston et al. (1998) showed that because the British Isles lie around the peripheral bulge of the Fennoscandian ice sheet, the interaction between the compressive stress from the British Isles and the extensional stress of the Fennoscandian ice sheet reduces the ratio of horizontal to vertical stress; thus, fault instability is predicted to decrease underneath the British Isles during glaciation (Firth & Stewart 2000). This is illustrated in Fig. 5.2 where ambient tectonic stresses for a thrust regime (with $S_{H\,max}^{tect}$ = 150 MPa along N60°W direction and $S_{h\,min}^{tect}$ = 145 MPa perpendicular to it) have been included.

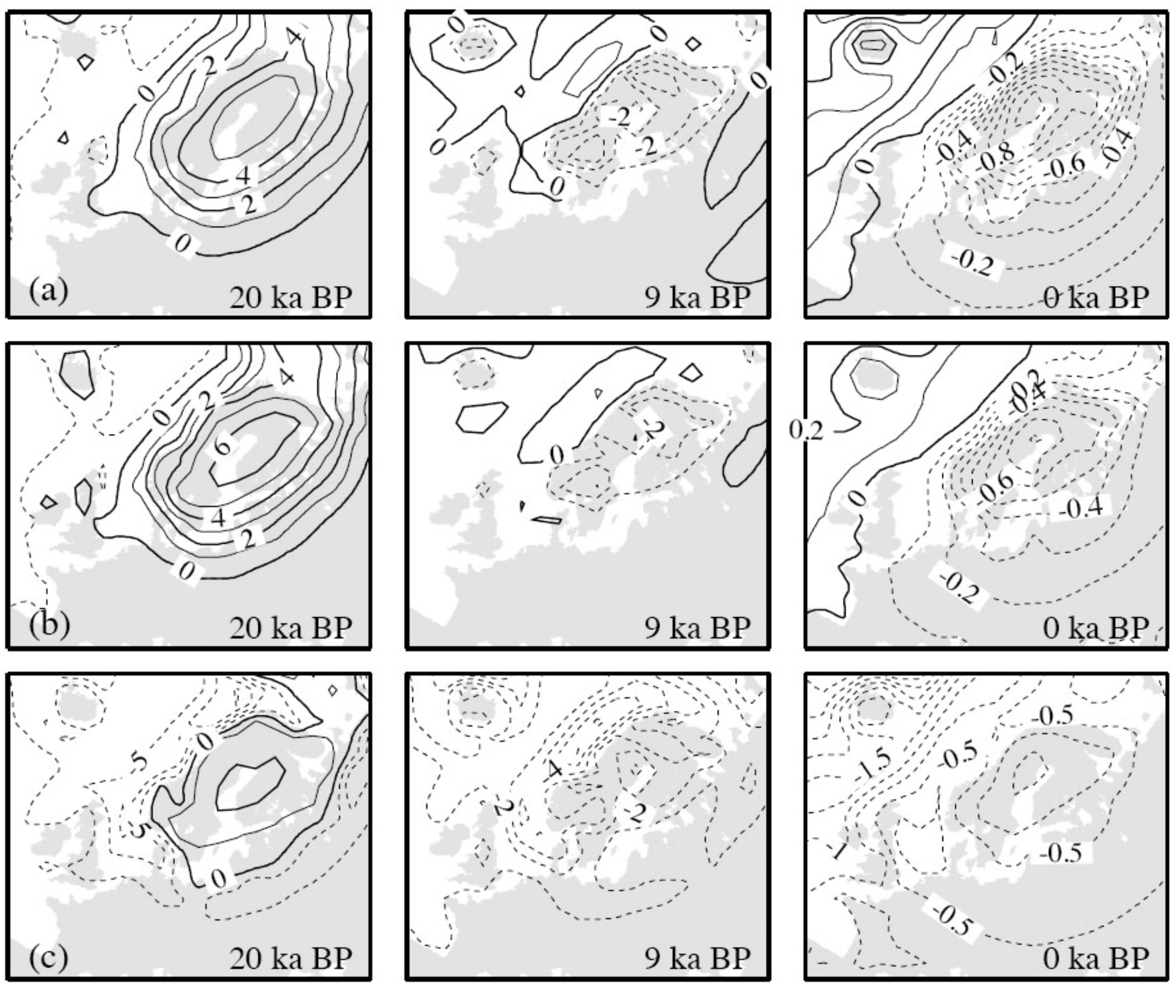

Figure 5.3: Predicted Spatio-temporal variation of δFSM in Fennoscandia at 3 time periods. Contour labels are in MPa. Contours in dashed lines have negative values. The spherical Earth model has 75 km thick elastic lithosphere, 0.36x10^{21} Pa-s upper mantle and 8x10^{21} Pa-s lower mantle. In the top row (a), the model includes compressibility and tectonic stress. The difference between row (b) and (a) is that an incompressible Earth is considered in (b). Similarly, row (c) differs from row (a) in that tectonic stress is neglected in (c) (see Wu et al. 1999 for details).

The effect of tectonic stress on δFSM in Fennoscandia can be seen by comparing row (a) to row (c) in Fig. 5.3. In general, fault instability decreases due to the presence of the tectonic stress. During the last glacial maximum (LGM), the region of fault stability extends farther beyond the ice margin than it does without tectonic stress. By 9 ka BP, fault stability is found just outside the LGM ice margin, except in the northeast and south where fault instability decreases in value outside the ice margin (Fig.5.3 row a). At the present time, fault stability is predicted in the northwest offshore, while fault instability is predicted within Fennoscandia and, outside the LGM ice margin in the south. The presence of tectonic stress has a smaller effect on fault instability within the LGM ice margin because δFSM there is dominated by the "rebound stress" and as shown in the axisymmetric model, the onset time is about 2 ka earlier than the end of deglaciation, when δFSM becomes most negative. This can be seen in Fig. 5.4 where the evolution of δFSM is shown for four sites within the ice margin at LGM – although to date no evidence of glacially - induced faulting has been found in neither Oslo nor Örebro. The onset time of instability lies within the uncertainties of the observed onset time and the mode of failure (around Gällivare & Kramfors in Angermanland) is of the thrust type as indicated by the postglacial faults.

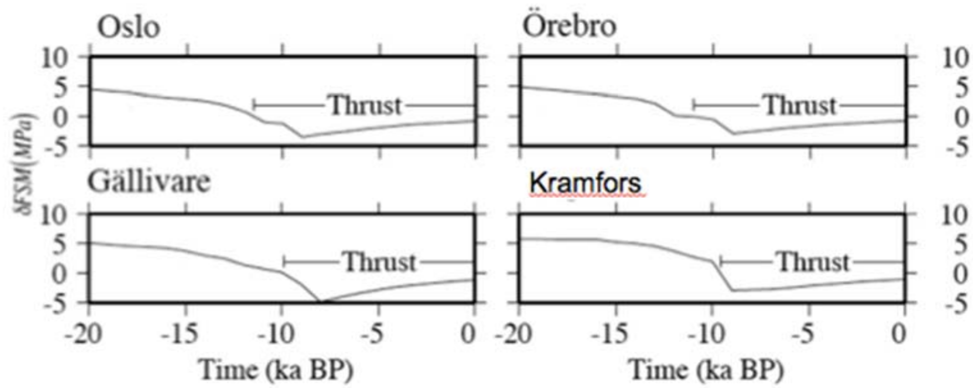

Figure 5.4: Evolution of δFSM for 4 sites in Fennoscandia predicted by the compressible Earth model in Fig.5.3a, where tectonic stress has been included. Fault instability is predicted earlier than the end of deglaciation, which ends earlier in the south (Oslo & Örebro) than in the north (Kramfors & Gällivare). The mode of faulting predicted is thrust (after Wu et al. 1999).

The situation in Laurentide is shown in Fig. 5.5. As predicted by the axisymmetric model, fault stability is promoted under the ice sheet and instability is promoted after local deglaciation. Around LGM, fault stability is also promoted outside the ice margin. However, at the present time, fault instability is promoted outside the LGM ice margin. Fig. 5.6 shows the evolution of δFSM for three sites – Charlevoix lies within the ice margin at LGM, while Indiana and New Madrid are at increasing distance outside the ice margin at LGM. The predicted onset time of instability in Charlevoix lies within the uncertainties of the observed onset time (Shilts et al. 1992). The predicted mode of failure is again of the thrust type and agrees with the finding of the postglacial faults. South of the LGM ice margin in Indiana, instability started early but decreased around 9 ka BP and then increased again after 7 kaBP (see Fig. 5.6). This second pulse of instability may be recorded by the Wabash Valley paleo-earthquake (Obermeier et al. 1991). Further south in New Madrid, instability is predicted to occur in the last 200 years (Fig. 5.6) and is close to that for the New Madrid earthquake in 1811 AD. The predicted thrust mode of failure agrees with that found in Reelfoot Scarp (Johnston & Schweig 1996). However, strike-slip motion is also observed elsewhere (e.g., Bootheel lineament). The value of δFSM there is small and only of the order of -0.01 MPa. Thus, rebound stresses alone may not be enough to trigger the M8 earthquake in New Madrid, implying an unspecified tectonic component.

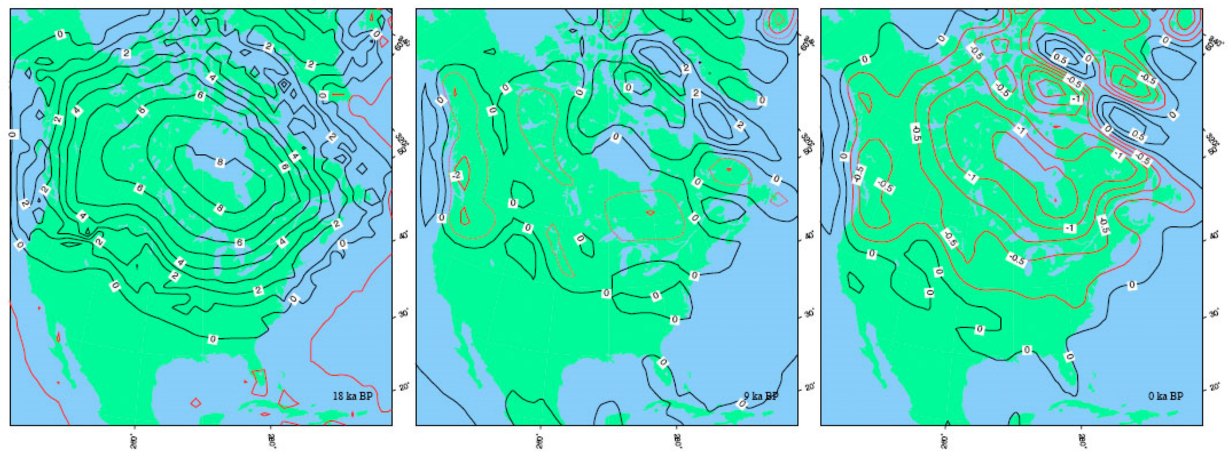

Figure 5.5: Spatio-temporal variation of δFSM in Laurentia at 18, 9 and 0 kaBP. Contour labels are in MPa. Contours in red have negative values. The spherical Earth model has 100 km thick elastic lithosphere, 0.6x10^{21} Pa-s upper mantle and 1.6x10^{21} Pa-s shallow lower mantle above 1200 km depth and 1.6x10^{21} Pa-s in the deep lower mantle. Compressibility have been included. Compressive tectonic stress, with $S_{H\,max}^{tect}$ = 150 MPa along N60°W direction and $S_{h\,min}^{tect}$ = 145 MPa (see Wu & Johnston 2000 for details).

To summarize, the predicted onset timing within the ice margin in Fennoscandia and Eastern Canada lies within the uncertainty of the observations. Also, thrust faulting is predicted under places that were once covered by ice sheets and this mode of failure is supported by the postglacial faults found. However, earthquakes today in Baffin Island (Bent 2002) and parts of eastern US (Zoback 1992b) and Fennoscandia (Arvidsson & Kulhanek 1994, Lindholm et al. 2000), indicate that the mode of failure is not limited to thrusting. A possible explanation is that rebound stress has decayed so that local tectonic stresses have become more dominant.

Next, we look at the spatial distribution of present day earthquakes in Eastern Canada and Fennoscandia. Although deglaciation affects these regions, Fig. 1.1a shows that earthquakes in Eastern Canada today lie along tectonically pre-weakened zones only. The reason, as pointed out by Wu & Hasegawa (1996), is that present-day rebound stress is not large enough to cause failure in intact rocks, but can reactivate pre-existing faults that are initially close to failure. In Fennoscandia, present-day earthquakes offshore Norway are mainly caused by tectonics. The lack of seismicity inland in Fennoscandia but the concentration of earthquakes along the coast today, can be explained if the initial value of FSM in Fennoscandia is close to zero around the coast and about 2 MPa in the interior or that the high angle faults there require 2 MPa to reactivate. Alternately, the stress released along the interior faults early in the deglaciation stage may have resulted in a reduction of seismicity in the interior today (Wu et al. 1999).

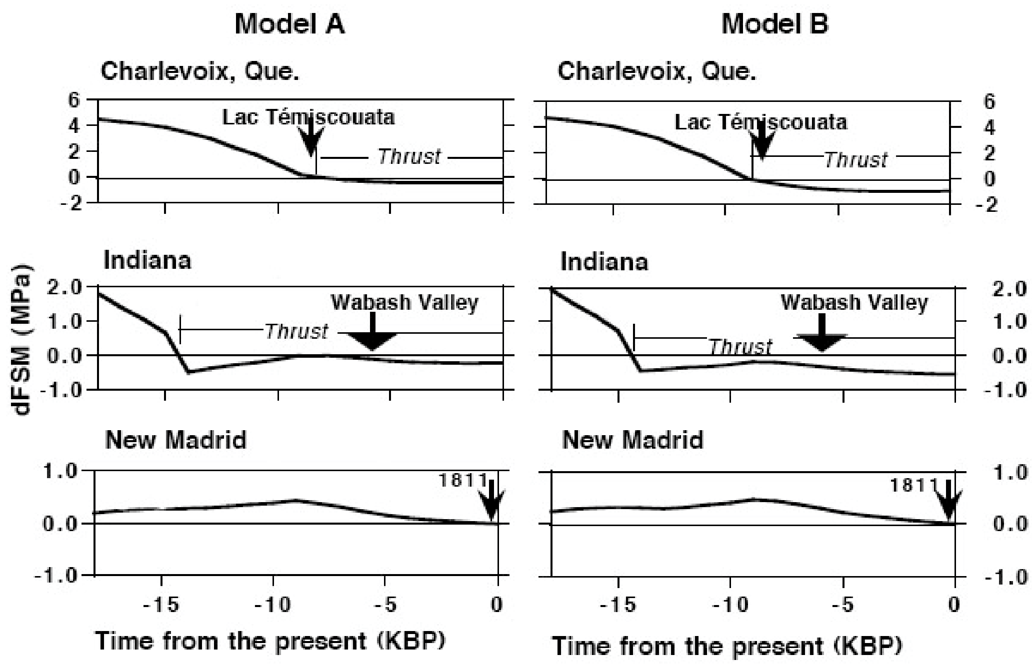

Figure 5.6: Evolution of δFSM for 3 sites in North America predicted by two spherical compressible Earth models with tectonic stress included. Model A is the same as that in Fig.5.5, while Model B is similar to Model A except that the viscosity in the deep lower mantle is 3x10^{22} Pa-s. Thrust faulting is predicted at these places. The observed timing of nearby paleo-earthquakes is indicated by the arrow.(see Wu & Johnston 2000 for details).

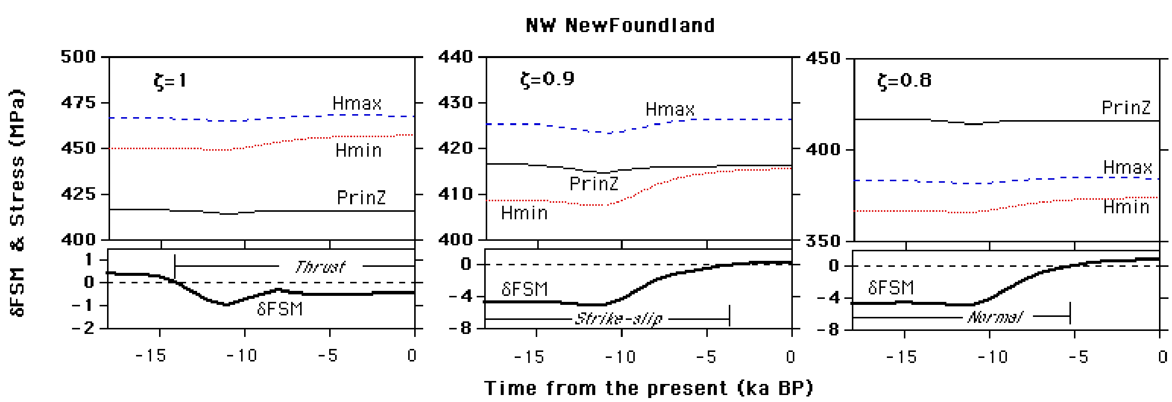

Figure 5.7: Effect of overburden parameter ζ on the time evolution of the horizontal principal stresses (Hmax, Hmin), the vertical principal stress (PrinZ), δFSM and the mode of failure at NW Newfoundland at a seismogenic depth of 12.5 km. The maximum tectonic principal stress is oriented N60°E with a magnitude of 50 MPa, while that of the orthogonal component is 40 MPa (after Wu & Hasegawa 1996b).

5.3 EFFECT OF OVERBURDEN PARAMETER (ζ) AND TECTONIC STRESS MAGNITUDE

The results in the last subsection are computed near the surface of the Earth. In section 3.1.5, it was shown that as depth increases, the increase in the magnitude of the horizontal principal stresses relative to the vertical stress depends on the overburden parameter ζ (see equations 3.6 , 3.7a & b), and the ambient fault regime will change as a function of depth. Fig. 5.7 illustrates the effects of ζ on the evolution of the principal stresses and δFSM for Eastern Canada. For $\zeta \geq 1$, the vertical principal stress is always the minimum principal stress (see Fig.5.7a) and thrust faulting is predicted to occur at the end of deglaciation around 14 ka BP in NW Newfoundland. When the value of ζ decreases to around 0.9, the vertical principal stress becomes the intermediate principal stress, so the mode of failure is strike-slip whenever failure occurs (Fig. 5.7b). However, fault instability occurs before about 4 ka BP in NW Newfoundland. Further decreasing in the value of ζ to around 0.8 or lower makes the vertical principal stress the maximum principal stress, but normal faulting is predicted to occur only before about 5 ka BP in NW Newfoundland (Fig. 5.7c). Wu & Hasegawa (1996b) showed that if the value of ζ is less than 1, then the onset timing of faulting near Charlevoix or near Indiana cannot be explained. Moreover, fault stability is predicted everywhere in eastern Canada today. Since these results are contrary to observations, only $\zeta \approx 1$ will be considered below.

The effect of tectonic stress magnitude on δFSM has also been studied by Wu & Hasegawa (1996b). They found that the magnitude of the tectonic stress within a given stress regime has little effect on the amplitude of δFSM or the onset timing of failure, except when the tectonic stress magnitudes are both small (< 20 MPa), which is highly unlikely (Hasegawa et al. 1985).

5.4 EFFECTS OF MATERIAL PROPERTIES, COMPRESSIBILITY AND MANTLE RHEOLOGY

Material properties, such as density, Young's modulus, compressibility, thickness of the lithosphere and mantle rheology affect the magnitude of stress and thus fault stability. However, the most important effect on onset timing and the minimum value of δFSM is from the ice model (Wu et al. 1999). In the following, we shall review the effects of material properties, compressibility and rheology on deglaciation-induced seismicity.

Lund (2005, 2006) found that smaller shear stress is obtained if the density or the Young's modulus of the lithosphere decreases, but larger shear stress is obtained if density or Young's modulus increases. However, these two parameters have little effect on the vertical displacement. On the other hand, thickness of the lithosphere has large effects on both the shear stress and vertical displacement: A thin lithosphere produces larger deformation under the load and shear stress become more localized near the ice margin where the shear amplitude also increases in magnitude. A thicker lithosphere spreads deformation farther away from the load, has smaller deformation underneath the load and has a smaller stress magnitude. The effect of lithospheric thickness on the onset of timing and minimum δFSM has been shown to be moderate (Wu et al. 1999) – for a 20 km reduction in lithospheric thickness, the onset time changes by less than 500 yrs and the minimum δFSM changes by less than 1 MPa.

The effect of compressibility can be separated into material compressibility and internal buoyancy. The former means that the elastic bulk modulus in the stress-strain relation is finite and the latter is due to the dilatation of rock (equation 2.4) that causes internal buoyancy (see the last term in equation 2.3). Klemann et al. (2003) and Wong & Wu (2019), showed that instability may arise in a compressible Earth because internal buoyancy counteracts the advection of pre-stress (second term on the right side of equation 2.3), which provides the stabilizing restoring force. Thus, many studies of GIA have assumed incompressibility in their computation. An added advantage for the spectral method is that the solution for an incompressible Earth does not involve transcendental functions (compare equation 30 and 43 in Wu & Peltier 1982) and can be obtained more accurately. For the finite element method, incompressibility or material compressibility can be easily included (Wu 2004), but the inclusion of internal buoyancy is complicated (Wong & Wu 2019).

Lund (2005) found that introducing material compressibility causes a decrease in shear stress and displacement, although the latter effect is small. When internal buoyancy is included, the effect of compressibility is found to give larger vertical displacements and longer relaxation times (Wu & Peltier 1982), and the difference between compressible and incompressible solutions for the vertical displacement can be as large as 10%. On the other hand, Mitrovica et al. (1994) found that the effect of compressibility on horizontal motion can be larger (20%). Thus, it is of interest to investigate the total effect of compressibility (including internal buoyancy) on fault stability. This can be seen by comparing row (a) and row (b) in Fig.5.3, which shows that incompressibility generally causes the amplitude of δFSM in and around Fennoscandia to decrease, but has little effect on the onset time of instability (except in the British Isles and offshore). Incompressibility also has no effect on the mode of failure.

Mantle viscosity controls the rate of relaxation of the rebound stresses and, thus, it is important to study the effect of mantle viscosity and nonlinear rheology on the spatio-temporal distribution of δFSM, onset time of instability and mode of failure. Wu (1997) showed that viscosity structure strongly affects the onset of timing and the magnitude of stress at sites outside the ice margin, but does not significantly affect either the onset of timing or the mode of failure within the LGM ice margin because they are dominated by the ice history (Wu et al. 1999). This is illustrated in Fig. 5.6 for two Earth models that differ in the viscosity of the deep mantle. Wu (1996) also showed that the observed rotation of stress orientation from postglacial time to the present can be used to constrain mantle viscosity.

In the aforementioned papers, the relationship between stress and strain is assumed to be linear, and viscosity is assumed to vary only as a function of depth. However, surface geology and seismic tomography clearly show that material properties of the Earth vary both in the radial and lateral directions. In addition, high-temperature and high-pressure creep experiments show that nonlinear rheology (power-law creep) is likely to occur in the mantle. Recent studies show that the effects of nonlinear rheology (Wu 2002b, Wu & Wang 2008) and lateral heterogeneity (Kaufmann & Wu 2002, Wang et al. 2008) do not significantly affect either the mode of failure or the onset timing within the LGM ice margin. However, this is not true for sites outside the ice margin. The effects of lateral heterogeneity in the mantle and ice history on fault stability in Antarctica have been studied (Kaufmann et al. 2005) and it was found that the inclusion of lateral heterogeneity together with long glaciation phases, can better explain the Balleny Island earthquake, which lies just outside the ice margin in Antarctica.

For understanding long-term geosphere stability, it is also useful to investigate if the rate of change in δFSM is increasing or decreasing in the next few thousand years. This has been computed and shown in Fig. 5.8 for two viscosity models. For the model with uniform mantle viscosity, the fault instability is decreasing in the next thousand years. However, for the model with a high viscosity in the lower mantle, fault instability is increasing with time with an average rate of around -0.06 MPa/ka. Such a trend over a few thousand years will become significant when compared to the stress level of 0.1 MPa needed to trigger the Landers earthquake (Gomberg 1996). On the other hand, one must be cautioned that the location and the amplitude of these rates of change in δFSM depend on the ice history and the mantle rheology. An extensive understanding of ice history and mantle rheology (including nonlinear rheology and lateral heterogeneity) is important for this type of investigation.

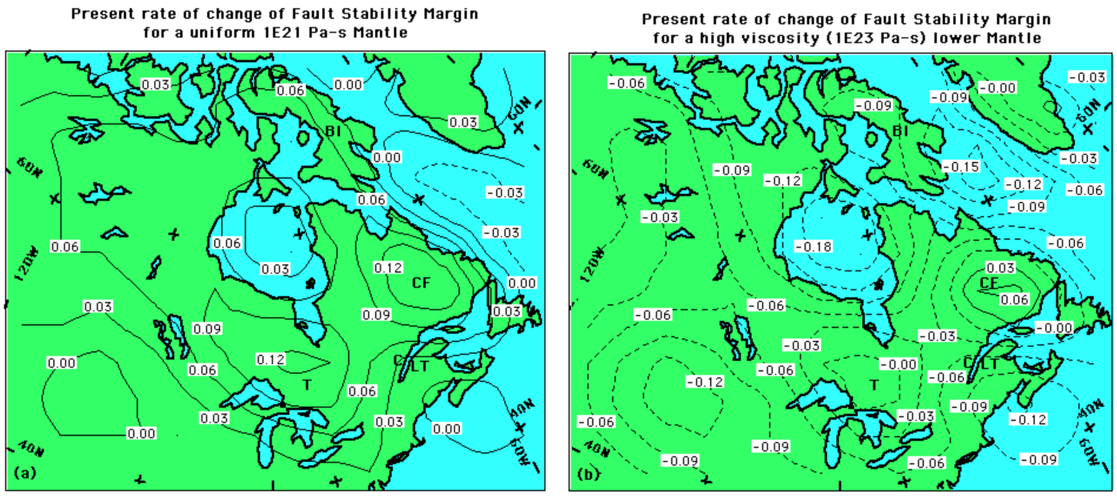

Figure 5.8: Spatial variation of the current rate of change of δFSM in Eastern Canada and peripheral area. Contours are in MPa/ka. Solid contour lines indicate decreasing fault instability (more stable faults) and dashed contours indicate increasing fault instability. Prediction on the left is for a uniform 10^{21} Pa-s mantle. For the diagram on the right, the upper mantle viscosity is 10^{21} Pa-s but the viscosity in the lower mantle is 10^{23} Pa-s. Symbols BI=Baffin Island, CF=Churchill Falls, C=Charlevoix, LT=Lac Temiscouata, T=Timmins (see Wu 1998 for details).

In summary, ice history has the largest effect on the onset timing and the minimum value of δFSM. Mantle rheology, lithospheric thickness and compressibility affect the amplitude of δFSM and the onset timing outside the LGM ice margin, but have little effect on the mode of failure and onset timing within the ice margin. However, mantle rheology is important in the rate of change in δFSM within the ice margin.

5.5 LITHOSPHERIC DUCTILE ZONE – WITH AND WITHOUT LATERAL HETEROGENEITY

So far, the entire lithosphere has been assumed to be purely elastic. In reality, depending on the thermal state and the creep law in a layered lithosphere, the lower crust and certain parts of the lithospheric mantle may experience ductile flow (Fig.1.5, also see section 5.2.1 in Stüwe 2007 or section 12.1 in Ranalli 1995). Because ductile behavior in the lower crust has been found to affect postseismic strains (e.g., Rydelek and Pollitz 1994), Wu (1997) investigated the effect of a laterally homogeneous 25 km thick lithospheric-ductile layer, with viscosity of 10^{22} Pa·s, on δFSM in Eastern Canada and found that the effect is small. However, the effect becomes significant if the viscosity of the ductile layer is greatly reduced. Klemann and Wolf (1999) found that a 10 km thick laterally homogeneous ductile layer with viscosity of 10^{17} Pa·s can shift the onset of timing by 1000 years for sites within the LGM Fennoscandian ice margin and can significantly affect the magnitude of the horizontal velocity. Di Donato et al. (2000) and Kendall et al. (2003) found that laterally homogeneous ductile layers with similarly low viscosities can affect the crustal velocities along the U.S. East Coast and Australia. Such low viscosities of the lithospheric ductile zone are only found in active tectonic settings (e.g., Kaufman and Royden 1994) where the geotherms are high and the presence of water can greatly reduce the viscosity (Dixon et al. 2004). For the cold and dry continental lithosphere under Laurentia, the viscosity of the ductile zone is not likely to be lower than ~ 10^{20} Pa·s (Wu & Mazzotti 2007). Using a layered thermo-mechanical lithospheric model, together with heat-flow data in Northern Europe and creep data for different crustal composition, Schotman (2008) demonstrated this for a wet crust with average grain size and plagioclase feldspar composition. Moderately high heat flow can reduce the viscosity of the ductile zone to 10^{19} Pa·s, but for low heat-flow and dry Baltic Shield, the viscosity of the ductile layer is probably higher than 10^{20} Pa·s. Thus, for the study of lithospheric ductile zones under cold and dry continents, the viscosities between 10^{20} to 10^{21} Pa·s should be considered.

Fig. 5.9a, b & c show the effect of viscosity in the lithospheric ductile layer. Model RF is the reference model where no ductile layer exists within the 125 km thick elastic lithosphere, and the mantle has a uniform mantle viscosity of 10^{21} Pa·s. Models UD1 & UD2 differ from model RF in that they both contain a 20 km thick ductile layer at a depth of 20-40 km. The viscosity of the ductile layer is 10^{21} Pa·s in model UD1, and 10^{20} Pa·s in model UD2. Inspection of Fig. 5.9a, b & c shows that the effect is largest along the LGM ice margin, with a decrease in fault stability along the Labrador coast by about 1 MPa. For model UD1, an area with fault stability is produced in Labrador. The effect on the onset timing for these models are very small well within the uncertainty of dating error (on the timing of fault movement) for sites inside the ice margin, but are much larger outside. Models with lateral changes in lithospheric ductile zone properties were investigated in Wu & Mazzotti (2007), but the results are almost the same as that in UD1 or UD2 (depending on the values of viscosity in the ductile layer).

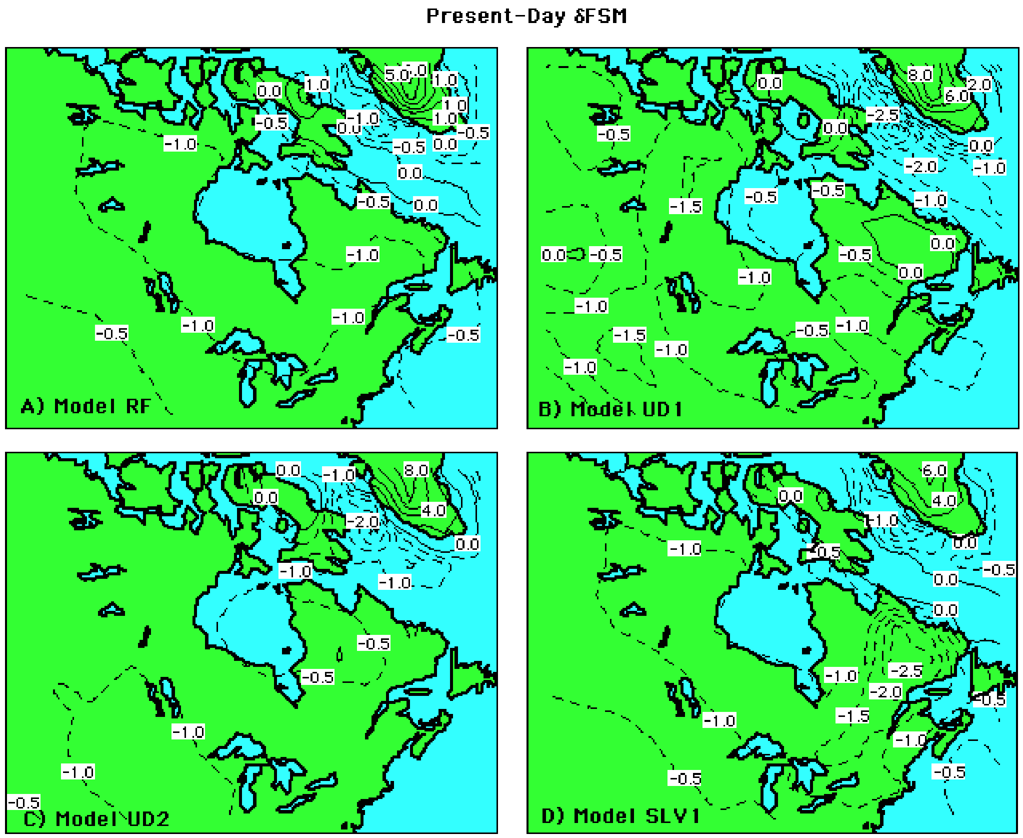

Figure 5.9: Spatial variation of δFSM in eastern Canada and northeastern USA at present time predicted by models RF, UD1, UD2 and SLV1. Contour interval is 0.5 MPa. Dashed contours are for negative values (after Wu & Mazzotti 2007).

In the results presented the ductile zone is assumed to be horizontal. But tectonically weakened areas (e.g., due to plate-plate collision) can form long and narrow zones as viewed on a map, and within the zone, the whole lithosphere might be weakened vertically all the way down to its bottom. Thus, Wu & Mazzotti (2007) also considered models SLV1 and SLV2 where the St. Lawrence Valley weak zone in North America is a vertical ductile zone that extends from the lower-crust to the bottom of the lithosphere. The width of the zone varies from 100 to 300 km. The viscosity of the ductile vertical zone is 10^{21} Pa·s in model SLV1, and 10^{20} Pa·s in model SLV2. δFSM predicted today for SLV1 is contoured in Fig. 5.9d, which shows that the effect is to amplify and localize the value of δFSM along the vertical ductile zone with variation as large as 1.5 MPa. The result of SLV2 is similar, except the amplitudes are slightly larger and thus not shown. Again, the effects on the onset timing for these models are very small (compared with the uncertainty of the dated timing) for sites inside the ice margin, but are much larger outside.

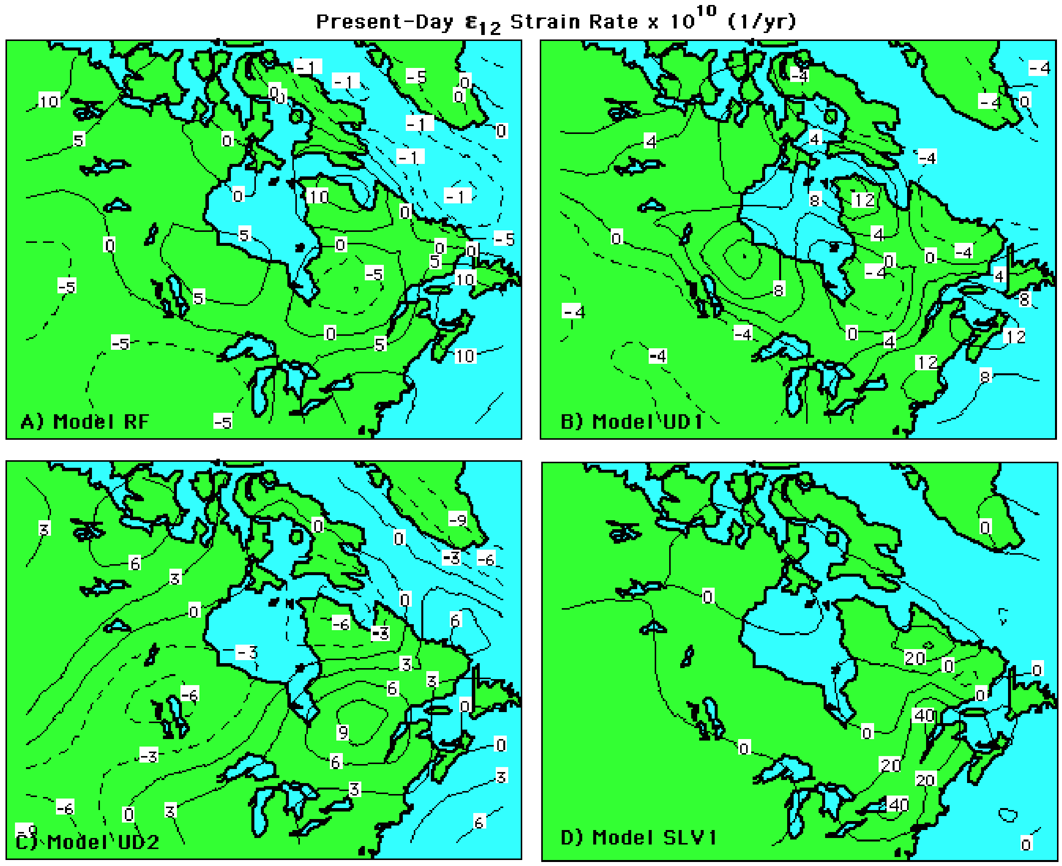

Figure 5.10: Contour plots of present-day horizontal shear strain rate $\dot{\varepsilon}_{12}$ multiplied by 10^{10} for models RF, UD1, UD2 and SLV1. Dashed contours are for negative values.

Wu & Mazzotti (2007) found that the presence of lithospheric weak zones, whether as a horizontal layer or as a vertical zone along the St. Lawrence Valley, have large predicted effects on the strain rates, and that their deviations from the reference model are large enough to be resolved by high-resolution GPS measurements. An example is shown in Fig. 5.10 for the horizontal shear strain rate. The effect of a uniformly thick ductile layer is most significant along the LGM ice margin – especially along the coastal area from Baffin Island to Labrador. Comparison between Fig. 5.10b & c shows that a reduction in viscosity of the horizontal ductile zone causes a reduction in the strain rate. Again, a vertical ductile zone along the St. Lawrence Valley concentrates the strain rate near the weak zone with a very large increase in the peak strain rate magnitude, promoting stability elsewhere in the cratonic interior. The strain rate in model SLV2 is slightly less than that in SLV1 due to the reduction in the viscosity of the ductile zone. These magnitudes are larger than those predicted by James & Bent (1994).

5.6 SUMMARY

The model of glacial induced stress and δFSM evolution with compressive background stress and $\zeta \approx 1$ is able to explain many of the observed data in Laurentia and Fennoscandia. These include the onset of timing and mode of failure of paleo-earthquakes. The present-day distribution and mode of failure of current day earthquakes can also be explained, provided that local tectonic stress and local value of FSM are assumed. The horizontal size of the ice sheet and the ice sheet history has large effects on the onset of timing and the amplitude of δFSM. Mantle viscosity also has large effects on the onset time of earthquakes and the amplitude of δFSM outside the ice margin at LGM, but has little effect on the onset of timing and mode of failure within the ice margin. However, mantle viscosity has a large effect on the rate of change in δFSM within the ice margin for the next few thousand years and is useful for understanding the evolution of the geosphere. The effect of lithospheric thickness is moderate, but the presence of a ductile zone in the lithosphere has large impacts inside the ice margin and should be implemented in future models to more realistically constrain stress and strain concentrations.

6. SLIP EVOLUTION OF A FAULT PLANE DURING A GLACIAL CYCLE

The previous sections assume that the faults are "virtual faults" (see section 4.4). This means that fault planes are not included in the model and no slip evolution of faults are computed.

6.1 SLIP MODEL DRIVEN BY CONSTANT SHORTENING HORIZONTAL VELOCITY AT LATERAL BOUNDARIES

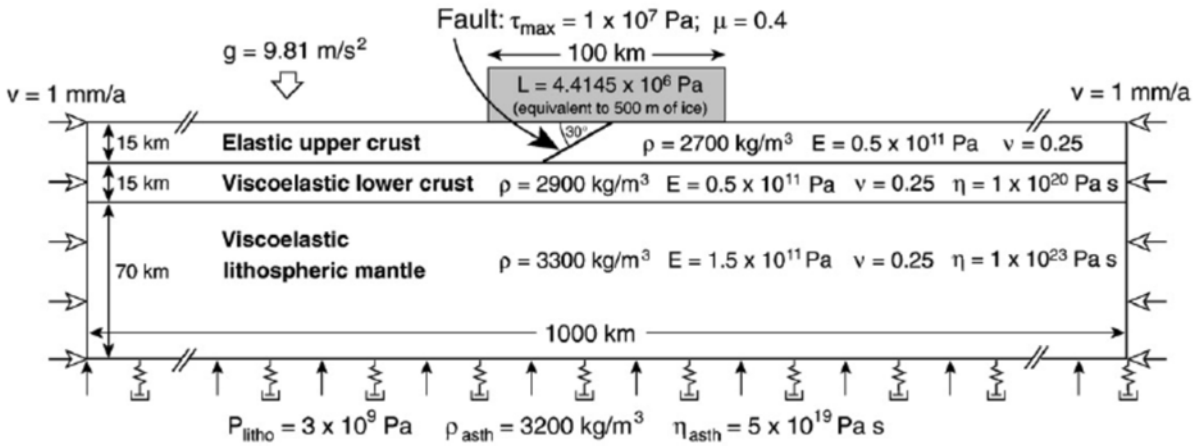

Figure 6.1: The 2-D finite element model of Turpeinen et al. (2008) that is used to study the slip evolution of a single fault plane during the loading and unloading of an ice load of constant thickness.

Recently, 2-D finite-element models have been developed by Hampel's group to study the slip evolution of a single fault plane embedded in a layered lithosphere (Hetzel & Hampel 2005, Hampel & Hetzel 2006, Turpeinen et al. 2008). The lithosphere contains an elastic upper crust, a visco-elastic lower crust, and visco-elastic lithospheric mantle overlying a uniform mantle that is simulated by the elastic foundation and dashpot elements at the bottom of the model. Slip evolution is computed for a fault plane that cuts through the entire elastic upper crust, and a uniform load with simple loading and unloading history is applied over the fault. The orientation of the fault plane can be varied, the dip ranges from 30 ^{o} to 60^o. In the study of Turpeinen et al. (2008), the ambient tectonic stress is assumed to be compressive and this is achieved by applying a constant shortening velocity in the horizontal direction. In the study of Hetzel & Hampel (2005) and Hampel & Hetzel (2006), the ambient tectonic stress is assumed to be tensional and the lithosphere is extended with a constant velocity. In all cases, the fault is allowed to undergo steady-state rate slip before onset of glaciation and deglaciation.

The results of Hampel and Hetzel (2006) confirmed earlier findings: (i) During glacial loading, active thrust and normal faults become more stable and so their slip rate decreases and may even drop to zero (see Fig. 6.2) if the ice thickness is large enough; (ii) during unloading, both the thrust and normal faults become more unstable and so slip motion resumes on the fault. What is found in these simple models is that the resumed slip proceeds at an accelerated rate - more than 10-fold higher than the steady-state rate of about 0.2 mm/yr before glaciation for the thrust fault (Turpeinen et al. 2008) and more than twice the steady-state rate for the normal fault. As expected, the period of accelerated slip coincides with the time of postglacial uplift of the land, but this accelerated rate gradually decreases back to the steady-state slip rate soon after deglaciation ends (see Fig. 6.2).

Turpeinen et al. (2008) also found that the magnitude of the slip acceleration along the thrust fault is controlled by several variables, including the thickness of the ice sheet, the viscosity of the lower crust and the lithospheric mantle, and the long-term rate of shortening. Also, as the dip angle of the thrust fault increases, or the shortening rate decreases, the magnitude of slip decreases, but their effects are less important.

3-D finite-element models have also been used to investigate the slip evolution (Hampel et al. 2007, Maniatis & Hampel 2008), for normal faults. Using such a model, the 2-D results have been confirmed, especially for the example of the Teton fault in the United States (Hampel et al. 2007).

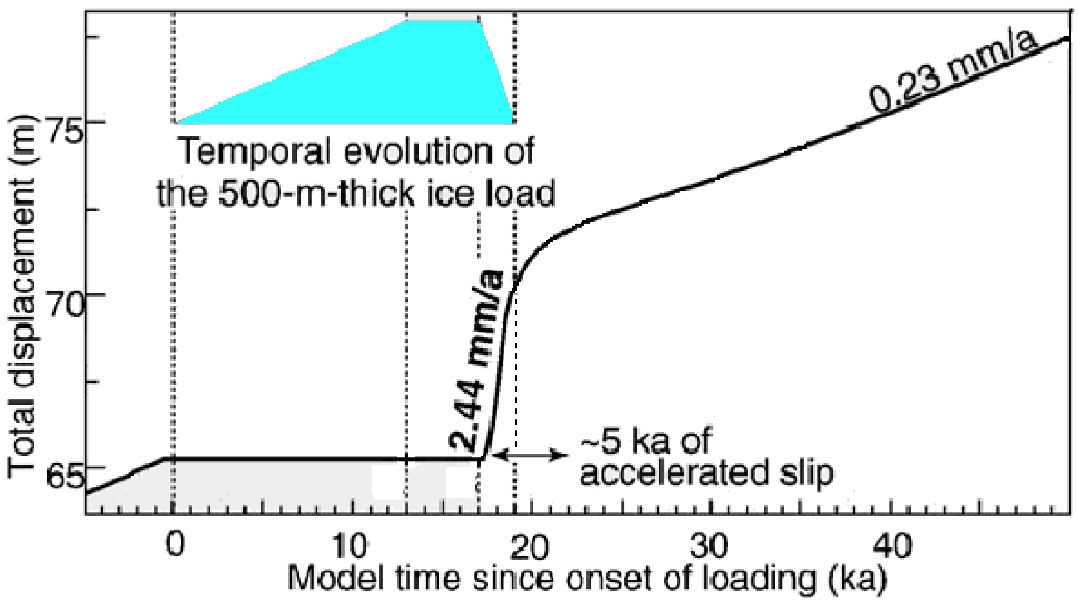

Figure 6.2: Evolution of fault slip predicted by the reference model of Turpeinen et al. (2008) which is shown in Fig. 6.1. Shortening of the model gives a steady-state slip rate of 0.23 mm/a before and long after the application and removal of a 500 m thick ice load whose history is depicted by the light blue polygon. In this model, slip ceases during loading but experience accelerated slip of 2.44 mm/a shortly after the onset of unloading.

However, the applicability of Hampel's model to Scandinavia (and larger ice sheets) has been called into question by Steffen et al. (2015). First, the Earth model of Hampel's group does not include the important effects of stress migration, from the mantle to the lithosphere following the relaxation of the viscoelastic mantle during and after the glacial cycle. Second, the horizontal dimensions of their ice model is much smaller than the ice sheets in Laurentia, Antarctica, Greenland and Fennoscandia. Also, the time scale of glacial loading and unloading are too short to be realistic. Third, shortening velocity boundary conditions (between 1 and 5 mm/yr) are applied at the lateral sides of the Earth model and as a result, continuous slip of the order of 0.2 mm/yr is predicted along the fault even **before** the glacial cycle. Thus the predicted fault slips are caused by the velocity boundary conditions and not entirely by glacial loading or unloading. Finally, their predicted slip rates after glacial unloading are not supported by observations. Also, the large (2.4 mm/yr) slip predicted during deglaciation is over a time scale of a few thousand years and not the observed seismogenic time-scale of a few seconds or minutes.

6.2 THREE-STAGE SLIP MODEL

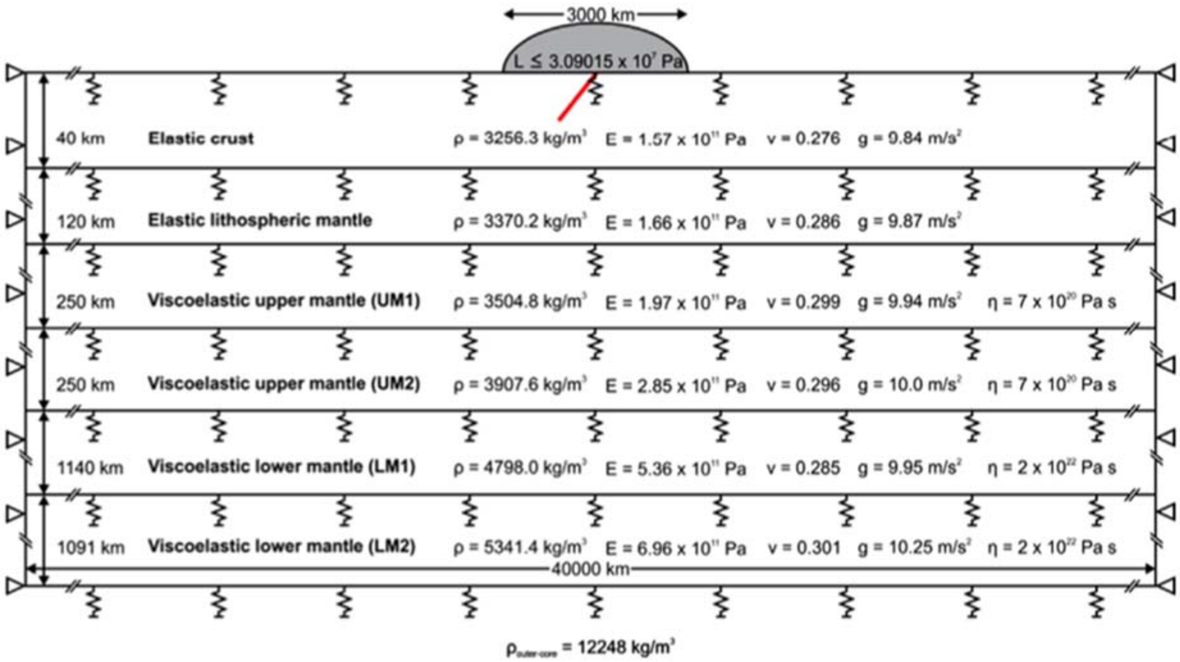

Figure 6.3: Fault slip model of Steffen et al. (2014a). The springs represent foundations that mimic the advection of pre-stress term (see section 2.2.2). The triangles represent the fixed degree of freedom along the sides of the model. The red line indicates the location and orientation of the fault. For the 2D model, the parabolic ice sheet is used. The elastic parameters and gravity values are from the PREM Earth model.

Steffen et al. (2014a) proposed a new finite-element (FE) methodology that takes into account the effects of a physical fault surface (not "virtual fault" as discussed in section 4.4) at arbitrary orientation and the new methodology can compute the fault slip magnitude (which the previous FE model, as described in sections 2 to 4, cannot do).

The new methodology consists of a **three-stage FE model**: In the first stage, the FE model is exactly the same as that described in sections 2 to 4, i.e. the Earth model includes the whole viscoelastic mantle and the lithosphere (see Fig. 6.3). The glacial induced stresses are then computed exactly as in Wu & Hasegawa (1996b) for a realistic ice thickness history model. The background tectonic stresses as well as the overburden pressure are then added to the glacial induced stresses to give the total stress field. In the second stage, the FE model only includes the lithosphere with the fault structure, but the fault surfaces are tied allowing no fault movement. The total stress and displacement fields from the first stage are applied to this model. However, the applied stresses and displacements are not in equilibrium (as additional stresses are added), so this FE model is not stable. To obtain stability, all degrees of freedom are fixed in all directions and reaction forces are determined for each degree of freedom for all the nodes in a static analysis. These reaction forces are then applied together with the stress and displacement fields to the FE model of the third stage. The fault structure in this 3rd FE model that include faults with negative δFSM is then untied and free to move. This results in a static fault movement that lasts only for a few seconds and thus simulates the occurrence of a glacially-triggered earthquake. The new displacements and stresses in this third FE model is now analyzed for fault slip behavior.

The advantage of this methodology is that fault movements are driven entirely by stress changes rather than by velocities at the boundary. In addition, the fault movements take place within the seismogenic time-scale of a few seconds or minutes and thus is consistent with what is observed. The validity of this methodology in predicting the magnitude of slip is shown in Fig. 6.4a. There, the black curve shows the vertical displacement along the Earth's surface predicted by this three-stage FE model immediately after fault slip occurred. The dashed line is from the analytical solution of an elastic halfspace (Okada 1985). They both predict an upward motion of the hanging wall and a downward motion of the footwall in this thrust earthquake. The good agreement between them is clearly seen. The variation of vertical displacement as a function of depth as predicted by this three-stage FE model is also shown in Fig. 6.4b.

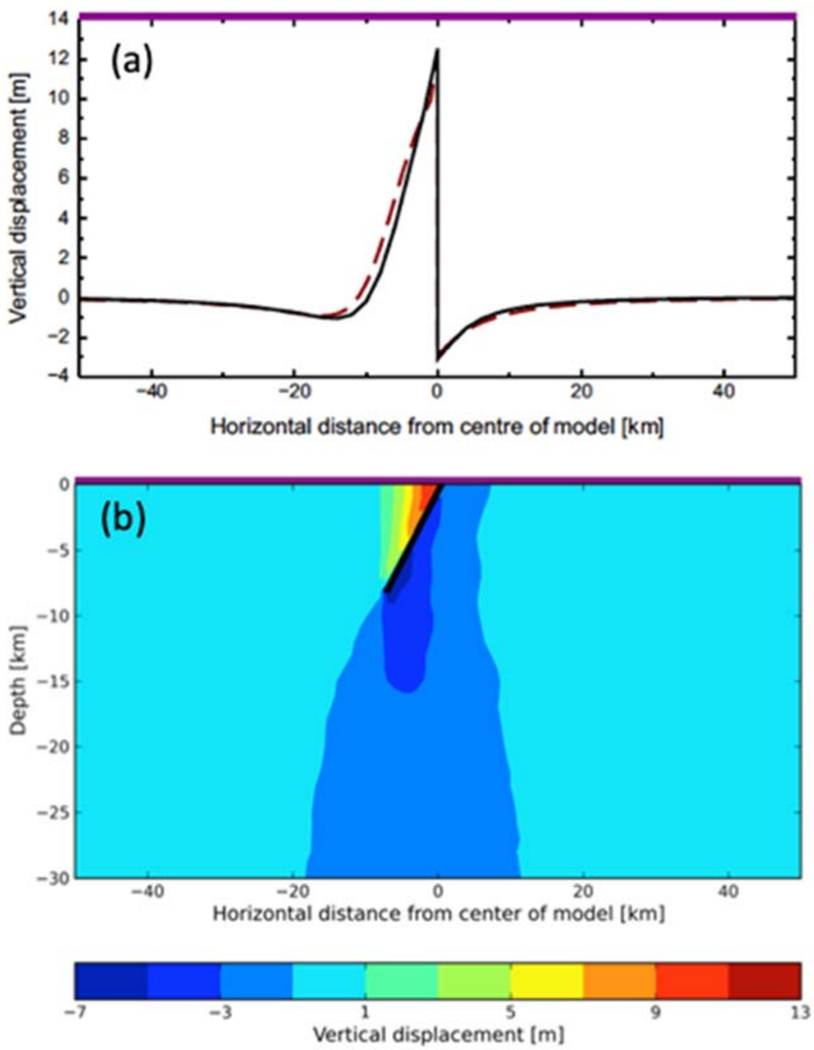

Figure 6.4: (a) Black line shows the predicted Vertical Displacement Variations along the surface of the model of Fig. 6.3, near the end of deglaciation – as computed by Steffen et al. (2014a). The dashed line is the analytical solution obtained by Okada (1985). (b) Vertical displacement as a function of depth computed by Steffen et al. (2014a).

Using a three-stage FE model in 2D and parabolic ice sheet with simple loading history, Steffen et al. (2014b, c) investigated the sensitivity of fault throw and activation time to lithospheric and crustal thickness, viscosity in the upper and lower mantle, ice-sheet thickness and width, as well as fault location, dip angle and fault properties (e.g. the coefficient of friction and depth of the fault tip) in a thrust regime. Their results confirm earlier findings with virtual faults that the presence of ice load suppresses fault movement, but that faults are reactivated near the end of deglaciation. The effect of the lateral length of the ice sheet on the activation time of earthquakes is also confirmed. The predicted throw of the thrust fault lies between 10 to 18 m, which is consistent with the observed maximum throw along the Pärvie fault in Northern Sweden. Their study found that the magnitude of fault slip is mainly affected by fault properties and the thickness of the crust and lithosphere, and not by the lateral size of the ice sheet. Ice thickness can also affect the magnitude of slip, but the effect is typically less than 5 meters. Now, the magnitude of the fault slip is related to earthquake magnitudes, from this the predicted fault slip is estimated to be able to generate paleo-earthquakes with magnitude between 5.9 to 8.5. Another interesting result that is worth mentioning is that thrust faults with low dip angle typically stop after one fault movement, but high angle thrust faults (dip $\geq 60^{o}$) can be activated with several fault movements although the subsequent slips are smaller than that of the first event – which is also supported by observations (Smith et al. 2018).

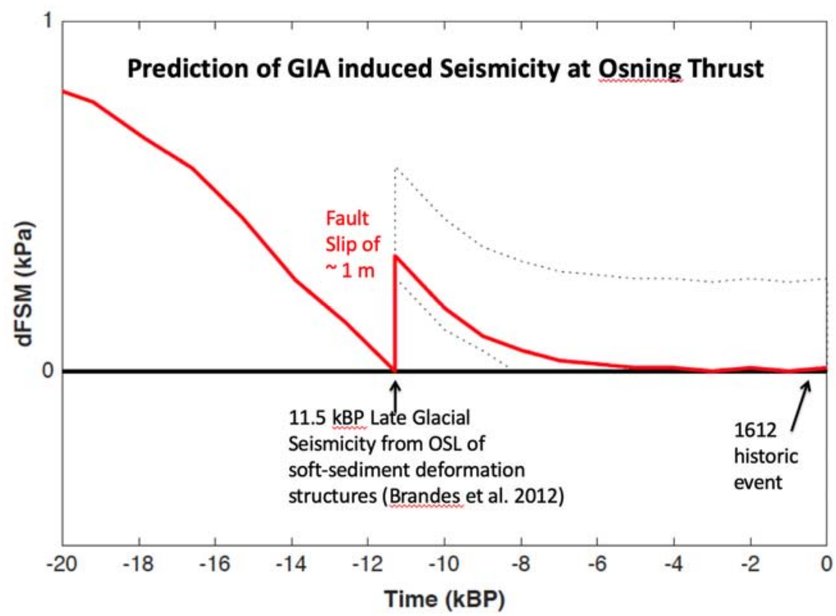

Figure 6.5: Changes in Fault Stability Margin for the thrust fault in Osning, Germany and the effect of fault slip magnitude on the timing of the historic event (adopted from Brandes et al. 2015).

The fault slip magnitude can be used in understanding paleo and historic seismic events and their relation to stress release after fault reactivation. Fig. 6.5 summarizes the seismic history at a site along the Osning Thrust which lies just outside the Fennoscandian ice margin at the Last Glacial Maximum in north central Europe (Brandes et al. 2015, 2018). Here, beside the historical earthquake in 1612, a paleo-earthquake also occurred around 11.5 ka BP with magnitude greater than 5.5, implying a fault slip of around 1 meter. The predicted δFSM history from the GIA model is shown by the red curve. From about 20 to 11.5 ka BP, the value of δFSM is positive meaning that there is fault stability. But due to the retreat of the Fennoscandian ice sheet, it became zero around 11.5 ka BP – in agreement with the observed time of the paleo-earthquake. When the fault slipped around 11.5 ka BP, part of the stress around the fault get released. If the fault slipped with magnitude around 1 m at 11.5 ka BP, then the stress release brought the fault back to stability as shown by the red curve. However, subsequent decay of δFSM brought it back to instability around the time of the historic earthquake in 1612. The dotted lines indicate how the magnitude of the fault slip affects the timing of the second historic seismic event. If the slip magnitude is much smaller than 1 m, then the second event is predicted to occur much earlier, e.g. around 8 ka BP instead of 1612. On the other hand, if the fault slip is much greater than 1 m, then the second event would not have occurred during historic time. So, the observed magnitude of the fault slip and the timing of the paleo-earthquake constrains the timing of the historic earthquake, and all three observations (the timing of the paleo and historic events and the magnitude of the paleo-slip-event) can be explained simultaneously by the glacial induced stress model.

6.3 SUMMARY

In summary, preliminary 2D study of the slip along a single active fault plane induced by a glacial loading cycle, confirms the findings of earlier studies with virtual faults. However, Hampel's model, which is driven by constant horizontal velocity at lateral boundaries, has been called into question because the ice and earth models used and the predicted slip rates are not realistic. The three-stage model of Steffen et al. (2014a) is more realistic - it can predict the observed throw of the Pärvie fault and fault movements are predicted to take place within the seismogenic time-scale of a few seconds or minutes. The magnitude of fault slip is found to be mainly affected by fault properties and the thickness of the crust and lithosphere. For the paleo-earthquake in the Osning Thrust, the magnitude of the associated fault slip and stress release near the end of deglaciation is found to be key in determining the onset time of the subsequent historic earthquake event.

7. DISCUSSION

In this report, we have considered stresses of different geologic origin and found that they can be classified as either time-dependent (within the last 20,000 years) or time-independent ambient stress for the purpose of this study. Away from the areas of anomalous rheology, the time-dependent contribution is mainly from the glacial ice/water loading or unloading events, the upward migration of stress from the mantle and the concentration of stress in the lithosphere. The shear stress induced by glacier flow has also been studied. Its contribution to the total stress field is found to be small and can be neglected in this study. For studies of first-order (continental-scale) stresses in Laurentide and Fennoscandia, the stress due to ridge push at the Mid-Atlantic, the overburden stress and pore-fluid pressure are included in the time-independent ambient stress. For more local studies, the regional and local tectonic stresses should be included. These may change the ambient fault regime and the orientation of the ambient stress field, but should have little effect on the computational methodology of δFSM described here.

Different failure criterions have been reviewed. These include Mohr-Coulomb and its extensions. Due to the dynamic nature of the rebound stress, rocks move in and out of failure and, thus, Anderson and Sibson's extensions of the Mohr-Coulomb criteria are not appropriate for this type of study, except for the background state (before the onset of glacial cycles). A better quantity is the Fault Stability Margin or its equivalent version (Lund & Slunga 1999). The quantity δFSM is not dependent on the value of rock cohesion or any time-independent pressure term. Its value reflects whether fault stability or instability is promoted during the glacial cycle. For pre-existing faults that are initially very close to, but not at failure, the promotion of fault instability means that the fault can be reactivated and seismicity induced. Mogi-von Mises fracture criteria gives different values of fault stability, but has no effect on the timing, location or the mode of failure.

From the discussion in Section 5 & 6, we see that most of the geophysical and geological observations (e.g. the timing of fault reactivation, the mode of failure, the fault slip magnitude and the location of seismicity) may be consistent with the predictions from models of glacial isostatic adjustment, provided that the fault were initially close to failure and the background stress regime is thrust-faulting (with $\zeta \approx 1$). Within the ice margin, the main effect on the onset time of paleo-earthquake is from the ice model itself. On the other hand, the amplitude of δFSM within the ice margin and its rate of change in the next few thousand years are sensitive to the rheology of the mantle and lithosphere. Outside the ice margin, the ice history, ambient tectonic stress, mantle rheology and lithospheric rheology are all important factors that affect fault stability and mode of failure.

In this report, most attention is focused on the thrust regime for the determination of background stress. This is because the first order background stress fields in Laurentide and Fennoscandia are both compressive due to the spreading of the North Atlantic Ridge. Furthermore, the background thrust regime assumption can explain most of the observed onset timing and mode of failure.

Our stress evolution model shows that rebound stress was large and dominant from LGM to near the end of deglaciation. Due to stress relaxation and migration, its magnitude has been decreasing exponentially with time and, today, tectonic stress has become more dominant than rebound stress. However, rebound stress can still trigger fault instabilities. In Fennoscandia, the effect of neotectonics have given rise to both strike-slip and normal faulting in addition to thrusting. In eastern Canada, neotectonic is less dominating and thrusting remains the dominant mode for most events.

Currently, large uncertainties still exist in the models of major ice sheet history in the Pleistocene and the rheology profile of the mantle and lithosphere. These models can be improved with more and more precise observations such as relative sea-level data, crustal velocities, measurements of gravity and the Earth's rotational motion. With improved ice and Earth rheology models, the fault stability of sites inside and outside the ice margin can be better understood.

In this report, our main focus is on glacial induced faulting in Laurentia and Fennoscandia; those in Greenland, Antarctica, other smaller ice sheets and alpine glaciers could also be fully investigated. For the study of glacial induced faulting in a specific geographic area, the effects of local tectonic stresses and pore fluid pressure variations during the glacial cycle should also be included. For our fault slip model, only results from 2D models have been presented, but results of 3D models would be more realistic. Furthermore, the reactivation of a fault system, including faults that intersect with each other, needs to be further studied.

REFERENCES

Adams, J. Postglacial Faulting in Eastern Canada: Nature, Origin and Seismic Hazard Implications. 1989. Tectonophysics, 163, pp 323-331.

Adams, J., 1996. Paleoseismology in Canada: A dozen years of progress, J. Geophys. Res., 101: 6193-6207.

Adams, J. & P.W. Basham, 1989. Seismicity and seismotectonics of Canada's eastern margin and craton. In: Earthquakes at North Atlantic Passive Margins: Neotectonics and Post-glacial Rebound. Editors S. Gregersen and P.W. Basham, Kluwer, pp.355-370.

Adams, J. and J.S. Bell, 1991. Crustal stresses in Canada, in The Geology of North America, Decade Map Vol.1, Neotectonics of North America, eds. Slemmons et al., pp.367-386, Geological Society of America, Boulder, Colo.

Anderson, E.M., 1951. The dynamics of faulting and dyke formation with applications to Britian, 2nd Edition, Oliver & Boyd, Edinburgh.

Argus, D. F. and W.R. Peltier, 2010. Constraining models of postglacial rebound using space geodesy: A detailed assessment of model ICE-5G (VM2) and its relatives, Geophysical Journal International, 181, 697-723, doi:10.1111/j.1365-246X.2010.04562.X.

Árnadóttir, T., B. Lund,W. Jiang, H. Geirsson, H. Björnsson, P. Einarsson and T. Sigurdsson, Glacial rebound and plate spreading: Results from the first countrywide GPS observations in Iceland, Geophys.J.Int., in press.

Arvidsson, R., 1996. Fennoscandian earthquakes: whole crust rupturing related to postglacial rebound, Science, 274, 744-746.

Arvidsson, R. & O. Kulhanek, 1994. Seismodynamics of Sweden deduced from earthquake focal mechanisms. Geophys. J. Int., 116: 377-392.

Bent, A.L., 2002. The 1933 M_s=7.3 Baffin Bay earthquake: strike-slip faulting along the northeastern Canadian passive margin, Geophys. J. Int., 150:724-736. doi: 10.1046/j.1365-246X.2002.01722x.

Biju-Duval, B., J.E. Swezey, 2002. Sedimentary Geology: Sedimentary Basins, Depositional Environments, Petroleum Formation. Translated by J.E. Swezey, Published by Editions TECHNIP, pp.656.

Brace W.F. & D.L. Kohlstedt, 1980. Limits on lithospheric stress imposed by laboratory experiments, J. Geophys. Res., 85, 6248-6252.

Brandes, C., H. Steffen, R. Steffen and P. Wu, 2015. Intraplate seismicity in northern Central Europe is induced by the last glaciation, Geology, 43, 611-614, doi: 10.1130/G36710.1

Brandes, C., Steffen, P.B.E. Sandersen, P. Wu and J. Winsemann 2018. Glacially induced faulting along the NW segment of the Sorgenfrei-Tornquist Zone, northern Denmark: Implications for neotectonics and Lateglacial fault-bound basin formation, Quaternary Science Reviews 189, 149-168, doi: 10.1016/j.quascirev.2018.03.036.

Brown, J.M. and J.R. Ritter. 1969. Phenomenal erosion rates in the Eel River basin, California, may be the highest in North America. Geol. Soc. Am. Abstracts with Programs, Pt 7; pp 21-22.

Bungum, H. O. Olesen, C. Pascal, S. Gibbons, C. Lindholm and O. Vestøl, 2010. To what extent is the present seismicity of Norway driven by post-glacial rebound? Journal of the Geological Society 2010; v. 167; p. 373-384.

Byerlee, J.D., 1978. Friction of rock, Pure Appl.Geophys., 116, 615-626.

Cathles, L.M. III, 1975. The viscosity of the earth's mantle. Princeton University Press, Princeton.

Chang, C. & B. Haimson, 2000. True triaxial strength and deformability of the German Continental Deep Drilling Program (KTB) deep hole amphibolite, J. Geophys. Res. 105: 18999-19013.

Clauss, B.,G. Marquardt, G. and K. Fuchs, K. 1989. Stress orientations in the North Sea and Fennoscandia, a comparison to the central European stress field, in Earthquakes at North-Atlantic Passive Margins: Neotectonics and Postglacial Rebound, edited by S. Gregersen and P.W. Basham, Kluwer, p.277-287.

Di Donato, G., J.X. Mitrovica, R. Sabadini & L.L.A. Vermeersen, 2000. The influence of a ductile crustal zone on glacial isostatic adjustment: Geodetic observables along the U.S. East Coast, Geophys. Res. Lett., 27, 3017-3020.

Dixon, J.E., T.H. Dixon, D.R. Bell, & R. Malservisi, 2004. Lateral variations in upper mantle viscosity: Role of water, Earth Plant. Sci. Lett., 222, 451-467.

Dyke, A.S., T.F. Morris & D.E.C. Green, 1991. Postglacial tectonic and sea level history of the Central Canadian Arctic, Geological Survey of Canada Bulletin 397

Farrell, W.E., 1972. Deformation of the earth by surface loads, Rev. Geophys. Space Phys. 10:761.

Farrell, W.E. and J.A. Clark, 1976. On postglacial sea level, Geophys. J.R. Astr.Soc., 46: 647-667.

Fenton, C. Postglacial Faulting in Eastern Canada. Geological Survey of Canada Open File 2774, 1994. Natural Resources Canada.

Findlay, B.F., G.A.McKay, and B.E. Goodison, 1984. Climatic variability of northwestern Ontario for the next million years, in Workshop on transitional processes: Proceedings, edited by W.F.Heinrich, Atomic Energy of Canada, AECL-7822, Ottawa, 14-39.

Firth, C.R. & I.S. Stewart, 2000. Postglacial tectonics of the Scottish glacio-isostatic uplift centre. Quat. Sci. Rev. 19: 1469-1493.

Flowers, G.E and Clarke, G.K.C., 2002a. A multicomponent coupled model of glacier hydrology. 1. Theory and synthetic examples, J.Geophys.Res., 107, doi: 10.1029/2001JB001122.

Flowers, G.E and Clarke, G.K.C., 2002b. A multicomponent coupled model of glacier hydrology. 2. Application to Trapridge glacier, Yukon, Canada, J.Geophys.Res., 107, doi: 10.1029/2001JB001124

Gangopadhyay, A., 2006. Re-visiting the tectonics of the oceanic intraplate earthquake of March 25, 1998 (M8.1) in the Balleny sea, offshore Antarctica. Earth & Planet. Sci. Lett., 249, 456-466.

Gasperini, P. & S. Sabadini, 1990. Finite element modeling of lateral viscosity heterogeneities and post-glacil rebound. Tectonophysics, 179, 141-149.

Gomberg, J. 1996. Stress/strain changes and triggered seismicity following the Mw 7.3 Landers, California, earthquake, Journal of Geophysical Research, Vol. 101, No. B1, p. 751-764.

Gregersen, S. 1992, Crustal stress regime in Fennoscandia from focal mechanisms. J.Geophys. Res., 97:11821-11827.

Hampel, A. & R. Hetzel, 2006. Response of normal faults to glacial-interglacial fluctuations of ice and water masses on Earth's surface. J. Geophys. Res. 111, B046406. doi: 10.1029/2005JB004124.

Hampel, A., R. Hetzel & A.L. Densmore, 2007. Postglacial slip-rate increase on the Teton normal fault, northern Basin and Range Province, caused by melting of the Yellowstone ice cap and deglaciation of the Teton Range? Geology 35(12), 1107–1110.

Hasegawa, H.S., J. Adams and K.Yamazaki, 1985. Upper crustal stresses and vertical stress migration in eastern Canada. J.Geophys.Res.,90, 3637-3648.

Heidbach, O., 2008. http://dc-app3-14.gfz-potsdam.de/

Henriksen, H., 2008. Late Quaternary regional geodynamics and hydraulic properties of the crystalline rocks of Fennoscandia. J. Geodynamics, 45:49-62.

Hetzel, R. & A. Hampel, 2005. Slip rate variations on normal faults during glacial-interglacial changes in surface loads. Nature 435:81-84.

Huybrechts, P., 1990. The Antarctic Ice Sheet during the last glacial-interglacial cycle: a three-dimensional experiment. Ann. Glaciol. 14: 115-119.

Imbrie, J., J.D. Hays, D.G. Martinsen, A. McIntyre, A.C. Mix, J.J. Morley, N.G. Pisias, W.L. Prell and N.J. Shackleton, 1984. The orbital theory of Pleistocene climate: Support from a revised chronology of the marine $\delta^{18}O$ record, in Milankovitch and Climate, edited by A. Berger et al., pp. 269-306, D. Reidel, Norwell, Mass.

Ivins, E.R., T.S. James & V. Klemann, 2003. Glacial isostatic stress shadowing by the Antarctic ice sheet, J. Geophys. Res., 108, No. B12, 2560, doi:10.1029/ 2002JB002182.

Ivins, E.R. & T.S. James, 2005. Antarctic glacial isostatic adjustment: a new assessment. Antarct. Sci., 17, 541-553.

Ivins, E.R., T.S. James, J. Wahr, E.J.O. Schrama, F.W. Landerer & K.M. Simon, 2013. Antarctic contribution to sea-level rise observed by GRACE with improved GIA correction, J.Geophys.Res., 118, 3126-3141, doi: 10.1002/jgrb.50208

James, T.S. and A.L. Bent, 1994. A comparison of eastern North American seismic strain-rates to glacial rebound strain-rates, Geophys. Res. Lett., 21, 2127-2130.

Johnson, R.B., and DeGraff, J.V. (1988). *Principles of Engineering Geology*. Wiley.

Johnston, A.C., 1987. Suppression of earthquakes by large continental ice sheets, Nature, 330, 467-469.

Johnston, A.C., 1989. The effect of large ice sheets on earthquake genesis, in Earthquakes at North-Atlantic Passive Margins: Neotectonics and Postglacial Rebound, eds. S. Gregersen and P.W. Basham, pp.581-599, Kluwer Academic.

Johnston, A.C. & E.S. Schweig, 1996. The enigma of the New Madrid earthquakes of 1811-1812. Annu. Rev. Earth Planet. Sci., 24: 339-384.

Johnston, P., P. Wu & K. Lambeck, 1998. Dependence of horizontal stress magnitude on load dimension in glacial rebound models, Geophys.J.Int., 132: 41-60.

Joughin, I., S.B. Das, M.A. King, B.E. Smith, I.M. Howat & T. Moon, 2008. Seasonal speedup along the western flank of the Greenland Ice Sheet, Science, 320, 781-783.

Kaufman, P.S., and L.H. Royden, 1994. Lower crustal flow in an extensional setting: Constraints from the Halloran Hill region, eastern Mojave Desert, J. Geophys. Res., 99, 15,723-15,739.

Kaufmann, G. and P. Wu, 2002. Glacial isostatic adjustment on a three-dimensional laterally heterogeneous earth: examples from Fennoscandia and the Barents Sea in Glacial isostatic adjustment and the earth system: sea-level, crustal deformation, gravity and rotation, Edited by J.X. Mitrovica & L.L.A. Vermeersen, AGU Geodynamics Series 29: 293-309.

Kaufmann, G., P. Wu & E.R. Ivins, 2005. Lateral viscosity variations beneath Antarctica and their implications on regional rebound motions and seismotectonics, J. Geodyn. 39 (2): 165-181.

Kendall, R., J.X. Mitrovica & R. Sabadini, 2003. Lithospheric thickness inferred from Australian post-glacial sea-level change: The influence of a ductile crustal zone, Geophys. Res. Lett., 30, No.9, 1461, doi:10.1029/2003GL017022.

King, G.C.P., R.S Stein and J. Lin, 1994. Static stress changes and the triggering of earthquakes, Bulletin of the Seismological Society of America **84** (3), 935-953.

Klemann, V. & D. Wolf, 1999. Implications of a ductile crustal layer for the deformation caused by the Fennoscandian ice sheet, Geophys. J. Int., 139, 216-226.

Klemann, V., P. Wu, D. Wolf, 2003. Compressible viscoelasticity: stability of solutions for homogeneous plane earth models, Geophys. J. Int., 153: 569-585.

Kukkonen, I. T., O. Olesen and M.V.S. Ask, and the PFDP Working Group: Postglacial Faults in Fennoscandia: Targets for scientific drilling, GFF, 132, 71–81, 2010.

Lagerbäck, R. 1979. Neotectonic structures in northern Sweden, Geol. Fören. Stockholm Förh., 100, 263–269.

Lagerbäck, R. 1990. Late Quaternary faulting and paleoseismicity in northern Fennoscandia, with particular reference to the Lansjärv area, northern Sweden, Geol. Fören. Stockholm Förh., 112, 333–354.

Lambeck, K., C. Smither, P. Johnston, 1998. Sea-level change, glacial rebound and mantle viscosity for northern Europe, Geophys. J. Int., 134: 102-144.

Lambeck, K., A. Purcell & S. Zhao, 2017. The North American Late Wisconsin ice sheet and mantle viscosity from glacial rebound analyses, Quat. Sci. Rev., 158: 172-210. doi: 10.1016/j.quascirev.2016.11.033.

Latychev, L., J.X. Mitrovica, J. Tromp, M.E. Tamisiea, D. Komatitsch, C.C. Christara, 2005. Glacial isostatic adjustment on 3-D Earth models: a finite volume formulation, Geophys. J. Int. 161 (2005) 421-444, doi: 10.1111/j.1365-246X.2005.02536.x.

Lindholm, C.D., H. Bungum, E. Hicks & M. Villagran, 2000. Crustal stress and tectonics in Norwegian regions determined from earthquake focal mechanisms. Geological Society London, Special Publications, 167, 429-439, doi: 10.1144/GSL.SP.2000.167.01.17.

Love, A.E.H., 1911. Some problems of Geodynamics, Dover, New York.

Lund, B., 2005. Effects of deglaciation on the crustal stress field and implications for endglacial faulting: a parametric study of simple earth and ice models. TR-05-04, Svensk Kärnbränslehantering AB.

Lund, B., 2006. Stress variations during a glacial cycle at 500 m depth in Forsmark and Oskarshamn: earth model effects. R-06-95 Svensk Kärnbränslehantering AB.

Lund, B., P. Schmidt & C. Hieronymus, 2009. Stress evolution and fault stability during glaciation, (report submitted to SKB)

Lund, B. & R. Slunga, 1999. Stress tensor inversion using detailed microearthquake information and stability constraints: application to Ölfus in southwest Iceland. J. Geophys. Res. 104: 14947-14964.

Lundquist, J., 1986. The Weichselian glaciation and deglaciation in Scandinavia. Quat. Sci. Rev. 5: 269-292.

Lundquist, J. & R. Lagerbäck, 1976. The Pärve Fault: a late-glacial fault in the Precambrian of Swedish Lapland. Geol. Fören. Stockholm Förh., 98: 45-51.

Lundquist, J. and M. Saarnisto, 1995. Summary of project IGCP-253. Quat. Int. 28:9-18.

Malvern, L.E., 1969. Introduction to the mechanics of a continuous medium. Prentice-Hall, Englewood Cliffs, N.J.

Maniatis, G. & A. Hampel, 2008. Along-strike variations of the slip direction on normal faults: Insights from three-dimensional finite-element models. Jour. Struct. Geol. 30, 21-28.

Martinec, Z., 2000. Spectral-finite element approach to three-dimensional viscoelastic relaxation in a spherical earth. Geophys. J. Int., 142, 117-141.

McGarr, A., 1988. On the state of lithospheric stress in the absence of applied tectonic forces, J.Geophys.Res.,93, 13609-13617.

Milne, G.A., J.X. Mitrovica, 1998. Postglacial sea-level change on a rotating Earth, Geophys. J. Int., 133, 1-19.

Mitrovica, J.X., J.L. Davis and I.I. Shapiro, 1994. A spectral formulism for computing three-dimensional deformations due to surface loads 2. Present-day glacial isostatic adjustment, J. Geophys. Res., 99:7075-7101.

Mörner, N.A., P.E. Tröften, R. Sjöberg, D. Grant, S. Dawson, C. Bronge, O. Kvamsdal & A. Siden, 2000. Deglacial paleoseismicity in Sweden: the 9663 BP Iggesund event. Quat. Sci. Rev. 19: 1461-1468.

Muir-Wood, R., 1989. Extraordinary deglaciation reverse faulting in northern FennoScandia, in Earthquakes at North Atlantic Passive Margins: Neotectonics and Post-glacial Rebound, edited S. Gregersen and P.W. Basham, pp.141-173, Kluwer Academic.

Muir-Wood, R., 2000. Deglaciation seismotectonics: a principal influence on intraplate seimogenesis at high latitudes. Quat. Sci. Rev. 19: 1399-1411.

Muller, R.A. & G.J. MacDonald, 1997. Glacial cycles and astronomical forcing, Science, 277, 215-218.

Munier, R. and C. Fenton, 2004. Review of postglacial faulting. Current understanding and directions for future studies, in: Munier, R. and H. Hökmark, Respect distances, rationale and means of computation, Tech. Rep., R-04-17, Swedish Nuclear Fuel and Waste Management Co., Stockholm, Sweden

Näslund, J-O, 2006. Ice sheet dynamics, in Climate and climate related issues for the safety assessment SR_Can, TR-06-23, Swedish Nuclear Fuel and Waste Management Co. (SKB), Stockholm, Sweden.

Obermeier, S.F., N.R. Bleuer, C.A. Munson, P.J. Munson, W.S. Martin, K.M. McWilliams, D.A. Tabaczynski, J.K. Odum, M. Rubin & D.L.Eggert, 1991. Evidence of strong earthquake shaking in the lower Wabash Valley from prehistoric liquefaction features, Science, 251, 1061-1063.

Okada, Y., 1985. Surface deformation due to shear and tensile faults in a half-space. Bulletin of the Seismological Society of America 75, 1135-1154.

Pascal, C. and S.A.P.L Cloetingh. 2009. Gravitational potential stresses and stress field of passive continental margins: insights from the south-Norway shelf. Earth and Planetary Science Letters, 277, 464–473.

Pascal. C, D. Roberts and R.H Gabrielsen, 2010. Tectonic significance of present-day stress relief phenomena in formerly glaciated regions. Journal of the Geological Society, London, Vol. 167, 2010, pp. 363–371.

Paterson, M.S. 1978. Experimental Rock Deformation – The Brittle Field. Springer-Verlag, Berlin.

Peltier, W.R., 1974. The impulse response of a Maxwell earth, Rev. Geophys.Space Phys., 12, 649-669.

Peltier, W.R., 1976. Glacial isostatic adjustment – II. The inverse problem. Geophys. J. R. astr. Soc., 46:669.

Peltier, W.R., 1985. The Lageos constraint on deep mantle viscosity: results from a new normal mode method for the inversion of viscoelastic relaxation spectra. J. geophys. Res., 90: 9411-9421.

Peltier, W.R., 1994. Ice age paleotopography, Science 265: 195-201.

Peltier, W.R., 1998. Postglacial variations in the level of the sea: implications for climate dynamics and solid-earth geophysics, Reviews of Geophysics, 36(4): 603-689.

Peltier, W.R., 2004. Global glacial isostasy and the surface of the ice-age earth: the ICE-5G (VM2) Model and GRACE. Ann. Rev. Earth. Planet. Sci. 32:111-149.

Peltier, W.R., 2006. Boundary conditions data sets for spent fuel repository performance assessment. Ontario Power Generation Report No: 06819-REP-01200-10154-R00.

Peltier, W.R. 2011. Long-Term Climate Change. Nuclear Waste Management Organization Report NWMO DGR-TR-2011-14 R000. Toronto, Canada.

Peltier, W.R., D.F. Argus & R. Drummond, 2015. Space geodesy constrains ice-age terminal deglaciation: the global ICE-6G_C (VM5a) model", J. Geophys. Res. – Solid Earth, 129(1), 450-487, doi: 10.1002/2014JB011176.

Ranalli, G., 1995. Rheology of the Earth. Chapman & Hall, London.

Ranalli, G. & Z.M. Yin, 1990. Critical stress difference and orientation of faults in rocks with strength anisotropies: the two dimensional case. J. Structural Geology, 12: 1067-71.

Richardson, R.M. and L.M. Reding, North American plate dynamics. J.Geophys.Res. 96, 12201-12223, 1991.

Roots, E.F., 1984. Comments on the state of knowledge about climatic and geological processes and extra-terrestrial events, in Workshop on transitional processes: Proceedings, edited by W.F.Heinrich, Atomic Energy of Canada, AECL-7822, Ottawa, 270-295.

Roy, K. & W.R. Peltier,.2015. Glacial isostatic adjustment, relative sea level history and mantle viscosity: Reconciling relative sea level model predictions for the US east coast with geological constraints, Geophys. J. Int., 201, 1156-1181, doi:10.1093/gji/ggv066.

Rydelek, P.A. and F.F. Pollitz, 1994. Fossil strain from the 1811-1812 New Madrid earthquakes, Geophys. Res. Lett., 21, 2303-2306.

Sauber, J.M. and B.F. Molnia, 2004. Glacier ice mass fluctuations and fault instability in tectonically active Southern Alaska, Global and Planetary Change, 42, 279-293.

Schotman, H., 2008. Shallow earth rheology from glacial isostasy and satellite gravity: a sensitivity analysis for GOCE. PhD thesis, Technical University of Delft, Delft.

Shilts, W.W., M.Rappol and A. Blais, 1992. Evidence of late and postglacial seismic activity in the Temiscouata-Madawaska Valley, Quebec - New Brunswick, Canada, Can.J.Earth Sci., 29, 1043-1059.

Sibson, R.H., 1974. Frictional constraints on thrust, wrench and normal faults. Nature, 249: 542-544.

Smith, C.A., S. Grigull & H. Millo, 2018. Geomorphic evidence of multiple surface ruptures of the Merasjarvi "postglacial fault", northern Sweden. GFF, 140(4), 318-322. doi: 10.1080/11035897.2018.1492963.

Steffen, H., O. Olesen & R. Sutinen, 2021a. Glacially-Triggered Faulting. Cambridge University Press, Cambridge, UK.

Steffen, R., P. Wu, H. Steffen & D.W. Eaton, 2014a. On the implementation of faults in finite-element glacial isostatic adjustment models, Computers & Geosciences, 62, 150-159, doi: 10.1016/j.cageo.2013.06.012.

Steffen, R., P. Wu, H. Steffen & D.W. Eaton, 2014b. The effect of earth rheology and ice-sheet size on fault-slip and magnitude of postglacial earthquakes, Earth & Planet. Sci.Lett. 388, 71-80, doi: 10.1016/j.epsl.2013.11.058.

Steffen, R., H. Steffen, P. Wu & D.W. Eaton 2014c. Stress and fault parameters affecting fault slip magnitude and activation time during a glacial cycle, Tectonics, 33, 1461-1476, doi: 10.1002/2013TC003450.

Steffen, R., H. Steffen, P. Wu & D.W. Eaton 2015. Reply to comment by Hampel et al. on "Stress and fault parameters affecting fault slip magnitude and activation time during a glacial cycle", Tectonics, 34, 2359-2366, doi: 10.1002/2015TC003992.

Steffen, R., P. Wu, B. Lund, 2021b. Geomechanics of Glacially-Triggered Faulting, in Glacially-Triggered Faulting, Edited by H. Steffen, O. Olesen & R. Sutinen, Cambridge University Press, Cambridge, UK.

Stein, S., N.H. Sleep, R.J. Geller, S.C. Wang and G.C. Kroeger, 1979. Earthquakes along the passive margin of Eastern Canada, Geophys.Res.Lett., 6, 537-540.

Stephansson, O., 1989. Stress Measurements and modeling of crustal rock mechanics in Fennoscandia, in Earthquakes at North-Atlantic Passive Margins: Neotectonics and Postglacial Rebound, edited by S. Gregersen and P.W. Basham, Kluwer.

Stewart, I.S., J. Sauber & J. Rose, 2000. Glacio-seosmotectonics: ice sheets, crustal deformation and seismicity. Quat. Sci. Rev. 19: 1367-1389.

Tsai, V. C., G. Ekström, 2007. Analysis of glacial earthquakes. J. Geophys. Res. 112, F03S22.

Tsai, V. C., J. R. Rice, M. Fahnestock, 2008. Possible mechanisms for glacial earthquakes. J. Geophys. Res. 113, F03014.

Tsuboi, S., M. Kikuchi, Y. Yamanaka, M. Kanao, 2000. The March 25, 1998 Antarctic earthquake: great earthquake caused by postglacial rebound. Earth Planets Space 52: 133-136.

Turcotte, D.L. & G. Schubert, 1982. Geodynamics: applications of continuum physics to geological problems, John Wiley & Sons, New York. pp. 450.

Turpeinen, H., A. Hampel, T. Karow, G. Maniatis, 2008. Effect of ice growth and melting on the slip evolution of thrust faults. Earth & Planet. Sci. Lett. 269: 230-241, doi: 10.1016/j.epsl.2008.02.017

Van der Veen, C.J., 1999. Fundamentals of glacier dynamics. A.A. Balkema, Rotterdam, pp.462.

Voss, P., S.K. Poulsen, S.B. Simonsen & S. Gregersen, 2007. Seismic hazard assessment of Greenland. Geol. Survey. Denmark & Greenland Bull. 13:57-60.

Walcott, R.I., 1970. Isostatic response to loading of the crust in Canada, Can.J.Earth Sci., 7: 716-727.

Wang, H., P. Wu, W. Van der Wal, 2008. Using postglacial sea level, crustal velocities and gravity-rate-of-change to constrain the influence of thermal effects on mantle lateral heterogeneities, J. Geod., 46:104-117, doi:10.1016/j.jog.2008.03.003

Whillans, I.M., Y.H. Chen, C.J. van der Veen & T.J. Hughe, 1989. Force budget: III. Application to three-dimensional flow of Byrd Glacier, Antarctica. Journ. Glaciol. 35:68-80.

Whitehouse, P.L., M.J. Bentley & A.M. Le Brocq, 2012. A deglacial model for Antarctica: geological constraints and glaciological modeling as a basis for a new model of Antarctic glacial isostatic adjustment, Quat. Sci.Rev. 32,1-24. doi: 10.1016/j.quascirev.2011.11.016.

Wolf, D., 1985a. On Boussinesq's problem for Maxwell continua subject to an external gravity field. Geophys. J. R. astr. Soc., 80:275-279.

Wolf, D., 1985b. The normal modes of a uniform, compressible Maxwell half-space. J. Geophys., 56: 100-105.

Wong, M.C.K. and P. Wu, 2019. Using commercial finite-element packages for the study of Glacial Isostatic Adjustment on a compressible self-gravitating spherical earth – 1: harmonic loads, Geophys. J. Int., 217,1798-1820, doi: 10.1093/gji/ggz108.

Worm, H. U., A. M. M. Ahmed, N. U. Ahmed, H. O. Islam, M. M. Huq, U. Hambach, and J. Lietz. 1998. Large sedimentation rate in the Bengal Delta; magnetostratigraphic dating of Cenozoic sediments from northeastern Bangladesh, Geology 26: 487-490.

Wu, P., 1978. The response of a Maxwell earth to applied surface mass loads: Glacial isostatic adjustment, MSc Thesis, University of Toronto, Toronto.

Wu, P., 1992a. Viscoelastic vs. Viscous deformation and the advection of prestress. Geophys. J. Int.,108:35-51.

Wu, P., 1992b. Deformation of an incompressible viscoelastic flat earth with Power Law Creep: a Finite Element approach. Geophys.J.Int.,108, 136-142.

Wu, P., 1996. Changes in orientation of near-surface stress field as constraints to mantle viscosity and horizontal stress differences in Eastern Canada, Geophys. Res. Lett., 23: 2263-2266.

Wu, P., 1997. Effect of viscosity structure of fault potential and stress orientations in eastern Canada, Geophys.J.Int., 130: 365-382.

Wu, P., 1998. Will earthquake activity in Eastern Canada increase in the next few thousand years? Can.J.Earth Sci., 35: 562-568.

Wu, P., 2002a. Mode coupling in a viscoelastic self-gravitating spherical earth induced by axisymmetric loads and lateral viscosity variations, Earth and Planetary Science Letters, 202, 49-60, doi:10.1016/S0012-821X(02)00750-1.

Wu, P., 2002b. Effects of Mantle Flow Law Stress Exponent on Postglacial Induced Surface Motion and Gravity in Laurentia, Geophys.J.Int., 148: 676-686.

Wu, P., 2004. Using commercial finite element packages for the study of earth deformations, sea levels and the state of stress, Geophys. J. Int., 158: 401-408.

Wu, P., 2006. Sensitivity of relative sea levels and crustal velocities in Laurentide to radial and lateral viscosity variations in the mantle, Geophys. J. Int., 165, 401-413.

Wu, P. & H.S. Hasegawa, 1996a. Induced stresses and fault potential in Eastern Canada due to a disc load: a preliminary analysis. Geophys.J.Int., 125: 415-430.

Wu, P. & H.S. Hasegawa, 1996b. Induced stresses and fault potential in Eastern Canada due to a realistic load: a preliminary analysis. Geophys.J.Int., 127: 215-229.

Wu, P. & P. Johnston, 2000. Can deglaciation trigger earthquakes in N. America? Geophys. Res. Lett., 27: 1323-1326.

Wu, P., P. Johnston & K. Lambeck, 1999. Postglacial rebound and fault instability in Fennoscandia, Geophys.J.Int., 139: 657-670.

Wu, P. & S. Mazzotti, 2007. Effects of a lithospheric weak zone on postglacial seismotectonics in Eastern Canada and Northeastern USA, accepted in GSA Special Paper 425: Continental intraplate earthquakes: science, hazard and policy issues, Ed. S. Stein & S. Mazzotti, p. 113-128.

Wu, P. & W.R. Peltier, 1982. Viscous gravitational relaxation, Geophy.J.R. Astr.Soc., 70: 435-486.

Wu, P. & W.R. Peltier, 1984. Pleistocene deglaciation and the earth's rotation: a new analysis, Geophy.J.R.Astr.Soc., 76:753-792.

Wu, P., R. Steffen, H. Steffen & B. Lund, 2021. Chapter 8.1 Glacial Isostatic Adjustment Models for Earthquake Triggering, in Glacially-Triggered Faulting, Edited by H. Steffen, O. Olesen & R. Sutinen, Cambridge University Press, Cambridge, UK.

Wu, P. and H.S. Wang, 2008. Postglacial Isostatic Adjustment in a Self-Gravitating Spherical Earth with Power-law rheology, J. Geod., 46:118-130, doi:10.1016/j.jog.2008.03.008.

Yin, Z.M., & G. Ranalli, 1992. Critical stress difference,fault orientation and slip direction in anisotropic rocks under non-Andersonian stress system. Journal of Structural Geology, 14: 237-244.

Zoback, M.L., 1992a. First- and Second-order patterns of stress in the lithosphere: The World Stress Map Project, J.Geophys.Res., 97: 11703-11728.

Zoback, M.L., 1992b. Stress field constraints on intraplate seismicity in eastern North America, J.Geophys.Res. 97: 11761-11782.

Zoback, M.D. & J.H. Healy, 1984. Friction, faulting and in situ stress, Ann. Geophys., 2, 689-698.

Zoback, M.D. & M.L. Zoback, 1991. Tectonic stress field of North America and relative plate motions, in The Geology of North America, Decade Map Vol.1, Neotectonics in North America, edited by Slemmons et al., pp.339-366, Geological Society of America, Boulder, Colo.

Zoback, M.D., R. Apel, J. Baumgartner, M. Brudy, R. Emmermann, B. Engeser, K. Fuchs, W. Kessels, H. Rischmuller, F. Rummel and L. Vernik, 1993. Upper-crustal strength inferred from stress measurements to 6 km depth in the KTB borehole, Nature, 365, 633-635.